sensors

MDPI

Review

Polymer-Based Triboelectric Nanogenerators for Self-Powered Sensing: Materials, Interfaces, and Device Architectures

Giovanna Di Pasquale [1,*] and Antonino Pollicino [2,*]

[1] Department of Chemical Sciences, University of Catania, V.le A. Doria 6, 95125 Catania, Italy
[2] Department of Civil-Industrial Engineering and Architecture, University of Catania, V.le A. Doria 6, 95125 Catania, Italy
* Correspondence: giovanna.dipasquale@unict.it (G.D.P.); apollicino@unict.it (A.P.)

Abstract

Polymer-based triboelectric nanogenerators (TENGs) convert mechanical stimuli into electrical signals without requiring an external bias; this makes them a promising platform for self-powered sensing systems. This review critically examines polymer-based TENGs from the perspective of their use as sensors, rather than as generators, integrating aspects related to the physics of contact electrification, polymer chemistry, device engineering, and metrology. After outlining the charge generation mechanisms, operating modes, and performance metrics, the work analyzes the molecular, dielectric, and surface engineering of triboelectric polymers, their implementation in sensing-oriented architectures, and the related applications, in the mechanical, wearable, biomedical, environmental, and analytical fields, also addressing degradation mechanisms and sustainability. A finding that consistently emerges in these areas is that the heterogeneity of testing protocols and adopted metrics prevents quantitative comparison among studies. Following this synthesis, the MIS-TENG ("Minimum Information Set for Triboelectric Sensors") is proposed as a reporting framework, not a measurement standard, complementary to the existing figures of merit for generators; it includes a reliability module (MIS-TENG-R) and is illustrated through six devices from the literature. Finally, research perspectives based on comparable data are outlined, including a roadmap for the interlaboratory validation that the framework still requires.

Keywords: triboelectric nanogenerators; self-powered sensing; triboelectric polymers; contact electrification; surface engineering; wearable sensors; reliability; metrology; standardization; sustainability

Check for updates

Academic Editor: Zhen Wen

Received: 24 October 2026
Revised: 19 November 2026
Accepted: 21 November 2026
Published: 26 November 2026

Copyright: © 2026 by the authors. Licensee MDPI, Basel, Switzerland. This article is an open access article distributed under the terms and conditions of the Creative Commons Attribution (CC BY) license.

1. Introduction: From Triboelectricity to Self-Powered Polymer Sensors

Over the last decade, triboelectric nanogenerators (TENGs) have emerged as an enabling technology for self-powered electronics, capable of converting mechanical stimuli (vibrations, pressures, and small-amplitude movements) into usable electrical energy. By exploiting one of the oldest known electrostatic phenomena, the triboelectric effect, TENGs have redefined how such stresses can be harvested and used directly for sensing and communication. Since their introduction by Fan and colleagues in 2012, TENGs have evolved from proof-of-concept devices into platforms investigated for wearable monitoring, structural diagnostics, and environmental sensing, in which the transducer autonomously generates the electrical signal without requiring external bias [1–5].

At the heart of this progress lies the polymer interface, which serves both as the active triboelectric material and as a mechanically compliant support; the reasons for this central role are illustrated in Section 1.2.

1.1. From Triboelectricity to Triboelectric Sensing

The triboelectric effect, traditionally regarded as a source of troublesome static electricity, is exploited in TENGs by combining contact-induced charge separation with electrostatic induction (Sections 2.1 and 2.2). Since the amplitude, frequency, and waveform of the resulting signal depend on the mechanical stimulus and the device transfer function, TENGs can operate not only as energy-harvesting systems but also as transducers capable of converting mechanical stimuli, or, in hybrid architectures, chemical or biological quantities (Section 6.2.5), into voltage, current, or charge, without the need for external bias [6–8]. This shift, from the concept of "energy-harvesting devices" to that of "signal-generating sensors," constitutes the perspective adopted in this review.

1.2. Why Polymers Are Central in the Triboelectric Sensor

Polymers are the cornerstone of modern TENG technology for both scientific and practical reasons. First, their molecular diversity allows precise modulation of the tendency to donate or accept electrons by acting on surface functional groups (see Section 3.1). Second, their dielectric permittivity (ε_r) and surface potential can be tuned to modulate charge trapping and retention. Third, the soft mechanics of triboelectric elastomers (Young's moduli typically between ~50 kPa and ~10 MPa) allows intimate contact with external stimuli and reliable performance under repeated deformations; stiffer fluoropolymers (Polytetrafluoroethylene (PTFE), Fluorinated ethylene propylene (FEP), Polyvinylidene fluoride (PVDF)) and polyimides, with moduli of roughly 0.4–3 GPa, contribute conformability in the form of thin films rather than as elastomeric substrates.

Representative tribo-positive polymers include polyamides (Nylon), polyethyleneimine (PEI), and chitosan, while fluorinated polymers such as PTFE, FEP, and PVDF, together with other fluorine-free but still tribo-negative materials such as polydimethylsiloxane (PDMS) and polyimide, dominate the negative end of the triboelectric series [9,10]; the complete classification of polymer families and their polarity is developed in Section 3.1. In systems appropriately optimized by surface engineering and chemical modification, charge densities above 100 $\mu C\ m^{-2}$ have been reported [11,12], and breakdown suppression or charge-excitation strategies reach the order of $mC\ m^{-2}$ (see Section 2.1) [13–16]. Micro/nano-structuring can increase the real contact area, while high-permittivity nanofillers can increase polarization and charge storage capacity, with effects depending on the formulation and device architecture [17,18]; these two levers, respectively surface engineering and dielectric engineering, are treated in detail in Sections 3.4 and 3.5.

The processability and conformability of polymers allow the design of TENGs resistant to bending and stretching and their integration into fabrics, elastomeric substrates, and biointerfaces. Stability under repeated deformation and environmental variations is not intrinsic, however, but depends on the formulation, architecture, and protection strategies discussed in Sections 3 and 8.

1.3. Self-Powered Sensing and Closed-Loop Operation

The self-generated signal makes TENGs suitable for sensing pressure, strain, and vibrations, as well as physiological signals related to heartbeat or respiration. The amplitude and shape of this signal depend not only on the stimulus but also on the effective contact area, the deformation rate, the state of charge, and environmental conditions; moreover, the "self-powered" nature pertains to the transduction process but not necessarily to the

entire electronic chain, which may still require interface circuits and energy storage systems. Throughout this review, "self-powered" refers to devices in which the TENG output itself constitutes the sensing signal, so that no external power is needed for transduction, although acquisition and readout may rely on external electronics. "Battery-free" denotes systems that operate without a pre-charged battery, with harvested energy supplying signal conditioning and/or readout, possibly assisted by an external RF field for Near-field communication (NFC). "Autonomous" is reserved for systems in which harvested energy alone supplies conditioning, readout and transmission, without any external source or pre-charged storage. On these bases, recent polymer nanogenerators detect pressures down to a few pascals, as in a drum-structured device with a detection limit of 3.9 Pa that resolves pulse, throat, and wrist micromotions [19], and track complex dynamic movements in real time, from machine-learning gesture recognition for wireless robot control [19] to on-line monitoring of joint bending angles and step counts in silicone-rubber-based smart garments [20] and AI-assisted recognition of gait, sitting posture, and sleep patterns [21].

The ability to harvest energy and simultaneously generate a sensory signal allows the integration of energy harvesting and sensing in the same triboelectric element. When such an element is coupled to power management, processing, and actuation, this integration can form the basis of autonomous or closed-loop systems for the Internet of Things and wearable monitoring.

1.4. Current Challenges, Aims, and Structure of This Review

Despite rapid growth, the field remains fragmented. Most existing reviews focus either on TENG fundamentals or on specific application domains (wearable devices, energy harvesters), but few offer a comprehensive materials-oriented perspective linking polymer chemistry, triboelectric physics, device engineering, and metrology. Moreover, inconsistencies in test protocols, normalization of results, and reporting metrics complicate meaningful comparison across studies. There are already established quantitative tools for evaluating TENGs as generators, including the structure and material figures of merit introduced by Zi et al. [22] and the quantified triboelectric series proposed by Zou et al. [23]. The latter, shown in Figure 1, converts the traditional qualitative ranking into a surface charge density scale with a stated uncertainty, measured under controlled environmental conditions against a single reference counter-material. The values are normalized with respect to PTFE ($\sigma_{PTFE} \approx -113\ \mu C\ m^{-2}$) to define a dimensionless charge density $\alpha = \sigma/|\sigma_{PTFE}|$. The signs are relative to the mercury counterpart and do not represent absolute polarities (Section 3.1).

However, such instruments are primarily aimed at energy conversion capability and do not fully describe sensitivity, limit of detection (LoD), nonlinearity, hysteresis, repeatability, and drift of TENGs used as sensors. More recent sensing-oriented proposals also remain limited to specific application domains, such as acoustic sensing [24,25], while shared test protocols are still being defined [26]. This gap defines the contribution of the present work, which consists primarily of a critical review. Its fundamental contribution lies in an integrated synthesis of polymer-based TENG sensors, spanning from molecular design to functional applications, at a time when molecular control of triboelectricity, the use of ionic and "soft" materials, artificial-intelligence-assisted signal analysis, and sustainable design are converging [27–29]. This synthesis is conducted from the perspective of the sensor rather than that of the generator: for each area, not only the reported performance is examined, but also the ways in which that performance was measured and documented. A further contribution emerges from this analysis: since empirical evidence repeatedly shows that the heterogeneity of protocols and metrics prevents comparison among studies, the work proposes a framework for the documentation of TENG sensors, intended as a basis

for discussion within the scientific community and for future standardization, rather than as an already defined standard.

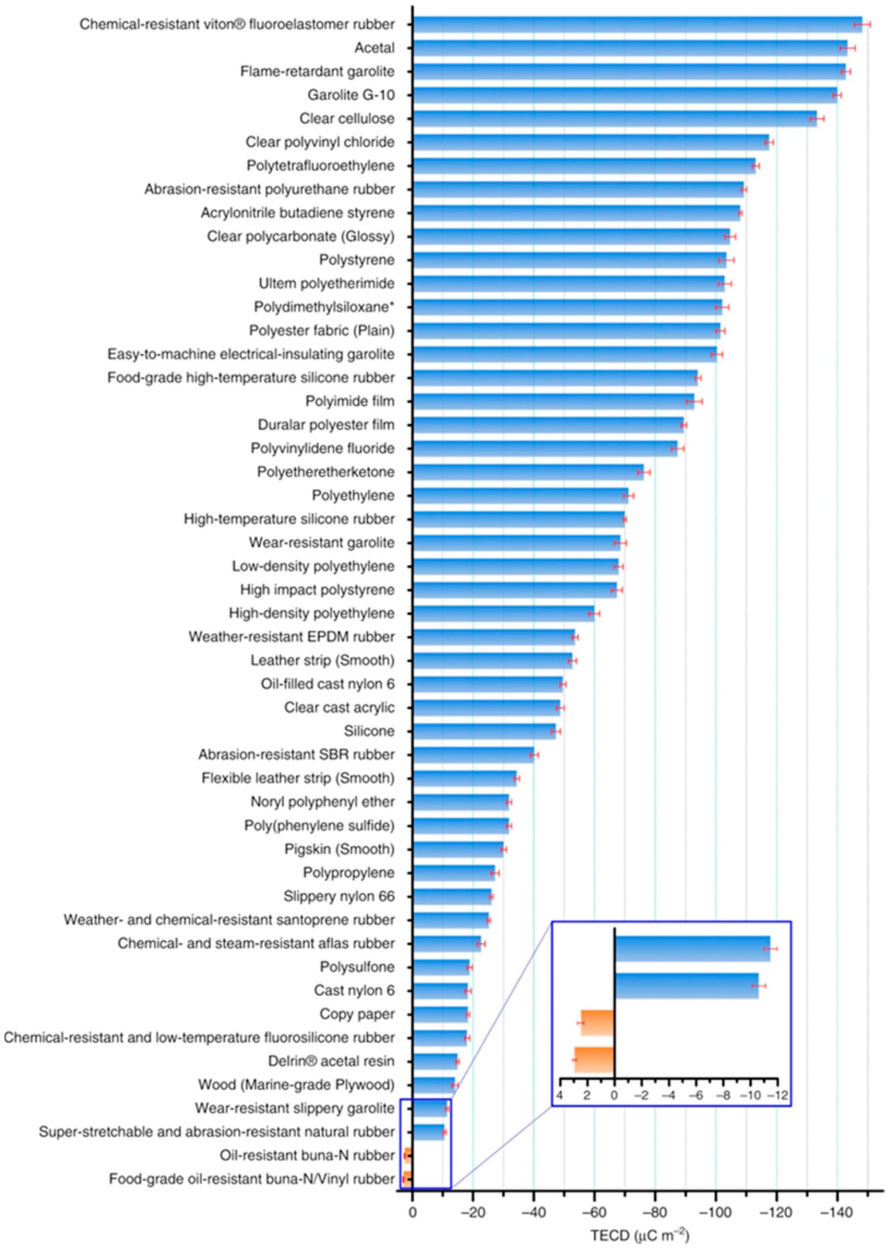


Figure 1. Quantified triboelectric series of more than fifty materials, ordered by triboelectric charge density measured through contact-separation cycles with liquid mercury under a nitrogen atmosphere (20 ± 1 °C; relative humidity 0.43%); error bars represent one standard deviation. Values are normalized with respect to PTFE ($\alpha = \sigma/|\sigma_PTFE|$); $\alpha < 0$ and $\alpha > 0$ indicate, respectively, materials that are more tribo-negative and more tribo-positive than mercury. The exchanged charge between two materials is determined by the distance separating them within the series, not by their absolute positions. The material marked with an asterisk '*' means it has strong adhesion with mercury, a small drop of mercury is observed when it is separated with mercury. The measured TECD value may be a bit lower than its real value. Reproduced from Zou et al. [23], Nat. Commun. 2019, 10, 1427, Figure 4; © 2019 The Authors, published by Springer Nature, licensed under CC BY 4.0.

Specifically, the review aims to identify the structure–property–function relationships that govern triboelectric charge generation in polymers; to examine how microstructuring and interface engineering improve performance; to compare architectures and performance

metrics across different domains, such as mechanical, wearable, and environmental sensors; to discuss sustainability, recyclability, and future design paradigms for the next generation of self-powered sensors; and, within all these topics, to analyze the ways in which test conditions and performance metrics are reported. As a result of this analysis, Section 9 introduces MIS-TENG (Minimum Information Set for Triboelectric Sensors), a minimum information set that complements the figures of merit already established in the scientific literature [22,23].

MIS-TENG extends reporting practices, moving from the energy evaluation of generators to the metrological characterization of polymeric TENGs understood as sensors (sensitivity, LoD, nonlinearity, repeatability, hysteresis, drift). It is organized into core descriptors and modules specific to architecture or application, and is accompanied by a module dedicated to reliability (MIS-TENG-R). The framework was developed by the authors on the basis of the evidence examined and is illustrated through six case studies of devices already present in the literature. Since it has not yet been validated through interlaboratory comparisons, Section 11.3 outlines a roadmap for such validation.

Section 2 presents the physical foundations, Section 3 the materials, and Section 4 the device architectures. Sections 5–7 deal, respectively, with mechanical sensing, wearable and biomedical sensing, and environmental and analytical sensing. Section 8 addresses reliability and introduces the MIS-TENG-R module. Section 9 collects the reporting gaps identified in Sections 2–8 and translates them into the MIS-TENG framework. Section 10 is dedicated to sustainability, while Section 11 summarizes the conclusions and research perspectives. Readers interested exclusively in the state of the art can consult Sections 2–8 and 10 independently; the cross-references to Section 9 present in those sections (e.g., Sections 2.1, 5.6, 7.5 and 8.7) indicate the point at which each gap is first identified.

1.5. Literature Search and Selection

This work constitutes a critical narrative review, supported by a structured literature search, and not a systematic review. A Scopus search was conducted to identify articles and reviews published in English from 2012, the year of the introduction of TENGs, up to July 2026, combining the term "triboelectric nanogenerator*" and "polymer*" with keywords specific to each thematic block of the review (Appendix A, Table A1); the search was supplemented by citation tracking of seminal works. Priority was given to peer-reviewed studies published in the 2023–2026 period, although earlier contributions were also included where they introduced concepts, models, or benchmarks still in use [4,22,23,30]. Quantitative data were drawn from primary experimental studies rather than from reviews; works subject to retraction or "expressions of concern" were also excluded. The devices presented in Sections 5.6 and 7.5 are representative rather than "record" values: they are recent studies reporting the test conditions necessary to interpret their performance. The six MIS-TENG case studies (Section 9.4.1) were selected from these tables and figures so as to cover a variety of measured quantities, operating modes, and architectures, drawing on works for which the full text and Supporting Information were available for the coding of individual elements.

2. Fundamentals of Triboelectric Nanogenerators

This section refers exclusively to the physical elements necessary to interpret polymer-based TENG sensors: the charge generation regimes that determine the surface charge density σ (Section 2.1), the relationship between voltage, charge, and displacement that defines the transfer function (Section 2.2), the equivalent-circuit description (Section 2.3), and the metrics used throughout the review (Section 2.4). The operating modes are addressed

together with device geometries in Section 4.2, while the triboelectric series is examined together with the classification of polymers in Section 3.1.

2.1. The Triboelectric Effect: Charge Generation at Interfaces

When two materials come into contact, a charge transfer occurs at the interface, determined by asymmetries in their surface properties, such as work function, electron affinity, and surface density of states. Upon separation, equal and opposite net charges remain on the two surfaces, generating an interfacial potential difference. On the nanoscale, however, each surface can exhibit a mosaic of domains with charges of opposite sign, a phenomenon accompanied by bond breaking and material transfer [31]. The identity of the transferred species is still a matter of debate, and no single mechanism can explain all cases, regardless of the material pairs and specific conditions. A notable microscopic model is the one based on the overlap of electron clouds (or potential well model), proposed by Wang and co-workers; according to this model, compression during contact reduces the interatomic potential barrier, favoring electron transfer. The main experimental evidence supporting this theory, namely the temperature dependence of the release of the transferred charge, consistent with a thermionic emission mechanism, has been observed in contacts between metals and dielectrics [32,33]. The extension of this model to all solid-solid contacts is not yet fully confirmed: the relative weight of electron, ion, or material transfer depends on the materials involved and the contact conditions, which can be classified into five distinct regimes.

(i) Metal–dielectric and metal–semiconductor contacts. Electron transfer is the predominant contribution, whose direction is determined by the difference between work functions or between effective energy levels [32–35]. Even in this case, the polymer surface is not static: at metal–polymer interfaces, acceptor states are generated and annihilated mechanochemically during contact, and their density depends on the deformation history of the polymer [36].

(ii) Dry contacts between polymers. This is the most debated regime and, at the same time, the most relevant one for all-polymer TENGs. Electron transfer via orbital overlap and mass transfer via heterolytic bond cleavage represent two competing interpretations. For the Poly(methyl methacrylate) (PMMA)/PTFE pair, simulations indicate that covalent bonds break before the electron clouds overlap; moreover, the presence of charges that cannot be removed by grounding suggests the existence of bound charges carried by the transferred material [8].

(iii) Polymer interfaces in the presence of moisture or ions. Adsorbed water and mobile ions introduce an ionic conduction channel. In ionomer pairs, electron and ion transfer occur simultaneously; the ionic contribution increases the accumulated charge at relative humidity (RH) above about 50% [37]. In the case of nonionic insulators, water accelerates charge exchange and increases the acquired charge as humidity increases, provided that the curved contact surface is hydrophilic [7].

(iv) Systems characterized by measurable material transfer. When the transferred material can be detected by spectroscopic techniques, as in the case of PTFE/PDMS pairs [31], or manifests as a transfer film (in sliding contacts involving PTFE, cf. Section 8.1) [26], the charge cannot be attributed exclusively to electron transfer; in this context, the contact history becomes an integral part of the mechanism. Sliding introduces an additional contribution: elastic shear stress breaks the symmetry between the leading and trailing edges of the contact area. It has been hypothesized that the resulting difference in strain-induced polarization represents a general origin of the “tribo” component [6].

(v) Liquid–polymer contacts. When the counter-surface is a liquid, electron transfer from the liquid to the polymer coexists with ion adsorption and the formation of an electric double layer (EDL); in the case of aqueous solutions, electron transfer tends to prevail on

hydrophobic polymers such as fluoropolymers, whereas on hydrophilic ones ion transfer prevails [38]. The charge acquired therefore depends on both the liquid and the polymer. A quantified triboelectric series comprising about 50 liquids, measured inside FEP tubes using liquid columns moved by a gas flow, a solution that allows flow dynamics to be decoupled from electrification, demonstrated that hydroxyl groups and the presence of ions at dilute concentrations (about 10^{-3} mol L^{-1}) increase the transferred charge. By contrast, alkyl groups and ionic concentrations above a threshold specific to each chemical species reduce this charge, owing to compression of the electric double layer and the electrostatic screening effect [39]. In the same experimental apparatus, FEP and PTFE acquired similar charges in contact with deionized water, higher than those observed for polyvinyl chloride (PVC), polyethylene (PE), polyamide 66, and silicone rubber; the ranking of the analyzed liquids remained essentially unchanged when FEP was replaced by PTFE, polypropylene, PVC, or PE, although the absolute charge densities showed differences [39]. Signal amplification, obtained by atomizing the liquid, made it possible to distinguish the contributions of electron transfer, molecular polarization, ionic migration, and ionic screening [40]. This regime constitutes the operating principle of the droplet-, flow-, or wave-based devices described in Section 7, and it is the reason why liquid composition, ionic strength, and wettability are among the descriptors of module M5 (Section 9.4).

For sensing purposes, the practical consequence is that the charge density—and, consequently, the device transfer function—depends on variables specific to the regime considered (humidity, ionic content, liquid composition, contact history, sliding); this is precisely why such variables appear among the MIS-TENG descriptors (Section 9.4).

The charge density (σ) obtainable by triboelectrification alone is usually between 10^{-6} and 10^{-3} C m^{-2}, depending on the material pair and surface treatment; in air, it is limited by the phenomenon of electrical discharge in gases (Paschen regime). Techniques such as discharge suppression, corona charging, dielectric optimization, and deep-trap engineering allow the intrinsic σ to be raised to values on the order of a few mC m^{-2} (8.6 mC m^{-2} [13]), whereas charge pumping and charge excitation increase only the effective output charge through cyclic accumulation based on external circuits [14–16]. Both approaches are subject to the same limit (Figure 2), whose threshold increases as the dielectric thickness or ambient humidity decreases [16]. For sensing purposes, a relevant consequence is that the gain of the transfer function, which varies in proportion to σ (Section 2.2), depends on dielectric thickness and ambient humidity; therefore, these parameters must always be specified (Section 9.2.3).

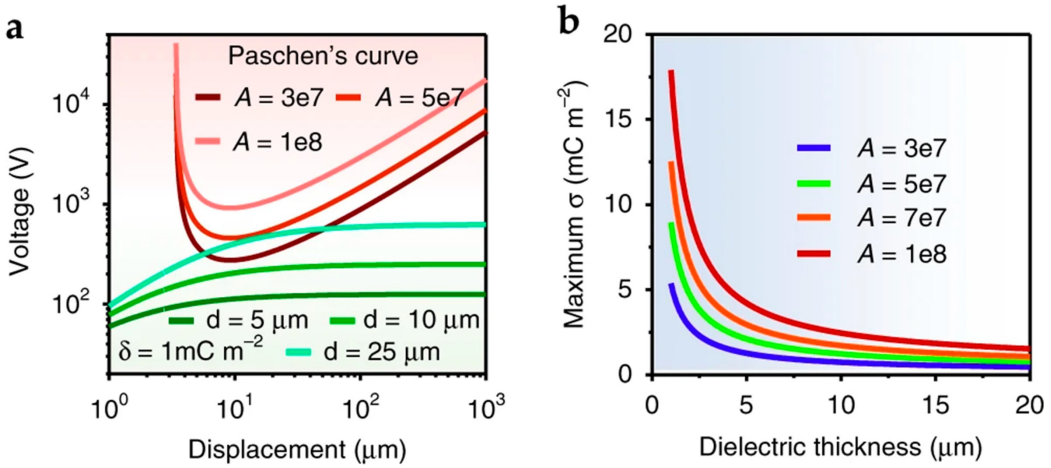


Figure 2. Air-breakdown limit on the triboelectric charge density in contact–separation TENGs. (**a**) Paschen curves for different values of the atmospheric constant A, inversely proportional to

relative humidity, together with the gap voltage as a function of displacement (air-gap distance x) for dielectric thicknesses d = 5, 10 and 25 μm at $\sigma = 1$ mC m^{-2} (denoted δ in the panel); air breakdown occurs where the gap-voltage curve meets the Paschen curve. (**b**) Maximum charge density limited by air breakdown as a function of dielectric thickness for different values of A: the limit rises steeply as the dielectric becomes thinner and as A increases, i.e., as humidity decreases. Adapted from Liu et al. [16], Nat. Commun. 2020, 11, 1599, Figure 1e,f (panels relabeled (**a**) and (**b**)); © 2020 The Authors, published by Springer Nature, licensed under CC BY 4.0.

2.2. Electrostatic Induction: Converting Charge into Current

Once triboelectrification has occurred, separation of the two materials establishes an electric field between the surfaces; if these are connected by an external circuit, electrostatic induction drives the charges that tend to balance the potential difference. For the commonly adopted one-dimensional contact–separation model, the electromechanical behavior of a TENG can be described by the voltage–charge–displacement relation:

$$V(x, Q) = -\frac{Q(d_0 + x)}{A\varepsilon_0} + \frac{\sigma x}{\varepsilon_0} \quad (1)$$

where x is the instantaneous separation between the triboelectric surfaces and $d_0 = \sum d_i/\varepsilon_{ri}$ is the effective dielectric thickness, summed over the dielectric layers between the electrodes ($d_0 = d_1/\varepsilon_{r1}$ for a conductor-to-dielectric device). Equations (1)–(4) assume parallel-plate geometry, i.e., separations much smaller than the lateral dimensions of the device. Under open-circuit conditions ($Q = 0$), this reduces to:

$$V_{OC} = \frac{\sigma x}{\varepsilon_0} \quad (2)$$

Under short-circuit conditions ($V = 0$), the transferred charge is

$$Q_{SC} = \frac{A\sigma x}{d_0 + x} \quad (3)$$

and, assuming that the triboelectric surface charge density remains approximately constant during a mechanical cycle,

$$I_{SC} = \frac{dQ_{SC}}{dt} = \frac{A\sigma d_0}{(d_0 + x)^2} v(t) \quad (4)$$

where $v(t) = dx/dt$. Therefore, the electrical output reflects both the displacement and the velocity history of the mechanical excitation: its waveform, and not only its amplitude, conveys information about the stimulus (Section 4.4).

2.3. Equivalent Circuit and Energy Conversion Process

The TENG can be modeled as a time-varying capacitor with a triboelectric charge and a capacitance $C(x)$ that depend on the displacement $x(t)$:

$$Q = C(x)[V_{OC}(x) - V] \quad (5)$$

Differentiation yields the output current:

$$I = \frac{dQ}{dt} = (\frac{dC}{dt})[V_{OC}(x) - V] + C(x)[\frac{dV_{OC}}{dt} - \frac{dV}{dt}] \quad (6)$$

This formalism highlights two fundamental insights: the output current arises from the mechanical modulation of capacitance and not solely from charge generation, and the delivered power ($P = IV$) depends jointly on the input mechanical frequency and on the electrical load impedance.

Reported conversion efficiencies, instantaneous (about 70% with liquid-metal electrodes [41]) or full-cycle (85% [42] and 63.5% [43] for a grating-structured freestanding and a rotary liquid-sliding TENG, respectively), refer to load-matched laboratory conditions and drop markedly under irregular excitation [44]; for sensing, stability and linearity of the transfer function matter more than efficiency.

2.4. Key Performance Metrics

Several parameters are used to characterize TENG performance both in the energy-harvesting configuration and in the sensing configuration; Table 1 summarizes their symbol, unit of measure, and operational definition [19,45,46].

Table 1. Main TENG performance metrics for energy harvesting and sensing, with symbol, unit of measure, and operational definition.

Parameter	Symbol/Unit	Definition
Generator metrics		
Open-circuit voltage	V_{OC} (V)	Peak voltage in open circuit; requires an input impedance $Z_{in} \gg 1/(2\pi f C_T)$ *, i.e., electrometer-class inputs (~10^{13}–10^{14} Ω), since 10–100 MΩ probes underestimate V_{OC}; $V_{OC} = \sigma x/\varepsilon_0$ in the parallel-plate model
Short-circuit current	I_{SC} (A)	Peak current at zero load resistance; since $I_{SC} = dQ_{SC}/dt$, it scales with separation velocity and must be reported with the motion profile
Transferred charge	Q_{tr} (C)	Short-circuit charge transferred per stroke, measured in coulomb mode, with a charge amplifier ($V_{out} = -Q/C_f$), or by integrating I_{SC}; largely velocity-independent and the most robust basis for comparison [22] (Q_{SC} when measured under short-circuit conditions, Equation (3))
Power density	P/A (W m^{-2}) (or W m^{-3})	I^2R_L/A at the optimum load $R_{opt} \propto 1/(2\pi f C_T)$, specifying whether instantaneous peak or cycle-averaged power
Sensor metrics		
Sensitivity	S (e.g., V kPa^{-1}, nC kPa^{-1}, V %$^{-1}$)	Slope of the calibration curve, $S = \Delta V/\Delta P$ (or $\Delta Q/\Delta P$, $\Delta V/\Delta\varepsilon$), within a stated stimulus range, with output quantity and units. For nonlinear responses, either piecewise slopes S_i over contiguous, stated sub-ranges, each with its own nonlinearity, or the fitted calibration function with its parameters and residuals and the local sensitivity $S(x_0) = dy/dx$ at stated operating points; a single slope over the full range, or the maximum slope alone, is not sufficient
Limit of detection	LoD (e.g., Pa, % strain)	Smallest stimulus distinguishable from baseline noise at Signal-to-noise ratio (SNR) = 3, i.e., LoD = $3\sigma_{noise}/S$, with the noise definition stated
Nonlinearity	% FS	Maximum deviation from the fitted line as a percentage of full-scale (FS) output over the stated range; R^2 alone does not quantify linearity
Hysteresis	H (% FS)	Maximum difference between outputs at the same stimulus during a full loading–unloading sweep, divided by the full-scale output: $H = \max\|y\uparrow(x) - y\downarrow(x)\|/y\mathrm{FS} \times 100\%$, with sweep rate and number of steps stated
Response/recover time	τ_r/τ_f (ms)	Rise (10→90%) and recovery (90→10%) times after a step stimulus, reported with loading rate, readout input impedance, and acquisition bandwidth
Drift	D (% h^{-1} or % per 10^3 cycles)	Change in baseline or sensitivity over a stated time under constant stimulus and environmental conditions
Durability	N_{10}% (cycles)	Number of cycles to 10% output degradation (Section 8.6)

* C_T = device capacitance.

All metrics must be reported with the mechanical (force, frequency, loading rate) and environmental (T, RH) conditions, and sensor metrics with the stimulus range and the readout mode (Section 4.1); the calculation rules adopted for the MIS-TENG framework are detailed in Table S1 (Section 9.4).

Comparison of generator output across configurations relies on the structural and material figures of merit of Zi et al. [22] and on the quantified triboelectric series of Zou et al. [23]; their relation to sensor metrology is discussed in Section 9.4.

Terminology. To avoid ambiguity, the following terms are used throughout with a single meaning. *Self-powered sensing* denotes transduction in which the TENG output is the sensing signal and no external bias is required; it does not imply that conditioning, readout or transmission are powered by the device (system-level terms are defined in Section 1.3). *Energy harvesting* denotes the extraction of electrical energy to a load or storage element, characterized by the generator metrics of Table 1. *Sensor output* denotes the primary electrical quantity read out, which must always be specified: V_{OC}, Q_{SC}, I_{SC} or the voltage across a stated load RL, as peak or peak-to-peak value. *Sensitivity* is used only for the slope of the calibration curve defined in Table 1, never for output amplitude or qualitative claims; the dependence of the output on an unintended variable is termed *cross-sensitivity*. *Charge density* (σ) denotes the triboelectric surface charge density; literature values obtained as transferred charge per unit nominal area (Q_{tr}/A) are labelled as such, since Q_{tr}/A approaches σ only for full contact and $x \gg d_0$ (Equation (3)). *Reliability* is an umbrella term for the ability to retain the transfer function under stated conditions over time, quantified by durability (N10%, retention R(t), Section 8.6) and drift (Table 1). Following the International Vocabulary of Metrology (VIM) [47] and ISO 5725-1 [48] (Section 9.6), *repeatability* refers to consecutive cycles on the same device, setup and session; *intermediate precision* to independently fabricated devices, batches or days within one laboratory; and *reproducibility* exclusively to interlaboratory conditions.

The quantitative comparison of the operating modes described in Section 4.2 is summarized in Figure 3, which presents the structural figure of merit, calculated analytically and via finite element simulation, for the five canonical configurations; the results show that dual-electrode architectures clearly outperform the single-electrode design and that the contact-mode freestanding configuration achieves the highest FOM_S value, whereas sliding modes require significantly larger displacements to reach the same open-circuit voltage.

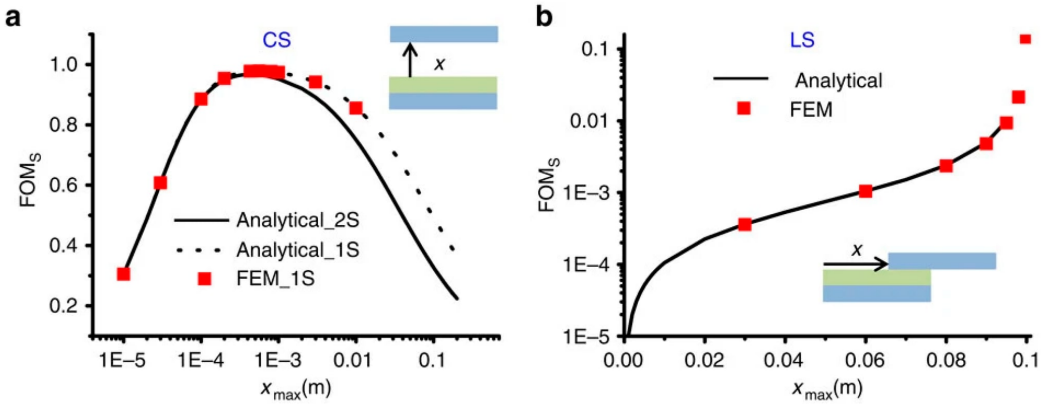


Figure 3. *Cont.*

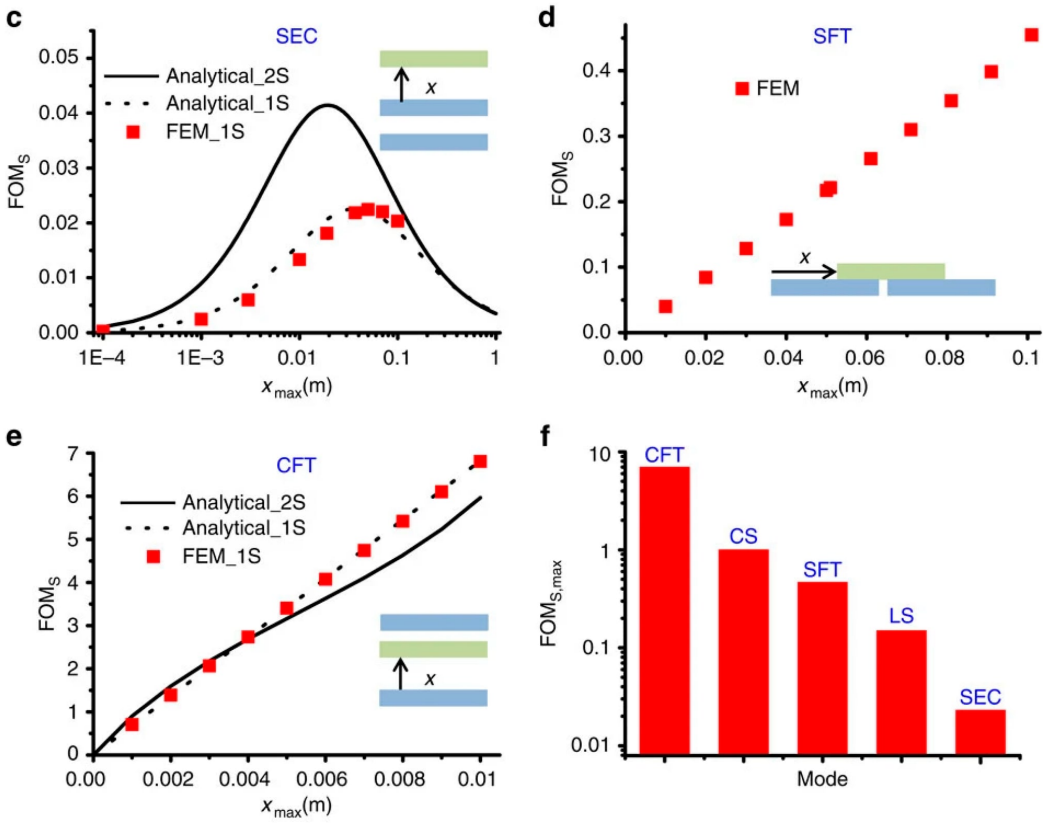


Figure 3. Structural figure of merit (FOM_S) as a function of maximum displacement x_{max} for the five canonical configurations: vertical contact-separation (CS), lateral sliding (LS), single-electrode contact (SEC), sliding free-standing (SFT), and contact free-standing (CFT) (**a**–**e**); (**f**) maximum value of the FOM_S obtained from finite element simulations. The FOM_S isolates the geometric contribution to performance, while the material-related contribution is contained in the term σ^2. Reproduced from Zi et al. [22], Nat. Commun. 2015, 6, 8376, Figure 3; © 2015 The Authors, published by Springer Nature, licensed under CC BY 4.0.

3. Polymeric Triboelectric Materials and Surface Engineering

After defining the charge generation and conversion mechanisms in Section 2, this section examines how polymer chemistry, structure, and mechanics control these processes. The focus thus shifts from the general physics of TENGs to the composition–structure–property relationships that guide material selection, from triboelectric polarity and dielectric properties to functionalization, microstructuring, and mechanical compliance.

3.1. Classification of Triboelectric Polymers

The triboelectric series ranks materials according to the sign and relative magnitude of the charge acquired with respect to a reference element under defined conditions; the quantified series shown in Figure 1 turns this ranking into a material parameter, associated with a given uncertainty [23]. Polymers bearing electron-donor groups (–NH_2, –OH) tend to lie toward the positive end, whereas those with electron-withdrawing groups (–F, –CF_3) tend toward the negative end; charge transfer is maximized when materials that are far apart in the series are paired, such as nylon and PTFE. Since polarity depends on the pair of materials in contact and is influenced by factors such as morphology, contamination, humidity and contact history, Table 2 summarizes representative trends, not absolute values. In addition to the choice of pair, charge density can be modulated over several orders of magnitude by using functional copolymers, dielectric composites, surface treatments

and charge-trap engineering techniques [49–51], strategies that are discussed in detail in Sections 3.2–3.8.

Table 2. Classification of the main families of triboelectric polymers by polarity (electron donors, electron acceptors, neutral/tunable materials), with the dominant functional groups responsible for the triboelectric behavior.

Category	Representative Polymers	Dominant Groups	Triboelectric Polarity
Positive (electron donors)	Nylon-6, Nylon-11, Poly(ethyleneimine) (PEI; not to be confused with poly(ether imide), which is strongly tribo-negative [23]), Chitosan	$–NH_2$, –OH, –NH–	Tend to lose electrons → positive surface charge
Negative (electron acceptors)	PDMS, PDMS copolymers, PTFE, FEP, PVDF, P(VDF–TrFE), PEEK, Polyimide (Kapton), PMMA (weakly negative)	–Si–O–, –F, $–CF_3$, –CO– imide	Tend to acquire electrons → negative surface charge
Neutral/tunable	PVA, PU, PEO *	weak dipoles, hydrophilic parts	Tunable via functionalization, doping, or formulation (e.g., an abrasion-resistant PU rubber lies close to PTFE in the quantified series [23], while other formulations behave as positive counterparts)

* PVA, poly(vinyl alcohol); PU, polyurethane; PEO, poly(ethylene oxide).

Fluorinated polymers such as PTFE and FEP lie toward the negative end owing to the strong electron-withdrawing fluorine atoms, which lower surface energy and stabilize trapped electrons. Within the negative category, however, the degree of tribo-negativity varies considerably: in the quantified triboelectric series, PMMA ($\alpha = -0.43$) lies in the less negative half of the series, unlike PTFE, which lies close to its extreme. The quantified series nevertheless shows that fluorination alone does not determine rank: PVDF ($\alpha = -0.77$) is less negative than PDMS (-0.90) and polyimide (-0.82), and several non-fluorinated materials (acetal, glass-epoxy laminates, clear cellulose) exceed PTFE [23]. PDMS, due to its siloxane backbone, and polyimide (Kapton), whose imide/carbonyl groups are electron-withdrawing and which lacks free amines or hydroxyls, behave as tribo-negative materials in the vast majority of devices, in agreement with the quantified triboelectric series and with their current use as the negative layer [23,45,52,53]. Conversely, polymers rich in amine, amide, and hydroxyl groups (Nylon, PEI, gelatin) act as positive counterparts when paired with fluoropolymers or PDMS.

Natural and biodegradable polymers (cellulose and nanocellulose, chitosan, silk fibroin, collagen, gelatin), also obtainable from waste biomass, generally exhibit lower charge densities than fluoropolymers, but, in the most common pairs, they are positioned on the positive side due to the presence of –OH, $–NH_2$, and amide groups [54,55]; chemical derivatization can shift them toward the negative side [56]. Their use in low-impact and transient devices is discussed in Section 10.2.

3.2. Dielectric Properties and Dipole Orientation

An increase in ε_r and polarization can favor charge accumulation and retention and, in certain architectures, increase triboelectric output; however, the relationship is not universally linear, since trap states, interfaces, dielectric strength, and device geometry also come into play [57–59]. High-ε_r materials improve charge storage by reducing the internal electric field and allowing greater surface charge accumulation. For example, Poly(vinylidene fluoride-trifluoroethylene) (P(VDF–TrFE)) exhibits high polarization associated with polar chain conformations and can show, under comparable conditions, a higher device output than PVDF formulations with a lower fraction of polar phases [57]; since that study

addresses hybrid piezoelectric–triboelectric harvesting, the increase cannot be ascribed to triboelectrification alone.

Dipole orientation can be regulated by electrical poling, mechanical stretching, or copolymerization with polar monomers. Enrichment of the β phase by drawing, poling, or suitable processing conditions has been associated, in specific systems, with significant increases in surface charge density and device output compared with films having a lower polar phase content [58,59], although the relative weight of triboelectric and piezoelectric contributions is rarely quantified. Dielectric blending with polar additives (ionic liquids, sulfonated polymers, zwitterions) further modulates polarization and interfacial charge mobility. Since PVDF and its copolymers are also piezoelectric and pyroelectric materials, processing steps that increase the polar phase fraction (stretching, poling, electrospinning, copolymerization) modify the piezoelectric response together with the triboelectric one. Consequently, whenever the triboelectric layer is also deformed, the measured output may include a piezoelectric component; an increase in output can be attributed to enhanced triboelectrification only if the study in question has separated the two contributions—for example by comparing poled and unpoled films (or films consisting of the non-polar α phase) of equal thickness and morphology, by deforming the layer without resorting to the contact–separation mechanism, or by reversing the poling direction (which reverses the sign of the piezoelectric contribution but not that of the triboelectric one). The opposite error, that is, mistaking a triboelectric charge for a piezoelectric output, is a well-documented phenomenon [60], including in bio-based nanogenerators: in cellulose devices, removing the PDMS packaging layer reduced the output by an order of magnitude, which scaled with the composite permittivity rather than with the piezoelectric coefficient d_{33} [61]. Unless otherwise indicated, the improvements discussed below refer to the overall device output and do not necessarily imply a purely triboelectric origin (Section 9.1).

3.3. Chemical Functionalization and Molecular Engineering

Modifying the surface chemistry of polymers allows precise control of electron affinity and interfacial energy through complementary strategies. Fluorination, for example by CF_4 plasma or fluorosilane grafting, accentuates the negative triboelectric character [58,59], while grafting amine or hydroxyl groups introduces positive charge sites and hydrogen bonding capability. On the environmental interaction side, carboxylation or sulfonation increases hydrophilicity and ionic adsorption under humid conditions, while covalent crosslinking with highly polar segments, nitrile, carbonyl, or ether linkers, increases the dipolar density of the matrix.

Recent reports have explored copolymers (e.g., PVDF copolymers such as PVDF–TrFE and Poly(vinylidene fluoride-chlorotrifluoroethylene) (PVDF–CTFE)) in which the monomer composition regulates electron affinity and thus the tribo-negative character: in PVDF–CTFE the chlorinated unit lowers the LUMO of the system and, by modulating the surface Cl/F ratio, allows balancing of triboelectric charge capture and retention [62]. Such molecular engineering strategies enable fine tuning of the dielectric's electronic properties, complementary to the control of mechanical properties discussed in Section 3.7, essential for stable sensing under large deformations.

3.4. Reinforced Polymer Dielectrics and Nanofillers

The incorporation of nanoparticles with high dielectric constant or strong surface charge retention improves the triboelectric performance of polymer matrices; among the most used fillers are $BaTiO_3$, TiO_2, ZnO, SiO_2, and Al_2O_3, as well as carbon nanomaterials (graphene, Carbon nanotubes (CNTs)) and conductive 2D carbides/nitrides (MXenes). The improvement arises from the concurrence of multiple mechanisms: interfacial polar-

ization (Maxwell–Wagner–Sillars effect) increases charge storage capacity, the formation of microcapacitor networks within the polymer amplifies the effective dielectric constant, and local electric field intensification near filler–matrix interfaces favors charge trapping. The optimal concentration is strongly dependent on the matrix–filler combination and often lies in the low or moderate loading regime; beyond this value, aggregation, increased losses, or formation of conductive pathways can reduce the benefit, as in perovskite–PMMA composites whose output peaks at 10 wt% and declines at higher loading (12 wt%) as dielectric loss increases [63]. Increases in V_{OC} and I_{SC} of the order of several times have been reported for specific optimized composites [64,65].

3.5. Micro- and Nano-Structuring of Polymer Surfaces

Surface morphology critically determines triboelectric charge density, since it governs the real contact area, charge trapping, and the capacity of the interposed air layer. Several engineering strategies are used for this purpose: soft lithography and nanoimprinting generate regular micro-pyramids, pillars, or domes; plasma etching and laser ablation induce hierarchical roughness and nano-textures; electrospinning and phase separation produce porous films with high specific surface area. The optimal scale and geometry of the texture depend on the polymer modulus, applied pressure, and contact regime. In representative systems, hierarchical micro/nanometric structures have produced substantial increases in charge density and low-pressure sensitivity, but these gains are not directly transferable between different architectures [66]. In a representative case, a pre-stretched and wrinkled elastomer is used as a transfer stamp to imprint asymmetric textures on PVDF, characterized by adjustable periodicity and amplitude; the stress concentration generated by the asymmetry explains why the optimal texture scale emerges from the morphology, the film modulus, and the contact regime, rather than being defined a priori (Figure S1) [67].

3.6. Interface Modification and Charge Stabilization

The retention and repeatability of surface charge are strongly influenced by trap depth, interfacial energy, and surface contamination [68]. Functional coatings, such as self-assembled monolayers (SAMs), polyionic brushes, or hydrophobic silanes, reduce charge loss and improve environmental robustness. Similarly, the intermediate charge-trapping layers inserted between the triboelectric layer and the electrode limit the dissipation of the triboelectric charge toward the electrode: an intermediate layer consisting of TiO_2–MXene/polystyrene nanofibers, for example, has increased the surface charge density and the output power of a single-electrode TENG [69], while ion-impregnated electrolytic intermediate layers mitigate charge decay thanks to the high capacitance of the ionic electric double layer [70].

For self-powered sensors operating under humid or variable conditions, layered configurations separate the two functions: a hydrophobic outer surface limits moisture absorption, while an underlying layer generates or stores the triboelectric charge [71]. In a representative case, the combination of a superhydrophobic surface with an intermediate charge-storage layer preserved 95.2% of the full-scale output at 99% relative humidity [72]; it has also been demonstrated that tribo-negative bilayer stacks improve both charge generation and charge retention [73].

An equally critical element of the material stack is the electrode, which must ensure electrical conduction without compromising conformability and breathability. For wearable use, elastic and thin electrodes are adopted, silver nanowire (AgNW) networks, Poly(3,4-ethylenedioxythiophene):poly(styrene sulfonate) (PEDOT:PSS) films, graphene, and increasingly conductive ionic hydrogels, which combine extreme deformability and retention of conduction under strain: hydrogel electrodes reinforced with metal–organic

frameworks have shown superior stretchability and durability while maintaining high device performance [27,74,75]. Such electrodes are discussed, on the application side, in Sections 5.2 and 5.5.

3.7. Mechanical Compliance and Flexibility

For wearable and biointegrated sensing, the mechanical compatibility between TENG layers and the host substrate is crucial. The elastomers used cover a wide stiffness range: ultra-soft silicones such as Ecoflex have Young's moduli of ~50–100 kPa and elongation at break up to 500–900%, while standard crosslinked PDMS (e.g., Sylgard 184) is markedly stiffer (~1–3 MPa) with typical elongation at break of 100–150% [76–78]. The choice of formulation thus balances conformability, elastic recovery, and charge retention for the specific wearable application [79]. Crosslink density, filler content, and solvent retention influence both elastic recovery and triboelectric response. Balancing mechanical softness with charge retention remains one of the main design challenges for polymer TENGs [80]. A phase-locked triboelectric gel, for example, reaches a skin-compatible modulus without sacrificing strength or interfacial adhesion, the latter governing the stability of conformal contact (Figure S2) [78].

3.8. Advanced Strategies: Hybrid and Gradient Materials

Recent developments have introduced gradient and asymmetric structures to simultaneously optimize charge generation and mechanical stability. In gradient architectures, a stiffer surface region capable of accumulating high charges is combined with a soft, stretchable inner body: in a gradient interpenetrating polymer network, consisting of a positive triboelectric polymer within an Ecoflex-CNT elastomer, the rigid surface layer cracks and wrinkles under strain, exposing the underlying stretchable layer, such that the short-circuit charge density is maintained even at 100% strain [81]. In structured or composite surfaces, tribo-positive and tribo-negative domains can coexist within a single triboelectric layer: a checkerboard arrangement of opposite polarities balances charge attraction and repulsion at the interface in sliding TENGs, reducing dynamic and static friction by more than 30% and 80%, respectively [82]; alternatively, both polarities can be obtained from the same polymer platform through selective functionalization, as in the case of cellulose and fluorinated cellulose nanofiber pairs [83]. Finally, in ionic polymer TENGs, the integration of ionic liquids or zwitterions generates coupled triboionic outputs [78,84]; the roles of polymer gels as triboelectric layers, electrodes and conductive matrices have recently been reviewed [85]. Taken together, these strategies broaden the design space from conventional dielectrics to systems in which ionic transport, polarization, and mechanics can be coupled.

Critically evaluated, the material-level evidence examined in this section supports qualitative rather than quantitative design rules. Most improvements are reported as gains in the overall device output rather than in triboelectric charge density; in piezoelectrically active matrices, triboelectric and piezoelectric contributions are rarely separated (Section 3.2); and optimal filler loadings and texture scales are specific to formulation and architecture (Sections 3.4 and 3.5). Since such gains are rarely referred to a common counter-material, contact pressure or humidity, the only homogeneous quantitative datasets for material classification remain the quantified triboelectric series [23,86] (Section 9.8), and claims of superior materials should be read in relation to the device in which they were measured.

4. Device Architectures and Signal Characteristics for Self-Powered Sensing

The architectural design of a TENG governs its electrical output, signal stability, and mechanical robustness. In sensing-oriented devices, design therefore prioritizes the stability

of the transfer function, repeatability, and calibration, translating the material properties discussed in Section 3 into specific geometries and readout conditions.

4.1. The Dual Nature of TENG Architectures: Harvester vs. Sensor

A TENG can operate in two distinct regimes (Figure 4).

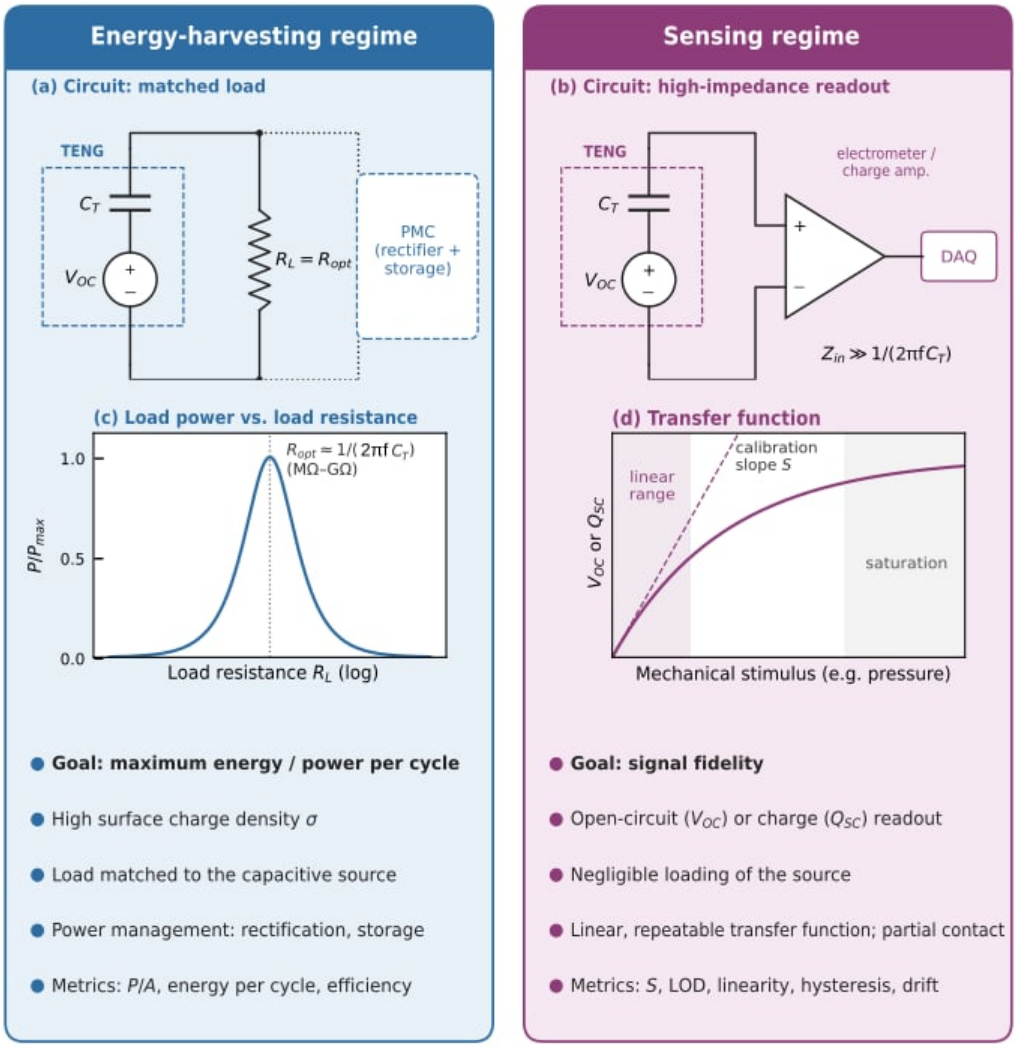


Figure 4. The dual nature of TENG architectures. In the energy-harvesting regime (**a**,**c**), the device, modelled as a V_{OC} source in series with its internal capacitance C_T, drives a load matched to the capacitive source: power transfer peaks at $R_L \approx 1/(\omega C_T)$, typically in the MΩ–GΩ range, and is made usable by a power-management circuit (PMC). In the sensing regime (**b**,**d**), the signal is read either in open-circuit (V_{OC}) mode through a high-impedance voltage stage ($Z_{in} \gg 1/(\omega C_T)$), or in short-circuit charge (Q_{SC}) mode through a charge amplifier holding the device at virtual ground; in both cases the readout does not extract energy from the source; optimization favors a linear, repeatable transfer function, exploited within its initial range before saturation. Qualitative curves; original elaboration by the authors.

In the energy harvesting regime, the mechanical conditions and the electrical load are selected so as to maximize the energy transferred to the load, combining a high charge density, impedance matching and, where necessary, charge management circuits; in resonant architectures, this may involve operation close to a natural frequency. In the sensing regime, the optimization aims at the fidelity of the transfer function: the readout system must not draw energy from the source (cf. Section 4.5) and, to avoid saturation and wear, partial contact amplitudes or small deformations are often used (cf. Section 4.6). For polymer-based

TENG sensors, this balance determines their practical usability in continuous monitoring applications, such as motion tracking, tactile sensing or physiological signal recording.

4.2. Operating Modes and Device Geometries

Four canonical operating modes, established by Wang and co-workers [87] and later compared quantitatively through the figure-of-merit framework of Zi et al., who split the freestanding mode into contact and sliding variants (five configurations; Figure 3) [22], define the operational diversity of triboelectric devices and are today expressed in a wide range of application variants [45]. In the vertical contact-separation mode, two layers come into contact and separate perpendicularly; from a construction standpoint, this is a "sandwich" configuration (for example, PDMS–Al), the most widely used for pressure, impact and vibration sensing. In the lateral sliding mode, tangential sliding modulates the overlap area, generating a continuous signal suitable for monitoring linear and rotational movements as well as for tactile sensing. In the single-electrode mode, one electrode is referenced to the environment, making it possible to detect freely moving objects or the human body; however, the response depends on parasitic capacitance and on the reference path to ground, factors that must be taken into account during calibration. In the freestanding triboelectric-layer mode, a charged moving layer induces alternating potential differences between two fixed electrodes, under contact or non-contact conditions [42,88]; this configuration is typical of vibration, flow and position sensors. Their relative performance as generators, quantified by the structural figure of merit, is summarized in Section 2.4 (Figure 3) [22]. These classifications, referring to generators, do not translate directly into metrics for sensors: in the sensing field, contact-separation and single-electrode modes are preferable for their simplicity and ease of integration. Hybrid architectures, which combine sliding and separation or integrate microstructured spacers, can further extend the dynamic range (Section 4.7).

4.3. Mechanical–Electrical Transduction Path

The output electrical quantities reflect the dynamic history of the mechanical state, but with distinct roles. In idealized models and for a fixed geometry, the open-circuit voltage predominantly reflects the state of separation, while the current strongly depends on the rate of change of the electromechanical state (Section 2.2). The open-circuit relation of Equation (2) [89] assumes full contact and a uniform charge density. For partial contact, it can be extended phenomenologically by replacing σ with an effective charge density weighted by the instantaneous real contact area:

$$V_{OC}(t) \approx \frac{\sigma_{eff}(t)x(t)}{\varepsilon_0} \text{ with } \sigma_{eff}(t) = \frac{\sigma_0 A_{eff}(t)}{A} \quad (7)$$

where σ_{eff} also depends on the surface state. Equation (7) is a quasi-static approximation, not a general consequence of Equation (2); its application to the pressure regime is developed in Section 5.1 (Equation (8)). Within this approximation, any variation in pressure, deformation, or vibration modulates σ_{eff} and x, producing a measurable voltage transient. This direct coupling constitutes the basis of TENGs as self-powered sensors, where electrical readouts encode mechanical dynamics without bias current.

4.4. Electrical Signal Characteristics

The triboelectric signal exhibits several attributes that distinguish it from other transduction mechanisms.

As regards polarity, the output of conventional TENGs is typically alternating and reverses its sign at each contact–separation cycle; direct-current variants, based on mechanical

rectification, localized electrical discharge in air, or the tribovoltaic effect at semiconductor junctions, forgo this characteristic, while nonetheless entailing different constraints in terms of impedance and materials [90–92].

Current and delivered power increase with excitation frequency, whereas V_{OC} is, to a first approximation, frequency-independent (cf. Equations (2) and (4), Section 2.2); the response to force is nonlinear and saturates at high loads (cf. Section 4.6). TENGs are particularly sensitive to variations in contact state: a load held without further motion does not sustain a continuous current and, due to relaxation and charge losses, does not allow a direct static measurement equivalent to that of a resistive or capacitive transducer. With a high-impedance readout, the voltage can persist for a few seconds after motion stops: a preliminary stretch sensor tested on a motorized joint platform held its output for about 7.5 s through a buffer stage before charge dissipation set in, enough for quasi-static angle readout [93]. The measurement was, however, relative rather than absolute, since each voltage increment depended on the preceding output, and it does not amount to a sustained static measurement. This characteristic makes the device especially suited to dynamic stimuli and motivates, when the static component is required, integration with complementary transduction modes. The high voltage amplitude obtainable in many architectures can reduce the need for voltage gain; however, a high-impedance input stage and appropriate signal conditioning remain essential, as discussed in Section 4.5.

For sensing purposes, the waveform morphology (rise/fall times, asymmetry, peak ratio) contains information about the type of stimulus and the mechanical regime, going beyond simple peak amplitude. The waveform thus serves as a sensory signature: based on it, pressure sensors distinguish the intensity and duration of a contact, vibration sensors reconstruct frequency spectra, and wearable devices identify movement or gait [19].

4.5. Load Impedance and Signal Conditioning

The load impedance strongly influences both the output waveform and the sensing accuracy. A TENG behaves as a high-impedance capacitive source, whose internal capacitance C_T typically ranges from tens to hundreds of pF for cm^2-scale devices. The choice of readout depends on the application objective: in energy harvesting the optimal load is determined experimentally or via the equivalent model, whereas in sensing the readout must not extract energy from the source, which can be achieved in two complementary ways. In voltage mode, the open-circuit voltage is read through a stage whose input impedance greatly exceeds $1/(2\pi f\, C_T)$; since this quantity reaches the GΩ range at frequencies of a few hertz, a standard oscilloscope input (1–10 MΩ) loads the device heavily, and electrometer-grade inputs (of the order of 10^{14} Ω) are required. In charge mode, a charge amplifier holds the device at virtual ground, i.e., in short-circuit condition, and integrates the transferred charge on a feedback capacitor C_f, so that the output ($V_{out} = -Q_{SC}/C_f$) is largely insensitive to cable and parasitic capacitances; its low-frequency limit, set by the feedback network, must however be matched to the time scale of the stimulus. Signal conditioning circuits, charge amplifiers, rectifiers, and RC filters, convert the triboelectric pulses into quasi-continuous or frequency-domain signals compatible with microcontrollers or wireless transmitters. More recent research aims to further reduce the interface electronics, even realizing battery-free sensor nodes: an example is the integration of the triboelectric transducer with passive wireless communication schemes, in which the triboelectric pulse itself carries the information without dedicated modulation and power management stages [94].

4.6. Dynamic Response and Calibration

For use as sensors, TENGs must exhibit predictable and repeatable responses under cyclic loading, and reproducible ones across devices. Recalling the definition of sensitivity

introduced in Section 2.4 (Table 1), dynamic characterization verifies its stability and linearity under repeated stress. Calibration curves frequently exhibit an initial quasi-linear range followed by a progressive reduction in slope when the real contact area approaches saturation; the position and extent of these regimes depend on the microstructure and compliance of the device. Similarly, response times below 100 ms have been reported in numerous tactile sensors, but they must be interpreted together with the test conditions and the instrument bandwidth.

Noise and drift arise mainly from charge losses, surface wear, and humidity (Section 8). Commonly targeted (not universal) values are hysteresis <5%, a stable baseline, and durability beyond 10^4 cycles, as in environmentally tolerant and self-healing devices [84] and in single-electrode triboelectric units with an MXene/silicone nanocomposite dielectric, whose output remains stable over 5×10^4 cycles [95]. Figure 5 illustrates this characterization using a single-electrode triboelectric unit: the short-circuit current scales linearly with contact speed, the open-circuit voltage increases monotonically with the imposed displacement, and the output remains stable over tens of thousands of cycles, illustrating, qualitatively, the requirements regarding linearity, calibration, and durability [95] (cf. its MIS-TENG coding in Section 9.4.1).

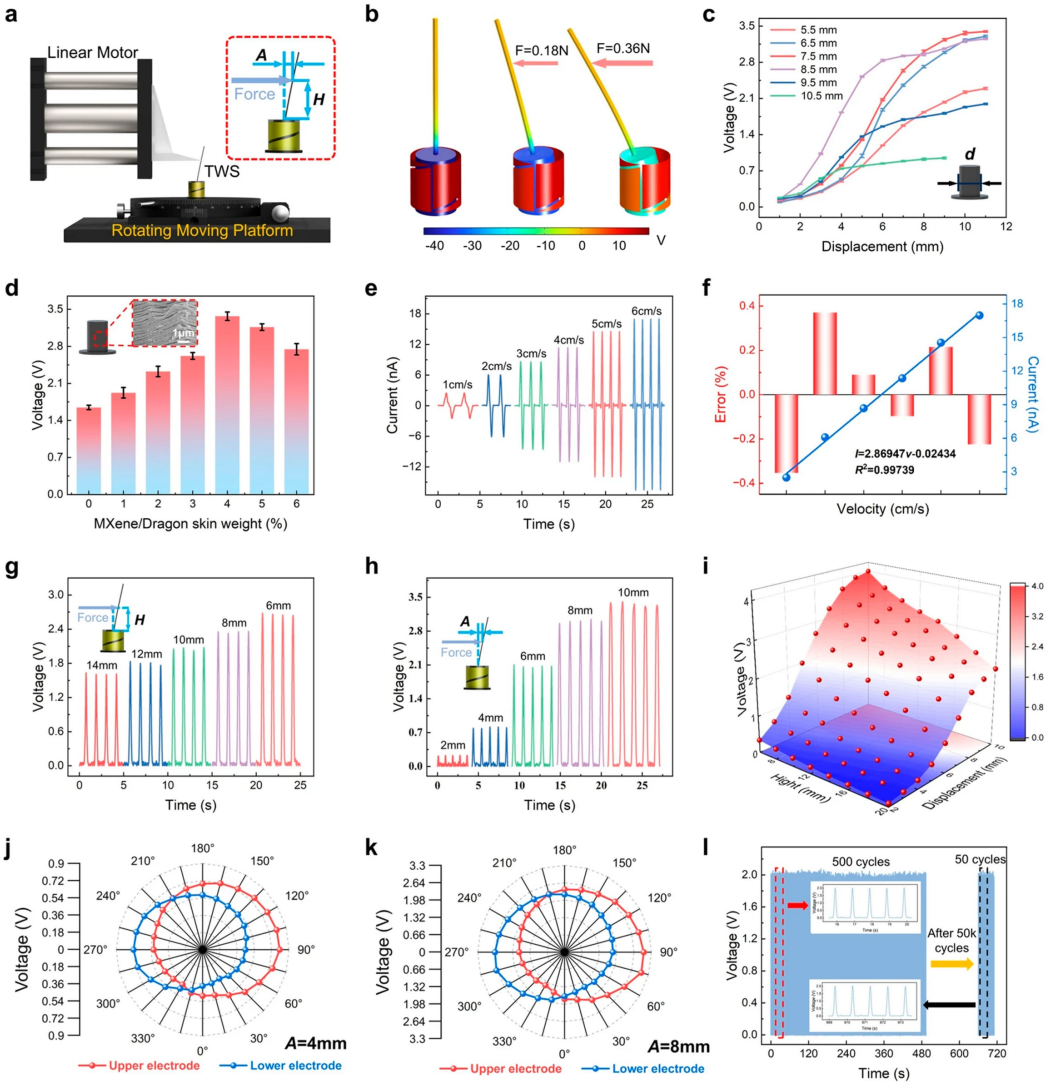


Figure 5. Dynamic characterization of a single-electrode triboelectric whisker unit with an MXene/silicone dielectric: (**a**) test setup; (**e**,**f**) short-circuit current versus contact velocity (1–6 cm s^{-1}) and its linear fit; (**g**–**i**) open-circuit voltage versus contact height (6–14 mm) and load displacement

(2–10 mm); (**l**) durability over 50,000 cycles. Panels (**b**–**d**,**j**,**k**) report simulation, optimization of geometry and composition, and directional response. Reproduced from Wang et al. [95], Nano-Micro Lett. 2026, 18, 76, Figure 2; © 2026 The Authors, published by Springer Nature CC BY 4.0, licensed under CC BY 4.0.

4.7. Hybrid and Multilayer Architectures

To balance signal intensity and mechanical resistance, several hybrid configurations have been developed, each oriented toward a specific compromise. In multilayer configurations, the alternation of tribo-positive and tribo-negative films multiplies the contact interfaces activated by a single stress, increasing the total charge per stimulus for a given footprint; however, the increase is sublinear with respect to the number of units, since part of the mechanical energy is dissipated during transfer between layers and not all units achieve full contact; consequently, for the same total contact area, a single-layer device can deliver a higher power density than a zigzag configuration [96]. In the field of sensing, stacked layers can also encode a single touch into multiple output pulses [97]. The spacers, in turn, define the air gap and, consequently, the sensitivity regime: a spacer layer that establishes the gap and transfers pressure to a porous dielectric ensures a steep low-pressure response while maintaining a wide detection range [98], and a braided mesh spacer, which separates two coaxial electrodes, stabilizes the output of triboelectric yarns for respiration monitoring [99]. A further family is that of hybrid piezo-triboelectric devices, in which PVDF-based piezoelectric layers operate in synergy with triboelectric surfaces: the coupling of the two mechanisms enables dual-mode sensing and, at the same time, energy harvesting, although attributing output changes to either mechanism requires the controls discussed in Section 3.2. Porous and textile three-dimensional architectures, with sponge-like morphologies, finally extend the principle to the compressible and omnidirectional regime, integrating natively into wearable fabrics. Taken together, these approaches improve linearity, elasticity, and fatigue resistance, essential requirements for continuous monitoring under real conditions [100,101].

4.8. Toward the Self-Powered Multimodal Sensor

By combining TENG elements of different geometries and polarities, a multimodal sensor can be obtained, simultaneously sensing pressure, deformation, vibration, or temperature through characteristic output signatures [102]. At the architectural level, matrices of individually addressable triboelectric cells map the spatial distribution of the stimulus; their output signatures (cf. Section 4.4), decoded by machine learning algorithms, enable gesture recognition and high-precision tactile mapping [95], paving the way for self-powered electronic skins (e-skin). Integration with wireless modules (Bluetooth Low Energy (BLE), or battery-free NFC powered by the reader's field) and low-power edge processors turns these systems into IoT nodes whose energy autonomy must be assessed for the whole chain (Section 6.3). In a reconfigurable whisker array, for example, a convolutional neural network classifies twenty surface profiles with an overall accuracy of 97.4%, demonstrating that the temporal signature encodes geometric attributes that peak amplitude alone is unable to capture (Figure S3) [95].

Overall, the set of architectural solutions for sensing is broader than the corresponding metrological validation. Geometry and the readout system determine the transfer function; however, the readout conditions that define it (input impedance or feedback capacitance, sampling frequency, filtering) are among the least frequently documented parameters (Section 9.4.1). Moreover, the inability of the triboelectric element to measure loads sustained over time (Section 4.4) makes it necessary to resort to hybrid transduction in architectures intended for static pressure measurement. Sensing-oriented design is

therefore less mature than design aimed at energy harvesting, a field for which figures of merit [22,30] and standardized test methods [103,104] already exist.

5. Polymer-Based TENGs for Mechanical Sensing (Pressure, Strain, Vibration)

Mechanical sensing of pressure, strain, and vibration represents the most mature application of TENGs, given its relevance to wearable electronics, soft robotics, tactile interfaces, and structural monitoring; this section summarizes the operating principles, architectures, and benchmark parameters for these three types of stimuli. As throughout this review, "self-powered" refers to the transduction stage (Section 1.3): the TENG output is the sensing signal, whereas readout and conditioning electronics are externally powered unless stated otherwise.

5.1. Pressure Sensing: From Tactile Pixels to E-Skins

Pressure sensing is the archetypal TENG application and relies on the contact-separation mode (Section 4.2). Evaluating Equation (7) between the unloaded and the loaded state gives the pressure-dependent signal:

$$\Delta V_{OC}(P) \approx \sigma_{eff}(P) \cdot \frac{[x_0 - x(P)]}{\varepsilon_0}, \quad with\ \sigma_{eff}(P) = \frac{\sigma_0 \cdot A_{eff}(P)}{A} \tag{8}$$

where σ_0 is the charge density at full contact, $A_{eff}(P)/A$ the fraction of real contact area, x_0 the unloaded separation, and $x(P)$ the residual separation under load. Pressure increases the first factor and, by reducing the residual separation $x(P)$, also increases the second, so that both raise ΔV_{OC}; the response becomes sublinear as A_{eff} approaches A and $x(P)$ its minimum (Section 4.6). Microstructured surfaces (domes, pyramids, wrinkles), most effective below about 10 kPa, act mainly on the first term; spacers and porous dielectrics act mainly on the second (Section 4.7).

Published sensitivity values span several orders of magnitude, because they depend not only on the architecture but also on the pressure range over which the slope is calculated. Values from about 10^{-2} up to tens of V kPa^{-1} have been reported, with operating ranges extending to hundreds of kPa, response times on the order of tens of milliseconds, and durability up to 10^5–10^6 cycles in selected devices [19,46,105,106]. These values should not, however, be interpreted as directly comparable benchmarks in the absence of homogeneous test protocols. The lower detection limit of most devices is on the order of pascals. A direct comparison with human touch is not straightforward, since psychophysical thresholds are expressed in terms of cutaneous indentation rather than pressure, with median values of about 10 µm on the fingertips and the volar surface of the fingers [107]. Only a few architectures have pushed the detection limit into the sub-pascal regime, thanks to porous microstructures that amplify deformation under low loads (150 mPa) [98] or micropillar interfaces capable of detecting the mechanical pulsations of cardiomyocyte monolayers below 1 Pa [108]; values on the order of 0.1 Pa therefore represent record rather than typical performance. Since the triboelectric element alone is unable to measure a constant load (cf. Section 4.4), electronic skins (e-skin) that must detect both dynamic and static components integrate a complementary modality, typically piezoresistive [105].

5.2. Strain Sensing: Elastic and Wearable Transducers

While pressure sensors rely on normal compression, strain sensors utilize the stretching or lateral bending of polymeric TENGs. The resulting changes in contact area, dielectric thickness, and capacitance alter charge induction and the output signal. Since polymer

films can withstand significant stretching, TENGs can transduce movements such as joint bending, muscle contraction, or body deformation (corresponding wearable biomedical applications are discussed in Section 6.2).

From a design perspective, two main strategies can be distinguished. Sliding-mode TENGs (cf. Section 4.2), often embedded in elastomeric or textile substrates, are used for in-plane deformation sensing. Conversely, for out-of-plane sensing, flexible bilayers or fiber-based TENGs bend in unison with the substrate, generating an alternating charge flow proportional to the curvature. Fiber-shaped TENGs, fabricated by twisting tribo-positive and tribo-negative polymer fibers (e.g., nylon and PTFE), offer one-dimensional architectures ideal for smart garments or joint-motion sensors [109–111]. In a representative example, a particulate PTFE dielectric decouples stretchability from the rigidity of the triboelectric film (Figure S4) [110].

In the devices described in the literature, the strain range can reach values on the order of 100–200%, while sensitivity is reported in heterogeneous forms, for example, as voltage at a fixed strain [112] or per degree of joint bending [113], thus depending, like response time and hysteresis, on the geometry and on the very definition of strain; extensibility alone does not guarantee a monotonic response to strain, since the output of some stretchable devices decreases as elongation increases under a constant applied force. A numerical comparison among the various studies is therefore meaningless in the absence of a common protocol (Section 9). Fiber-based architectures can amplify contact modulation at low deformation levels (representative metrics in Table 3); as with other stimuli (cf. Section 4.4), the waveform encodes the amplitude and rate of deformation, enabling motion reconstruction. For example, a helical-structure fiber strain sensor, based on a nylon-PTFE pair and sensitive to tensile strains of less than 1%, records signals associated with respiration, heartbeat, and joint flexion (fingers and knee) in a self-powered manner [112].

Table 3. Examples of polymer-based TENGs for mechanical sensing (pressure, strain, vibration): material system, transduction mode, main reported parameter, response time, operating range and durability. The values are given as reported in the original studies, with the test conditions in parentheses. A direct comparison between the different rows is not possible: the nature of the main parameter varies (voltage per unit pressure, voltage at a fixed strain, frequency error), the response times were obtained with different loading rates, and the durability refers to non-homogeneous cycling protocols (Section 9.4.1).

Application	Typical Polymer System	Mode	Sensitivity/ Main Metric	Response Time	Operating Range	Cycles	Ref.
Pressure (HMI/keyboard)	Silicone rubber (gradient)–foam	Contact-separation	0.011 V kPa^{-1} (0–18 kPa)	25 ms (recovery 71 ms) at 8 kPa, 0.5 Hz	≈0–30 kPa	≈4.5×10^3 ‡ (27 kPa, 0.5 Hz, 2.5 h; stable at 20 d)	[46]
Strain (wearable)	Helical fiber (fiber TENG)	Stretching (contact-separation)	0.5 V at $\varepsilon = 1\%$ (LoD < 1%)	70 ms (recovery 71 ms) at 5 Hz; 180 ms at 2 Hz	1–80%	2×10^4	[112]
Vibration (structural)	Silicone rubber–latex (coaxial fiber)	Contact-separation (fiber, single electrode)	0.32% freq. error *	-	0.1–100 Hz	≈4.6×10^4 ‡ (≈1530 s at 30 Hz)	[114]

‡ Derived from test duration and frequency; the number of cycles is not stated in the source. * Frequency accuracy (not voltage sensitivity), from a single comparison with a commercial accelerometer on one diesel engine (47.025 vs. 46.875 Hz).

5.3. Vibration and Dynamic Motion Sensing

In addition to quasi-static deformation, TENGs are suitable for detecting dynamic vibrations, with a typical bandwidth ranging from a single hertz to several hundred hertz, and extending, in the most recent architectures, up to the kilohertz range. In vibration-mode sensors, the periodic displacement between triboelectric layers induces alternating potential differences whose frequency and amplitude directly correspond to mechanical oscillations.

The mechanisms employed differ according to the quantity to be captured. Resonant TENGs, coupled to cantilevers or membranes, exploit vibration at well-defined natural frequencies; when the input is instead a rotation or an air flow, self-powered rotary TENGs, with disk architectures, return a periodic AC output; for linear acceleration, finally, mass-spring systems with vertical oscillation convert it directly into voltage pulses. Spectral analysis of the AC waveform (cf. Section 4.4) reveals amplitude, frequency, and pattern of vibration, enabling structural health monitoring and machine diagnostics. A recent example recognizes rotor-imbalance states with more than 98% accuracy under laboratory conditions, the authors noting that cross-machine and long-term industrial validation are still required [115].

Resolution, sensitivity, and durability depend on the mechanical dynamics of the resonator and on the readout method; therefore, comparison with electromagnetic, capacitive, or optical technologies must be made at equal bandwidth, mass, geometry, and excitation conditions. The most recent architectures have drastically broadened the band: by introducing a magnetically optimized quasi-zero-stiffness structure, Wu et al. realized a triboelectric sensor capable of covering 2.5 to 4000 Hz with an acceleration sensitivity that varies with frequency between 0.32 and 134.9 V g^{-1}, recognizing the operating state and fault type of mechanical components with 98.9% accuracy using machine learning algorithms [116]. Polymer-based vibration TENGs using FEP or PTFE films demonstrate excellent durability and environmental resilience [116,117], while flexible solutions, from stretchable PVDF–PDMS composite films to coaxial fiber architectures, extend their applicability to curved or moving surfaces [114,118]. Figure 6 documents the frequency and acceleration behavior of the quasi-zero-stiffness sensor [116], showing how the output remains measurable over more than three decades of frequency and responds linearly to acceleration at each frequency above 400 Hz, with slopes of 0.08–2.81 V g^{-1}, which are much lower than the peak sensitivity reached elsewhere in the band.

5.4. Signal Interpretation and Multimodal Sensing

Applied to mechanical stimuli, the multimodal architectures described in Section 4.8 are able to distinguish between normal and tangential stresses, or to resolve multiaxial deformations, by combining elements with orthogonal orientations or pairs of different polymers. Waveform analysis algorithms (Fast fourier transform (FFT), correlation analysis, neural networks) extract in real time mechanical or physiological information, such as gait symmetry or heartbeat [19,114,119]; moreover, the use of Long Short-Term Memory (LSTM)-type recurrent neural networks, applied jointly to triboelectric and piezoresistive signals, has made it possible to identify the type of material touched with an accuracy of 96.8% [105].

5.5. Durability and Mechanical Reliability

In mechanical sensing, repeated contact and sliding impose severe requirements on wear resistance and stability of the polymer–electrode interface. Elastic spacers, conformal electrodes, and liquid, quasi-liquid, or self-healing interfaces can reduce abrasion and preserve electrical continuity [84,120]. Degradation mechanisms, charge retention, and mitigation strategies are systematically analyzed in Section 8.

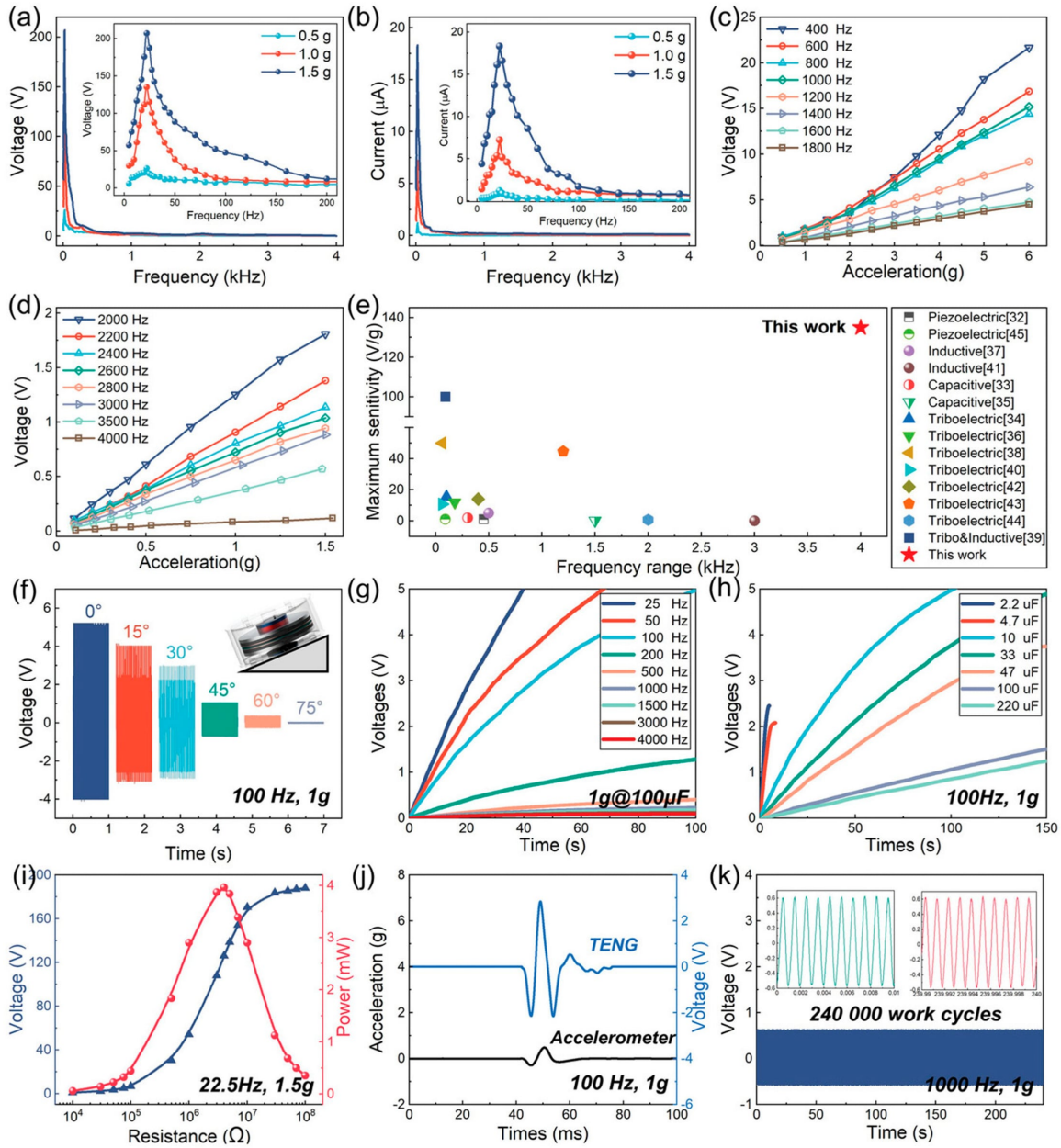


Figure 6. Output of a quasi-zero-stiffness triboelectric vibration sensor (HSVS-TENG): (**a**,**b**) open-circuit voltage and short-circuit current from 2.5 to 4000 Hz at different accelerations; (**c**,**d**) open-circuit voltage versus acceleration, linear above 400 Hz with slopes of 0.75–2.81 V g^{-1} (400–1800 Hz, 0.5–6 g) and down to 0.08 V g^{-1} (2000–4000 Hz, 0.1–1.5 g); (**k**) open-circuit voltage over 240,000 cycles at 1000 Hz. The panels (**e**–**j**) report comparison with other sensors, angular response, capacitor charging, load characteristics, and pulse response. Reference numbers in panel (**e**) refer to the source article. Reproduced from Wu et al. [116], Adv. Sci. 2023, 10, 2301199, Figure 3; © 2023 The Authors, published by Wiley-VCH GmbH, licensed under CC BY.

5.6. Benchmarking of Mechanical TENG Sensors: Representative Examples and Limitations

Table 3 collects three representative cases, one for each of the stimulus classes treated in Sections 5.1–5.3, reported with their respective test conditions, so as to make explicit the dispersion of published metrics and the reasons why direct comparison between studies remains problematic (cf. Section 9.1).

The resulting picture is both encouraging and instructive: the three devices cover pressure, strain, and vibration with useful performance and without biasing the transducer, but the main metric changes in nature from row to row, voltage per unit pressure, voltage at fixed strain, percentage frequency error, and the reported durations refer to non-homogeneous cycling protocols. The heterogeneity of these three entries alone concretely illustrates the metrological gap that the MIS-TENG framework (Section 9.4) is intended to help fill; their coding against the MIS-TENG checklist is reported among the case studies of Section 9.4.1.

6. Polymeric TENGs for Wearable and Biomedical Sensors

The integration of polymeric TENGs into wearable and biomedical platforms makes it possible to use body movement both as an information source and, in certain architectures, as an energy source. Adaptable materials, biocompatible design, energy management, and wireless electronics are expanding the possibilities of continuous physiological monitoring, within the limits of self-powering at the transducer level, as discussed in Section 1.3. The terms "self-powered", "battery-free" and "autonomous" are used as defined in Section 1.3.

A caveat applies to the whole section. Most of the biomedical demonstrations discussed below are proof-of-concept or benchtop studies (L1), pilot tests on small groups of healthy volunteers (L2), or preclinical animal studies (L3); none of the cited works reports validation against a clinical reference method in the target patient population (L4–L5; Table 4, Section 6.3). Throughout this section, "biomedical" and "physiological monitoring" therefore denote the intended application domain and the recorded signal, not demonstrated diagnostic or clinical performance.

6.1. Wearable Motion and Gesture Sensing

The mechanical movement of the human body, walking, running, joint flexion, and respiration, constitutes an intermittent but widely available source of excitation for wearable TENGs. When integrated into fabrics, footwear, or joint supports, polymeric TENGs can convert these movements into dynamic voltage pulses usable as motion signals and, after rectification and storage, as harvested energy, although the two functions involve the trade-offs discussed in Section 4.1.

The architectures described in Sections 3–5 are reconsidered here from the standpoint of wearability: textile integration, washability, breathability, skin conformity, and electrode stability under deformation become design criteria at least as important as signal amplitude. Elastomeric films, triboelectric fibers, and functionalized fabrics are therefore combined with conformal electrodes, for example metallized fibers, PEDOT:PSS, or percolative networks, to preserve electrical continuity during use [109,121,122].

On these material foundations, wearable polymeric TENGs cover a broad spectrum of motion-sensing functions. In joint and limb monitoring, textile patches sewn onto the knee or elbow produce voltage patterns that differ with flexion angle and activity (walking, stepping, running), transmitted via Bluetooth to a mobile application in a single-wearer demonstration [121]. In gait and posture recognition, elements integrated into insoles or footwear straps identify step cadence and plantar pressure distribution, with potential relevance for rehabilitation and sports analysis, which remains to be assessed in user studies [109]. Finally, in human–machine interfaces, devices mounted on fingers or the palm act as gesture controllers for robotic or virtual-reality systems, often in combination with machine-learning algorithms that classify waveform patterns [122], with about 98% accuracy under five-fold cross-validation [123]; simpler rule-based recognition has also reached 95.0% across 1200 trials from 12 participants on a textile sleeve (91–98% per participant) [124]. The reported results vary considerably depending on the architecture and testing method; peak values alone do not demonstrate that a wireless node can be

made operational, since this requires rectification, storage, and power management systems. Durability tests on woven implementations reach about 10^5 cycles (6 Hz, 300 N) [121], under non-uniform stress protocols (Sections 8.7 and 9.3).

6.2. Physiological and Biosignal Monitoring

In addition to macroscopic movement, polymeric TENGs can transduce weak biomechanical stresses associated with pulse, respiration, muscle contraction, and phonation. In more complex bioelectronic platforms, the TENG can also be integrated with electrophysiological electrodes or electrochemical sensors; in these cases, it is important to distinguish the triboelectric sensing/energy-harvesting function from the biopotential acquisition or chemical recognition function.

6.2.1. Heartbeat and Pulse-Wave Sensing

Ultrathin TENG patches applied to superficial arterial sites (wrist, neck) detect the weak pressure pulsations of the vessel wall, on the order of kilopascals or lower, translating them into distinct voltage oscillations synchronized with the cardiac cycle [125,126]. Beyond arterial sites, a single-electrode PTFE/nickel sensor placed on the lower sternum has recorded seismocardiographic chest-wall vibrations, with a sensitivity of 3.76 V N^{-1} below 200 mN and a 0.5–25 Hz frequency response [127]. Contact sensitivity and surface adaptation are maximized by the use of microstructured surfaces and suitably selected triboelectric pairs: in single-electrode or contact-separation devices, the tribo-negative layer (PTFE, PVDF, or PDMS) is paired with a material that occupies a distant position in the triboelectric series, such as nylon [23] or the skin itself, since PTFE and PDMS, which occupy close positions, do not by themselves constitute an efficient pair. Where PVDF is used, the pulse-induced deformation of the layer can also produce a piezoelectric contribution to the signal (Section 3.2). Polyurethanes can serve as a positive counterpart only in specific formulations, since their triboelectric position depends strongly on composition: an abrasion-resistant polyurethane rubber, for example, is located near PTFE in the quantified series [23]. From the morphology of the pressure wave (systolic peak, reflection wave, and dicrotic notch), it is possible to derive heart rate, Pulse-wave velocity (PWV), and stiffness indices [126,128], although in the cited demonstrations these were obtained from a single subject without comparison against a reference method [126]. By combining pulse transit time (PTT) with calibrated models, these sensors also enable continuous, cuffless estimation of blood pressure; in a recent five-participant study, an architecture enhanced by transfer learning provided stable pressure estimates over a six-month follow-up: model adaptation reduces the error in mean arterial pressure by about 27% compared with non-updated models, bringing it to around 3 mmHg with the most effective algorithms [125]. The reported figure is a mean absolute error and is not directly comparable with the acceptance criteria of clinical standards, which for intermittent automated devices require a mean difference ≤ 5 mmHg with a standard deviation ≤ 8 mmHg against a reference method, over populations of prescribed size and blood-pressure distribution [129]; cuffless and continuous devices are further addressed by dedicated protocols [130,131] against which triboelectric sensors have not yet been validated [125].

6.2.2. Respiration and Phonation Sensing

Thoracic expansion and airflow induced by breathing generate triboelectric outputs in flexible TENGs integrated into fabrics, belts, or masks: signal frequency and amplitude correlate with respiratory rate and tidal volume, to the point that, in a pilot study on seven healthy volunteers, a dedicated device reconstructed in real time not only respiratory rate (with a mean absolute error below 0.2 breaths/min) but also the FEV_1/FVC ratio, with a mean absolute error of about 2.4% compared with a reference spirometer [132,133]; patients

with respiratory disease have not yet been tested. Integration into smart masks, combined with superhydrophobic and antifouling coatings capable of neutralizing the humidity and particulate matter present in exhaled air, enables prolonged recording of respiratory rhythms; apnea-like events have been reported, but the detection of sleep apnea syndromes in diagnosed patients, confirmed by polysomnography, has not yet been documented [132] (Table 4). Similarly, patches applied to the throat capture vocal-cord vibrations for speech recognition, proposed as a basis for speech rehabilitation tools, returning millivolt-level signals with response times below 50 ms [134].

6.2.3. Muscle Activity and Joint Movement

When applied to muscles or tendons, flexible TENGs record the skin deformation associated with contraction and relaxation (based on the same strain transduction principle described in Section 5.2), thus providing a mechanomyographic rather than myoelectric signal, without the need for the conductive gel required by "wet" Electromyography (EMG) electrodes. In a representative device, an Ecoflex layer coupled to a small aluminum electrode, positioned on the forearm, made it possible to monitor the movements of the flexor muscles and related tendons, distinguishing individual finger movements and generating distinct waveforms when a single user emulated the motor patterns of different MDS-UPDRS severity levels [135]; subsequently, a stretchable hybrid triboelectric–piezoelectric device, applied to the biceps brachii muscle of three healthy volunteers, was compared with surface EMG signals recorded simultaneously; the Pearson correlation coefficients between the temporal trends of the two signals ranged from 0.89 to 0.91. The authors present this device as a mechanical sensing modality, intended as a complement to EMG rather than a replacement for it [136]. This approach has also been extended to implantable configurations: a helical-fiber TENG (organogel electrode and silicone dielectric inside an Ecoflex tube), implanted above the knee of rabbits ($n = 6$), produced signals that varied with flexion angle and frequency, remained stable after 7 days, and elicited a milder foreign-body response than a stainless-steel control after 4 weeks. The signal, acquired with an electrometer, reflects the combined stretch of the patellar ligament and compression by the surrounding muscle, rather than a calibrated measurement of deformation [137].

6.2.4. Electrophysiological Interfaces Integrated with TENGs

In hybrid electrophysiological platforms, it is necessary to distinguish the electrode function from that of the TENG. Conductive hydrogels and ionic materials can act as dry or conformable electrodes for Electrocardiogram (ECG), EMG, Electroencephalogram (EEG), or Electrooculography (EOG) acquisition, while the triboelectric element can contribute, after rectification and storage, to powering the conditioning electronics, or add a complementary biomechanical channel [134]. Platforms based on collagen–carbon dot matrices or stretchable ionic hydrogels have demonstrated the recording of multiple biopotentials, but such acquisition remains electrophysiological and does not derive directly from the triboelectric effect [138]. The distinction has a mechanistic basis, illustrated in Figure 7: in the ionic conductor, charge is carried by ions, and the electric double layer at the ionic-electronic interface couples it to the electronic current in the external circuit, such that the hydrogel itself can serve as the generator's electrode without the triboelectric signal coinciding with the acquired biopotential [134].

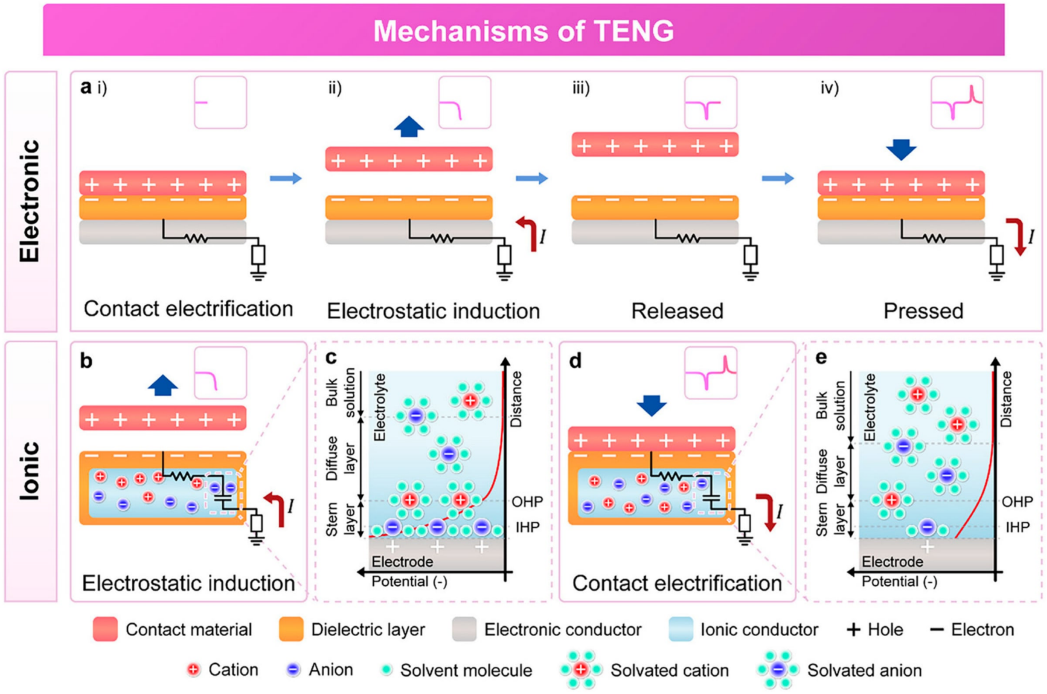


Figure 7. Operating mechanisms of electronic-conductor and ionic-conductor TENGs. (**a**) In electronic-conductor devices, electrostatic induction drives electrons in the external circuit. (i) Contact electrification: Physical contact between the contact material and the dielectric layer generates equal and opposite triboelectric charges on their surfaces, with no current flow in the external circuit. (ii) Electrostatic induction: As the two layers separate, the resulting potential difference drives electrons from the ground to the electronic conductor, producing a positive current pulse (I). (iii) Released: Once maximum separation is reached, electrostatic equilibrium is established and the current returns to zero. (iv) Pressed: When the contact material approaches the dielectric layer again, electrons flow back to the ground, generating a reverse (negative) current pulse. (**b**–**e**) In ionic-conductor devices, the triboelectric charge redistributes ions and forms an EDL at the electrode–electrolyte interface, described by the Gouy–Chapman–Stern model [139] with inner and outer Helmholtz planes [140]; pressing and releasing the contact material release cations and trigger anion migration, so that the potential decays. Reproduced from Choi et al. [134], Adv. Mater. 2026, 38, e17321, Figure 2; © 2026 The Authors, published by Wiley-VCH GmbH, licensed under CC BY.

6.2.5. TENG-Assisted Biochemical Sensing

In sweat-analysis platforms, TENGs generally act as an energy source or as a coupling element, while analytical selectivity is provided by the electrochemical transducer and its recognition elements. Alongside the biomechanical signal, the most recent frontier extends the triboelectric platform to non-invasive biochemical monitoring, overcoming the limitation of mechanical quantities alone. In this domain, the TENG serves a dual function: on the one hand, it provides the electrical stimulus that drives iontophoretic sweat extraction even in sedentary or elderly subjects, in whom spontaneous sweating is insufficient; on the other, in synergy with sweat-activated batteries, it powers the conditioning electronics, while data are read out by NFC powered by the reader's RF field, so that the system operates without conventional pre-charged batteries but is not fully autonomous. By integrating microfluidics and selective electrodes, such platforms quantify in real time sweat electrolytes (sodium and potassium ions and pH [141]) and, in broader implementations, metabolites such as glucose, lactate, and uric acid [142], potentially adding biochemical information to the hemodynamic and respiratory signals discussed above. The convergence of energy harvesting, biofluid extraction, and electrochemical biosensing in a single wearable patch therefore outlines an emerging class of sweat biosensors powered by TENGs; their use in

health monitoring will require validation of the measurements performed on sweat against laboratory reference methods and, in the case of metabolites, verification of the correlation between sweat and blood concentrations, aspects that have not yet been documented for such platforms (Table 4) [141,142].

6.3. Toward Battery-Free and Autonomous Physiological-Signal Monitoring Systems

A typical system organizes the chain, from transduction to data readout, on a single platform along three paths (Figure 8): an energy path, in which a rectifier and a storage capacitor enable duty-cycled operation of a microcontroller and a radio module once a threshold voltage is reached; a signal path, which conditions and digitizes the waveform; and a data path toward an external device, where an algorithm extracts the physiological parameters. Keeping the energy path and the signal path separate, by using dedicated electrodes or alternating time windows, prevents the storage stage from loading the source, which would distort the waveform (Section 4.1).

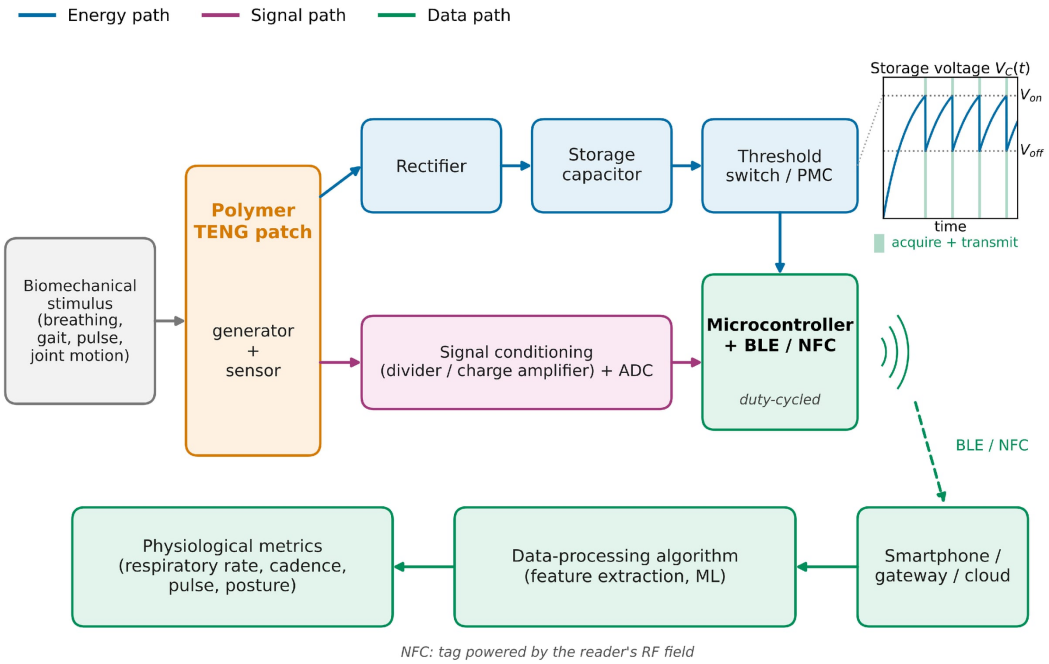


Figure 8. Architecture of a TENG-powered physiological-signal monitoring system. The biomechanical stimulus (breathing, gait, pulse, joint motion) is converted by the polymer TENG patch, which acts as both generator and sensor, along three paths. The energy path (rectifier, storage capacitor, threshold switch or power-management circuit, PMC) intermittently powers the microcontroller and radio module; the signal path, through the conditioning stage (voltage divider or charge amplifier) and the analog-to-digital converter (ADC), delivers the digitized waveforms to the microcontroller; the data path transmits them via BLE or near-field communication (NFC) to a smartphone, gateway or cloud service, where a data-processing algorithm (feature extraction, machine learning) extracts physiological metrics such as respiratory rate, cadence, pulse and posture. Inset: qualitative evolution of the storage voltage $V_C(t)$, which rises to the threshold V_{on} and falls to V_{off} during each acquire-and-transmit window (shaded). For NFC, the tag is powered by the reader's radio-frequency (RF) field; the system is then battery-free but not fully autonomous (Section 1.3). Original elaboration by the authors.

Recent demonstrations include a textile chest strap for respiration monitoring and a heart-rate belt equipped with triboelectric sensors that operate without external bias and whose signals are transmitted wirelessly to a smartphone [111]; woven triboelectric insoles that, after charging a capacitor, intermittently powered low-power electronics, and whose multichannel carpet version discriminated the sequence of activated zones in a simulated

walking test [121]; textile TENGs that act as self-powered pedometers while simultaneously charging an integrated textile supercapacitor [143]; and TENG-micro-supercapacitor systems capable of storing harvested energy to power microsensing systems intermittently, with an operating rate set by the charging interval [144]. Along these lines, an AIoT platform built on a single type of soft, stretchable TENG sensor has enabled machine-learning recognition of user identity and gait from a single insole sensor, of identity and sitting posture from a 12-sensor cushion (98.86% and 98.40% accuracy), and of eight sleep patterns from a 15-channel pillow (96.25%) [21]; the same soft sensor, with a Galinstan liquid-alloy electrode in single-electrode mode, is replicated across insole, cushion, and pillow (Figure S5) [21]; gait-based wearable systems have extended the approach to user identification and to a flatfoot-related gait model in an IRB-approved study, without yet a clinical cohort with a diagnostic reference [145]. Except where harvested energy is explicitly stored and used to power the electronics [121,143,144], in these demonstrations the triboelectric element is self-powered at the transduction level, whereas acquisition, classification, and communication rely on externally powered electronics. A distinct preclinical demonstration concerns the energy-harvesting side rather than sensing: a leadless intracardiac pacemaker powered solely by a heartbeat-driven double-oscillatory TENG, small enough to fit the battery compartment of a commercial leadless device, delivered a volumetric power density of 276.6 $\mu W\ cm^{-3}$ and supported cardiac pacing after implantation in a healthy swine model, with long-term (4-week) implantation evaluated in a single animal [146]. The result demonstrates the feasibility of coupling biomechanical harvesting with a miniaturized therapeutic device, but it does not yet amount to clinical validation.

In order to avoid presenting heterogeneous demonstrations characterized by different levels of maturity, the examples discussed in this section are classified according to the highest level of evidence reported in the cited work (Table 4): (L1) proof-of-concept/benchtop, i.e., characterization on test benches or demonstrations on individual subjects without comparison with a reference method; (L2) pilot study on healthy volunteers, i.e., on small groups of healthy subjects, possibly compared with a reference instrument; (L3) preclinical in vivo study, i.e., acute or chronic studies on animal models; (L4) clinical validation, i.e., prospective studies on the target patient population, conducted by comparison with a clinical reference; (L5) standard-compliant validation, i.e., protocols that meet recognized standards regarding sample size, population distribution, and acceptance criteria (e.g., [129–131] for blood pressure measurement devices). The levels are not strictly sequential: implantable devices usually follow a path from L1 to L3, while wearable devices generally go from L1 to L2, without an animal model phase.

6.4. Biocompatibility, Comfort, and Long-Term Wearability

For wearable and biomedical integration, elastic modulus, breathability, adhesion, and biocompatibility must be optimized jointly. The appropriate values depend on the anatomical site, thickness, and duration of use; for this reason, ranges of modulus, Moisture vapor transmission rate (MVTR), or adhesion energy should be presented as application-specific design targets, not as universal thresholds.

The most advanced TENGs incorporate bioinspired adhesives (catechol or zwitterionic groups), microporous elastomers for ventilation, and elastic encapsulants resistant to sweat and washing; nanofibrous membranes with asymmetric wettability (Janus) push this trade-off further, combining impermeability and breathability with active thermo-hygrometric regulation and bactericidal activity, while maintaining a stable triboelectric output over more than 10,000 cycles [147]. On this basis, the most recent "second-skin" devices have enabled prolonged use with limited signal degradation and no reported skin irritation in the tested conditions [134,147].

Table 4. Highest level of evidence reported for the biomedical applications discussed in Section 6. L1: proof-of-concept/benchtop or single-subject demonstration; L2: healthy-volunteer pilot, possibly against a reference method; L3: preclinical in vivo; L4: clinical validation in the target population; L5: standard-compliant validation. *n*: number of human subjects or animals reported; MAE: mean absolute error.

Application	Section	Ref.	Highest Level	*n*	Evidence Reported	Missing for Next Level
Woven textile TENG: knee/elbow motion, insole, smart carpet	Section 6.1, Section 6.3	[121]	L1	1	Single wearer; Bluetooth readout of knee/elbow patterns at 45°, 90°, 135°; insole tested by one 50 kg subject; carpet path tracking simulated by hand on a 5-channel mock-up	Volunteer cohort against motion-capture or force-plate reference
Gesture input on textile sleeve	Section 6.1	[124]	L2	12	Rule-based recognition, 95.0% over 1200 trials (91–98% per participant); written informed consent	Comparison with a reference input system; ethics-approved cohort
Pulse wave and cardiovascular indices (PWV, SI, HR, HRV)	Section 6.2.1	[126]	L1	1	Single male subject, at rest and after exercise; indices derived from the waveform	Comparison with a reference method (e.g., tonometry, clinical PWV device)
Cuffless Blood Pressure	Section 6.2.1	[125]	L2	5	6-month follow-up; transfer learning reduces mean arterial pressure error by ~27%, MAE ≈ 3 mmHg	Hypertensive patients; protocols of ISO 81060-2/-3 and IEEE 1708 [129–131]
Respiration rate and spirometry	Section 6.2.2	[133]	L2	7	Against reference spirometer: respiration-rate MAE < 0.2 breaths/min; FEV_1/FVC MAE 2.43%	Patients with respiratory disease
Respiration and sleep-apnea monitoring (smart mask)	Section 6.2.2	[132]	L1–L2 [a]	n.r.	Apnea monitoring reported; no patients with a diagnosis documented	Polysomnography-referenced study in patients
Forearm muscle/tendon activity (TENG)	Section 6.2.3	[135]	L1	1	Distinct waveforms for individual finger motions and for MDS-UPDRS severity levels emulated by a healthy user	Patients with Parkinson's disease; comparison with clinical rating and surface EMG
Biceps brachii activity (hybrid tribo-piezo)	Section 6.2.3	[136]	L2	3	Healthy males; ethics approval; simultaneous wireless surface EMG; Pearson r = 0.893–0.910 between sensor and EMG temporal trends; ≥98% accuracy for task-defined fatigue conditions (3 durations × 3 loads) and 5 arm motions (3-fold cross-validation with data pooled across subjects)	Subject-independent validation; larger cohort; patients with musculoskeletal disorders

Table 4. *Cont.*

Application	Section	Ref.	Highest Level	*n*	Evidence Reported	Missing for Next Level
Implantable ligament/muscle deformation sensing	Section 6.2.3	[137]	L3	6 rabbits	Output varies with flexion angle and frequency; stable after 7 days; milder foreign-body response than stainless steel at 4 weeks; electrometer readout	Calibrated in vivo strain; chronic studies; human studies
Biopotentials (ECG, EMG, EOG) with e-skin electrodes	Section 6.2.4	[138]	L1	1 [b]	SNR 25.1 dB vs. 23.9 dB for commercial Ag/AgCl electrodes	Cohort study; comparison with clinical ECG/EMG systems
Sweat electrolytes with TENG-driven iontophoresis	Section 6.2.5	[141]	L1–L2 [a]	n.r.	On-body sweat extraction and analysis aimed at sedentary users	Reported cohort size; validation of sweat Na^+, K^+ and pH readings against a laboratory reference method
Identity, gait, sitting posture, sleep patterns (AIoT)	Section 6.3	[21]	L2	7 (identity); 2 (activity)	ML accuracy 96–99%; informed consent obtained	Independent populations, clinical endpoint
Gait-based healthcare monitoring	Section 6.3	[145]	L2 [a]	n.r.	IRB-approved study; user identification 99.6%; flatfoot time-ratio model	Clinical cohort with diagnostic reference
Leadless intracardiac pacemaker powered by TENG	Section 6.3	[146]	L3	1 swine (4-week) [c]	Pacing supported by harvested energy in a healthy pig	Diseased-heart models; chronic studies; first-in-human

n.r.: not reported in the sources examined; [a] Level assigned from abstract or full-text excerpts; cohort size not available. [b] The volunteer was the first author; the authors state that no ethical approval was required. [c] Long-term implantation performed in a single animal; other measurements with $n \geq 3$.

6.5. Challenges and Perspectives

Despite progress, the large-scale use of TENG-based wearable sensors remains conditioned by a set of interconnected challenges. The first concerns signal stability, which must be preserved against humidity and temperature variations and mechanical fatigue (cf. Section 5.5) and made robust to environmental noise and body-motion artifacts. Humidity can act as a threshold rather than a gradual drift: in a textile TENG, a three-sample humidity sweep showed outputs within 92.7–104.5% of the 20% RH value up to 60% RH, but only 19.9% at 70% RH [124]. Alongside this is the difficulty of integrating energy storage, circuits, and wireless communication into ultrathin and conformable formats without sacrificing comfort and performance. Finally, the issue of standardizing calibration protocols and biocompatibility tests remains open, as does the development of sustainable materials for single-use medical applications. A translational challenge is also added: the transition from prototype to clinical practice requires addressing long-term skin compliance, sweat tolerance, minimally invasive implantation strategies, and the regulatory requirements for clinical validation of TENG-based bioelectronic devices [134].

Signal interpretation by machine learning [21,145] is promising, but its relevance will depend on long-term validation and on demonstrating an advantage over existing clinical technologies; the cross-cutting issues of reliability, metrology, and sustainability are addressed in Sections 8–10.

7. Polymeric TENGs for Environmental and Analytical Sensing

TENGs have demonstrated a versatility that extends well beyond wearable and mechanical sensing, reaching environmental and analytical monitoring of natural phenomena such as wind, rain, droplet impact, fluid flow, and particulate motion. In these systems, the triboelectric signal arises from the interaction between polymer interfaces and dynamic environmental stimuli, enabling monitoring that is self-powered at the transduction stage (Section 1.3), without biasing the transducer; the distinctive element compared with previous sections is the frequent presence of liquid–solid interfaces, in which contact electrification, electric double-layer dynamics, and electrokinetic effects can contribute with different weights to the signal. These mechanisms are not equivalent and require appropriate experimental attribution. The maturation of this platform is now documented by dedicated reviews on nanostructured polymeric TENGs for environmental sensing, which identify control of morphology and surface chemistry as the main performance lever [148]; a review of fluid-based TENGs, in which liquids and gases act directly as triboelectric layers, identifies standardized measurement of the triboelectric series of liquids and gases as a priority for the field [38]. In parallel, the coupling of TENGs with electrochemical and microfluidic transducers has opened the way to environmental and biochemical analysis with reduced dependence on external power [149].

7.1. Sensing of Wind, Raindrops, and Environmental Motion

Environmental TENGs exploit wind, rain, and wave motion as excitation sources. The electrical output varies with impact energy, flow velocity, and contact dynamics, but the functional relationship is architecture-specific and requires calibration for quantitative use. Unlike conventional anemometers or pressure transducers, polymeric TENGs require no bias for transduction, and their output can serve both as a signal and as harvested energy [148] with the trade-offs discussed in Section 4.1.

7.1.1. Wind and Airflow Sensors

Fluttering or flag-type TENGs convert wind-induced vibrations into alternating current through continuous contact–separation cycles of lightweight films (e.g., PTFE, FEP, Kapton).

In many architectures, the output has a calibratable range with respect to flow velocity, but linearity, startup threshold, and operating range depend on geometry and aeroelastic dynamics. Cup-type rotary architectures in particular offer calibratable responses: a wind-driven rotary TENG showed a current sensitivity of 0.526 $\mu A \cdot m^{-1}$ s over a range of 2.2–19.6 m s^{-1}, with a linear correlation between output and speed ($R^2 \approx 0.995$ with a stator-rotor air gap of 18 mm) and, thanks to the thermal response of a shape-memory alloy, the additional ability to non-invasively monitor the airflow temperature of industrial equipment [150]. In this device (Figure 9), rabbit-fur sectors supported by NiTi strips slide against an FEP stator equipped with copper electrodes in a specific configuration; above the alloy's transition temperature (≈40 °C), the sectors flatten, the contact area increases, and the output voltage increases by a factor of about 2.4, thereby translating the air-flow temperature into a triboelectric signal [150]. Fluttering thin-film TENGs have also been adapted to building rooftops, where a wind-driven device powered outdoor temperature–humidity sensing [151], and to unmanned aerial vehicles, where a thin-film TENG coupled with a wind vane measured wind speed over 2.6–30 m s^{-1} through a dedicated signal-processing module [152]; in both cases, compactness and bias-free transduction are the main advantages over conventional solutions.

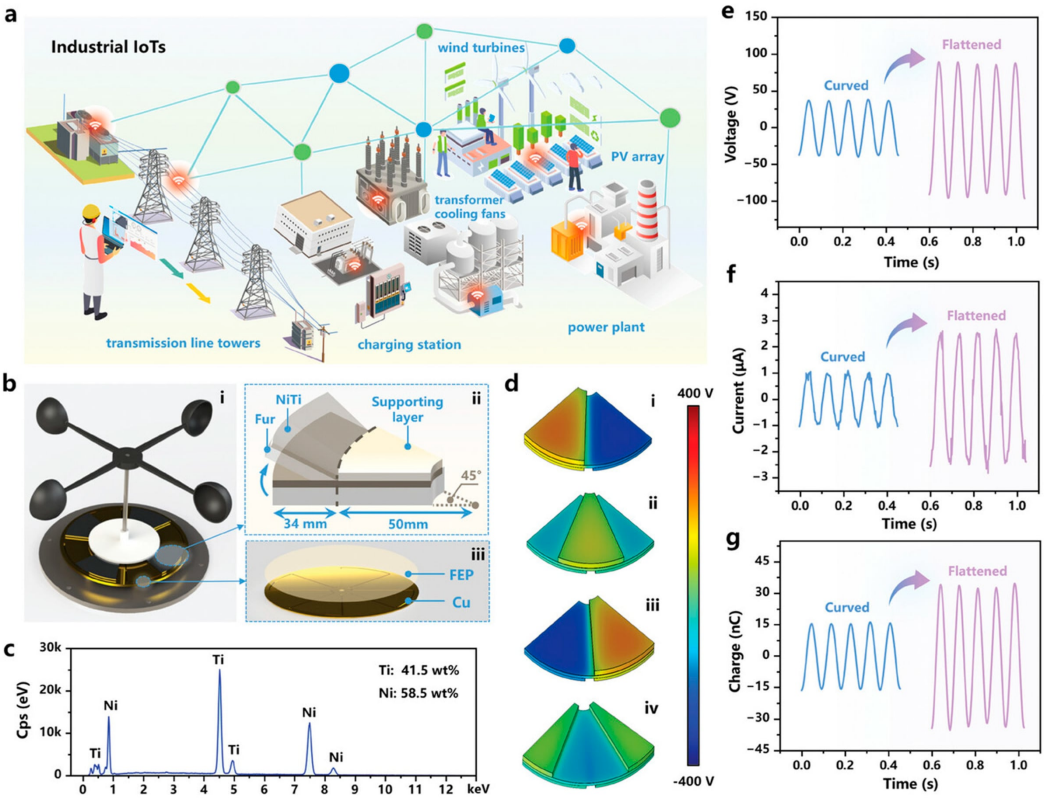


Figure 9. Wind-driven rotary TENG with contact area tuned by a NiTi shape-memory alloy: (**a**) industrial IoT monitoring concept; (**b**) device structure, with the rotator contact area modulated by the thermal response of the alloy, (i) overall 3D schematic of the anemometer-coupled rotary TENG; (ii) enlarged view of a single rotor blade showing the fur layer, flexible NiTi sheet (34 mm, inclined at 45°), and supporting layer (50 mm); (iii) enlarged view of the stator showing the fluorinated ethylene propylene (FEP) dielectric film mounted on segmented copper (Cu) electrodes.; (**e**–**g**) open-circuit voltage, short-circuit current, and transferred charge with the alloy in the curved and straight states. Panel **c**(**c**,**d**) report the Energy dispersive spectroscopy (EDS) spectrum of the alloy and the simulated potential distribution. d Finite element simulation of the open-circuit electric potential distribution (−400 V to 400 V) across two adjacent stator sectors at four consecutive rotational states during a working cycle: (i) initial aligned position showing maximum opposite surface potentials; (ii) intermediate

transition state as the rotor blade sweeps across the electrode gap, reducing the potential difference; (iii) half-cycle position over the adjacent sector, resulting in inverted potential polarity; (iv) return transition state approaching electrostatic equilibrium before completing the cycle.. Reproduced from Li et al. [150], Adv. Sci. 2024, 11, 2307382, Figure 1; © 2024 The Authors, published by Wiley-VCH GmbH, licensed under CC BY.

7.1.2. Raindrop and Precipitation Sensors

TENG-based rain sensors exploit charge transfer induced by the impact between falling droplets and hydrophobic polymer surfaces (cf. Section 2.1). Each droplet generates a transient pulse whose amplitude increases with the impact energy and with the droplet's expansion velocity: the charge transferred per droplet increases as the Weber number increases [153], and the output scales with the rate of change of the contact area, dS/dt, which a low-adhesion surface enhances [154]. A closely related class is that of droplet-based electricity generators (DEGs), in which a top electrode placed on a charged fluoropolymer film is bridged by the spreading droplet, turning the conventional interfacial effect into a bulk effect: in the original PTFE/Indium tin oxide (ITO)–aluminum device, a single 100 µL droplet delivered about 143.5 V and 270 µA, with an instantaneous peak power density of 50.1 W m^{-2}, three orders of magnitude above an otherwise identical device without the top electrode [153]. Since their mechanism and electrical topology do not coincide with those of classical TENGs, DEGs should be presented as an architectural variant. Biomimetic strategies that replicate, by soft lithography, the hydrophobic micro-texturing of leaves simultaneously enable fog harvesting and operation as a self-powered rain sensor [155].

7.1.3. Ocean Wave and Vibration Sensors

On larger scales, floating polymeric TENGs convert surface oscillations into alternating-current output, both for energy harvesting and for wave-motion monitoring. Since transduction occurs by liquid–solid contact, the active layer is typically a strongly tribo-negative fluorinated film (PTFE, FEP), encapsulated in waterproof elastomeric matrices (e.g., PDMS) that ensure its survival in the marine environment; PDMS thus acts as an encapsulant and not as a triboelectric counterpart, since it is also tribo-negative (cf. Section 3.1). A dual-mode TENG with a voltage-multiplying circuit demonstrated, alongside a peak power of 34.3 mW for blue energy harvesting, real-time reconstruction of wave height, with the sensing signal generated by the TENG itself [156]. This suggests that, with appropriate power management, the same device could supply low-power buoy electronics while monitoring wave motion; since 34.3 mW is a peak value, the average power available for continuous operation is lower (Section 4.1).

7.2. Flow- and Droplet-Based Sensing

The triboelectric effect can also be triggered by liquid–solid interactions on polymer surfaces, enabling self-powered sensing of flow, droplets, and particle transport [148].

7.2.1. Fluid Flow Sensing

When a liquid flows over a polymer surface, the signal may include contributions from liquid–solid electrification and from electrokinetic phenomena associated with the electric double layer, including streaming current and streaming potential. Since these contributions have different physical origins, their attribution requires specific experimental controls and specific calibration [148]. In optimized configurations, the relationship between electrical output and flow rate is markedly linear, making such sensors suitable for microfluidics, environmental monitoring, and process control [148]. Liquid–solid interfaces in hydrogels can generate electricity even in the absence of externally imposed flows or contact–separation cycles: in a system consisting of a stretchable gelatin hydrogel and a porous Al_2O_3 membrane,

the natural evaporation of water was sufficient to sustain a direct current of 32 µA, with an open-circuit voltage of 0.4 V and a maximum power density of 0.55 mW m^{-2} [157]. Such evaporation-based (hydrovoltaic) outputs represent a further possible contribution to the signal in liquid–solid devices and reinforce the need, already foreseen in module M5, to adopt controls that make it possible to distinguish contact electrification from electrokinetic contributions (Section 9.4). High-voltage triboelectricity can also be harnessed in reverse to drive the flow: TENG-driven soft electrohydrodynamic pumps have reached pressures up to 4.49 kPa and demonstrated pumping of dielectric liquids without an external electrical supply [158].

7.2.2. Droplet and Aerosol Sensing

The same impact mechanism described in Section 7.1.2 for rain lends itself, in a single-droplet regime and at a smaller dimensional scale, to a different use: no longer estimation of precipitation intensity, but discrete counting of events. Each impact produces a quantized voltage peak, enabling droplet counting and aerosol detection in fog and sprays, and potentially in biomedical settings such as the analysis of exhaled aerosols. Surface adhesion represents a further lever: the incorporation of carnauba wax into PDMS generates surface microstructures that reduce contact angle hysteresis, accelerate droplet spreading and retraction, and increase the peak power density from 0.07 to 1.2 W m^{-2}; because residual water no longer screens the surface charge, the same device is able to sense the droplet's properties, showing a temperature response of 1.57% $°C^{-1}$, a monotonic response to pH in the range 3–6, and a logarithmic response to Co^{2+} ion concentration [154], while liquid–liquid TENGs, in which two liquids act as the triboelectric pair, extend the approach to entirely liquid interfaces: a droplet passing through a suspended liquid membrane generates electricity, and the membrane itself is capable of measuring the charge carried by objects passing through it [159]; an immiscible biphasic aqueous interface transfers up to 129 nC per droplet, in the absence of oil phases [160]; and a liquid–liquid TENG has been operated as a self-powered rainfall sensor [161]. Atomization extends the approach to the analysis of the liquid itself: in a bio-inspired nebulization device, a high-speed air flow fragments the liquid into microdroplets that come into close contact with the solid surface and then rapidly separate from it; this increases the triboelectric output from about 10 V to nearly 1 kV. A hybrid model based on convolutional neural networks (CNNs) and LSTM networks was able to identify the liquids from the resulting waveforms with an accuracy of 99.30%, also enabling the detection of ionic solutes down to concentrations of 10^{-5} mol L^{-1} [40]. As with other recognition-based demonstrations, classification accuracy does not constitute a calibration metric: for quantitative use, the calibration levels, replicates, and selectivity tests specified by the MIS-TENG module for chemical and analytical sensing (A2, Section 9.4) are required. More generally, integrating the transduction function with the material's sensing function has led to self-powered gas and vapor sensors operating at room temperature, in which variation of the triboelectric output directly encodes the analyte concentration [71], including humidity, for which output decreased from 410 to 176 V between 40 and 80% RH in a biowaste-based device [162].

7.2.3. Particulate Matter and Dust Sensing

Charged particles striking polymeric TENG surfaces induce triboelectric charge, generating signals proportional to the flow and kinetic energy of the particles themselves. Flexible PVDF or PTFE films can thus operate as self-powered elements for monitoring airborne particulate matter (e.g., $PM_{2.5}$) or industrial aerosols, without the need for electrical bias of the transducer; quantification of particulate matter nevertheless requires calibration procedures and control of environmental conditions. It should however be observed that

quantitative particulate sensing by TENGs remains an emerging field, for example because for PVDF films impact-induced piezoelectric signals must be distinguished from triboelectric charging, requiring dedicated calibration; moreover, many implementations exploit triboelectric charge mainly for the capture and electrostatic removal of dust rather than for its quantification [148]. Recent work on dilute gas–solid flows illustrates both potential and difficulty: guiding particles toward the sensing wall by swirling flow increased the short-circuit current about twentyfold, under controlled temperature and humidity [163].

7.3. Analytical and Chemical Sensing: Coupling Triboelectric and Electrochemical Transduction

An emerging direction combines TENGs with electrochemical, optical, and chemical sensors, giving rise to hybrid platforms in which triboelectric energy drives or modulates the analytical process, or itself provides the analytical signal. This paradigm, termed self-powered electrochemical sensing in [149], has been reviewed with emphasis on its potential to reduce external power demand for sensing and on its still-open limitations in stability and sensitivity.

7.3.1. TENG-Driven Electrochemical Systems

Polymeric TENGs can provide high-voltage electrical excitation, or a limited amount of harvested energy, to power certain electrochemical processes, provided there is adequate load matching and proper power management. Since their output signal is intrinsically impulsive, characterized by high impedance and low current and charge values per cycle, the fundamental reference parameters are not only voltage, but also the current or energy actually available, the impedance matching between source and load, the duty cycle, and the degree of potential control. On this basis, three complementary modes are outlined. In the first, triboelectric energy powers or modulates an electrochemical transducer; in the second, after rectification and power management, it powers the electronics required for measurement; in the third, it generates electrical pulses for microfluidic actuation or signal modulation. In general, the TENG does not directly replace a potentiostat when a controlled potential and quantitative current measurement are required: the electrochemical function remains entrusted to the circuit and the sensitive interface. A significant example is offered by multifunctional PCL/PPy/GO nanofibers functionalized with glucose oxidase (GOx), used as a tribo-positive layer against tribo-negative electrospun PVDF nanofibers: the nanofiber-only device generates peak voltages of the order of 60 V and the open circuit voltage decreases with the glucose concentration (from around 62 V with the enzyme alone to around 50 and 40 V with 5 and 10 mM), an effect that the authors attribute to the reduction of the positive charge density of the enzymatic layer by the oxidation products [164]. The same type of nanofiber, transferred onto screen-printed electrodes, also acts as a voltammetric transducer for glucose, read with an external potentiostat, so that electrochemical and triboelectric sensing share a single material while remaining distinct measurements [164]. The full electrical response is shown in Figure S6 [164]. The PVDF–PCL/PPy/GO pair illustrates the requirement, consistent with the triboelectric series (see Section 3.1), to couple the tribo-negative fluoropolymer layer to a counterpart of opposite polarity and not to other tribo-negative materials; however, it should be noted that the triboelectric response to glucose is documented on only three concentration levels, insufficient to define a calibration curve in the metrological sense of Section 9.

7.3.2. TENG–Microfluidics Coupling

In microfluidic systems, the triboelectric signal generated by the sample itself can be used for non-invasive monitoring: a liquid–solid TENG device, integrated into a droplet microfluidic chip, detects the frequency, length, and velocity of the droplets from the

voltage pulses produced by their passage [165]. Conversely, a TENG can act as a high-voltage source for on-chip actuation, as in a TENG-powered dielectrophoretic platform in which a rotating TENG and a rectifier/filter circuit generate the non-uniform field that manipulates microparticles in a microchannel [166]. The triboelectric–electrohydrodynamic pump mentioned in Section 7.2.1 belongs to a different category and scale: in that case, the TENG acts as a high-voltage source that injects charge into a dielectric liquid (ion-drag mechanism), rather than exploiting wall tribo-ionic effects; moreover, the resulting flow rates, up to hundreds of mL min^{-1}, are typical of macroscopic pumping rather than lab-on-chip operation [158].

7.3.3. Optical and Chemical Coupling

Triboelectric outputs can also directly drive optoelectronic components, as in the case of lighting hundreds of commercial LEDs through the impact of just a few droplets [153]. Polymeric TENGs that incorporate mechanoluminescent phosphors, typically ZnS:Cu dispersed in PDMS or Ecoflex, emit light upon impact or deformation while simultaneously generating a triboelectric signal, thus integrating optical and electrical sensing in a single device [167,168]; the emission itself has been attributed to triboelectrification at the phosphor–polymer interface, whose intensity increases with the distance between the two phases in the triboelectric series [169].

7.4. Robustness and Environmental Stability

Environmental sensors must withstand thermal excursions, UV radiation, humidity, and mechanical abrasion. Polymers such as PTFE, FEP, and PVDF offer exceptional chemical stability and hydrophobicity, preserving triboelectric performance in harsh outdoor environments, while encapsulation with fluorosilane or parylene coatings mitigates moisture adsorption and charge loss (cf. Section 3.6). Self-cleaning and anti-adhesive micro-textures, inspired by the morphologies of lotus leaves or cicada wings, reduce dust accumulation and preserve optical transparency; the same biomimetic hydrophobic surfaces, in addition to ensuring stability for months outdoors, can perform an active function of fog harvesting and rain sensing [155].

7.5. Overview of Applications and Performance

A concise comparison of the main configurations of polymeric TENGs for environmental and analytical sensing is reported in Table 5; material pairs are indicated as liquid–solid systems or as oppositely polarized pairs where relevant, and the reported metrics are not intended for direct comparison.

These examples show how polymeric TENGs connect energy harvesting, environmental sensing, and analytical functionality, outlining a path toward autonomous platforms for environmental monitoring and portable analytical devices, although in most current demonstrations self-powering is limited to the transduction stage [148,149].

A critical analysis of Table 5 reveals that TENGs intended for environmental and analytical applications are at a less advanced stage of development than those used as mechanical sensors: fewer than half of the cases report a calibration slope over a defined range, several parameters remain qualitative in nature, and the glucose response is based on only three concentration levels. In liquid–solid devices, the attribution of the signal to contact electrification or to electrokinetic effects is rarely verified through specific controls (Section 7.2.1), and cross-sensitivity to temperature and humidity is almost never quantified. These gaps define the content of modules M5 and A2–A3 of MIS-TENG (Section 9.4).

Table 5. Representative configurations of polymeric TENGs for sensing and actuation platforms: application, device architecture, material system (solid–solid pairs with opposite polarization or liquid–solid systems), signal type, main reference parameter and performance. The entries report the parameters indicated in the respective sources and are not comparable across different rows. They refer to different measured quantities and output quantities (current, voltage, charge per drop, pressure, flow rate), to different normalizations (for example, instantaneous peak values versus cycle-averaged values) and to non-homogeneous test conditions; moreover, some data remain qualitative in nature. A critical analysis is presented below.

Application	Configuration	Material System	Signal Type	Key Metric	Performance	Ref.
Wind speed sensor	TENG rotary cup-type (soft contact)	FEP–rabbit fur on NiTi alloy	I_{SC} and frequency $\propto$ speed	2.2–19.6 m s^{-1}	0.526 $\mu A \cdot m^{-1}$ s; $R^2 \approx 0.995$	[150]
Droplet energy (tap, rain, sea water)	DEG: PTFE/ITO with Al top electrode	PTFE–water	Voltage/charge pulse per droplet	Q per droplet vs. We: 13.3–53.3 nC (We 7.7–150.4)	143.5 V; 270 µA; 50.1 W m^{-2}	[153]
Water-quality sensing	DEG with low-adhesion surface	PDMS + 1 wt% carnauba wax–water	Pulse amplitude vs. droplet property	Temperature 25–70 °C; pH 3–6; Co^{2+} 5–100 µM	1.57% $°C^{-1}$; 9.6 V $\ln(\mu M)^{-1}$	[154]
Wave sensor	Floating TENG	Fluorinated film encapsulated in PDMS	$V_{OC} \propto$ wave height	Low frequencies	Height monitoring	[156]
Flow-rate sensor	Liquid–solid channel	PTFE–water/PDMS	$V_{OC} \propto$ flow rate	Device-dependent	Linear correlation	[148]
Dust/particle monitor	Sheet TENG	PVDF or PTFE (single film)	Impact voltage	$PM_{2.5}$ flow	Emerging	[148]
Electrochemical transducer	TENG + enzymatic electrode	PVDF–PCL/PPy/GO (+GOx)	V_{OC} decrease with glucose	Glucose (mM)	$V_{OC} \approx 62 \rightarrow 40$ V (0–10 mM; 3 levels)	[164]
Fluid actuation (EHD pumping)	TENG-driven EHD pump	Nylon–PVC (rotary TENG); TPU pump	pressure/flow rate	$\leq$4.49 kPa; $\leq$502 mL min^{-1}	Pumping of dielectric liquids without an external electrical supply	[158]

Rows citing [148] summarize trends reported in that review rather than values measured on a single device.

8. Polymers, Interfaces, and Stability: Degradation, Aging, and Reliability in TENG Sensors

For continuous operation, in wearable, structural, or environmental contexts, reliability and signal consistency are just as fundamental as sensitivity. However, polymeric triboelectric interfaces are intrinsically dynamic: their surface chemistry, morphology, and charge-trapping characteristics evolve under the effect of mechanical, environmental, and electrical stresses.

8.1. Sources of Degradation in Polymeric TENGs

The degradation of polymeric TENGs originates from three families of processes, mechanical wear, chemical and thermal aging, and electric charge decay, which often act synergistically, each modifying the surface energy landscape and, ultimately, the triboelectric charge density (σ).

Mechanical wear and abrasion arise from repeated contact, sliding, and separation sequences, which induce progressive abrasion, microcrack formation, and delamination at polymer–polymer and polymer–electrode interfaces; the resulting reduction in effective contact area and change in surface roughness translate into a steady decline in output voltage (V_{OC}). Soft elastomers, such as PDMS and polyurethane, absorb much of the contact stress through elastic deformation; however, they remain susceptible to permanent deformation and tearing under high loads, and abrasion of the contact surface represents a significant limitation for the durability of solid-solid contact devices [170]. Greater stiffness does not, however, by itself guarantee wear resistance. PTFE, in particular, exhibits a high wear rate and tends to form transfer films on the counterface: in sliding contacts, these can reduce transferred charge, transforming the interface into a PTFE–PTFE contact [26]. Harder polymers such as PVDF better preserve surface morphology, although they remain sensitive to debris accumulation and adhesion forces.

In addition to wear, chemical and thermal aging act on the molecular chemistry of the triboelectric layer: oxidation, hydrolysis, and UV-induced chain scission alter its polarity and electron affinity. PDMS, for example, under short-wavelength UV irradiation in the presence of ozone undergoes surface oxidation and chain scission, forming a fragile, silica-like layer [171], from tens of nanometers to about a micrometer thick, whose mismatch in elasticity with the underlying elastomer makes it prone to cracking [172], whereas in PVDF thermal history, crystallization, and annealing can modify the distribution of crystalline phases and thus the polarization; the direction and extent of the transformation depend on the thermal protocol and formulation.

More generally, as temperature increases, thermionic emission accelerates the dissipation of surface charges and reduces the charge-storage capacity of the triboelectric layer [173,174], while material properties such as bandgap, carrier mobility, crystalline structure, breakdown field, and defect density become less stable [175]. The competition between charge-generation and charge-dissipation factors means that many devices exhibit an optimal operating temperature beyond which output degrades. The ingress of humidity and ambient oxygen accelerates these processes, simultaneously altering dielectric properties and mechanical compliance.

The third pathway is electric charge decay: charges trapped at the triboelectric interface gradually dissipate through surface conduction, bulk conduction (injection and drift of charges in the dielectric), dipolar relaxation, and neutralization by atmospheric ions, with kinetics accelerated by high humidity, ionic contamination, and temperature. Characteristic decay times vary widely with material, trap depth, humidity, temperature, and storage conditions, so that no single universal time scale is meaningful; it is precisely charge-trap

engineering that represents the most effective lever to slow decay (cf. Section 3.6), since denser and deeper traps make charges harder to dissipate and stabilize their retention [68].

Gas breakdown, which limits charge density (Section 2.1), can also contribute to failure; high-capacitance dielectrics combined with trap engineering mitigate both breakdown and bulk dissipation [68].

8.2. Interfacial Degradation and Electrode Delamination

The polymer–electrode interface constitutes a critical bottleneck for reliability. Elastic modulus mismatch and mechanical fatigue between the conductive layer (ITO, AgNW, Au) and the polymeric substrate trigger crack nucleation, delamination, and loss of electrical continuity, a degradation that repeated bending and stretching accelerate in wearable devices. Mitigation strategies converge on several complementary directions, which act on different levels but cooperate in preserving electrical continuity. A first approach aims to make the electrode intrinsically conformal, so that it follows substrate deformation without fracturing: this includes silver nanowire networks, liquid metals such as the gallium–indium eutectic (eGaIn), and PEDOT:PSS films with added elastic crosslinkers; the incorporation of liquid metal into silicone matrices, in particular, makes it possible to combine conductivity, high stretchability, and interfacial self-healing capability [120]. When the problem is instead bond strength, adhesion promoters are used, from surface silanization to plasma activation, which strengthen polymer–metal anchoring. Where mismatch between adjacent layers dominates, the insertion of gradient interlayers, such as MXene–PU transitions, mitigates both the mechanical and electronic imbalance. Finally, thin elastomeric encapsulation layers distribute stress and hinder interfacial oxidation, closing the environmental front of the problem (cf. Section 3.6) [176].

8.3. Charge Retention and Environmental Effects

Maintaining a stable surface charge density (σ) under real environmental conditions remains one of the most persistent challenges for polymeric TENGs. Charge loss originates from several concomitant phenomena: adsorbed water layers, which act as ionic conductors and locally short-circuit the charge; airborne ions and contaminants, which neutralize surface traps; and temperature-driven dipolar relaxation, which reduces local polarization. Hydrophobic passivation and charge-trapping or ion-impregnated interlayers (Section 3.6) mitigate these losses; the latter retain charge even after cuts, punctures, or crumpling [70]. Temperature acts in parallel by altering permittivity and viscoelastic response, and therefore both σ and V_{OC}; encapsulation, hydrophobic coatings, and low-vapor-pressure electrolytes mitigate these effects [177–179].

Humidity dependence is particularly pronounced: in unprotected devices, water adsorption increases surface conductivity and accelerates charge dissipation, so that, when relative humidity rises from 15 to 95%, the short-circuit current of a nylon-11-based TENG drops about sevenfold, from 9.1 to 1.3 μA, and its maximum output power from 2.6 to 0.054 mW [180], evidence that underscores the importance of environmental control and encapsulation for reproducible triboelectric output [177]. Among solutions that address the problem at its source, charge dispersion in the dielectric volume (for example, distributing charges not only on the surface but also within a thermoplastic polyurethane matrix loaded with carbon nanotubes) allows the device to operate stably in high-humidity environments and even in rain, whereas conventional TENGs suffer from charge leakage [181]. The overall picture of currently available strategies for preserving triboelectric output in humid environments is summarized in Figure 10 [177]: encapsulation, hydrophobic or superhydrophobic functionalization of surfaces, fibrous architectures, hygroscopic materials, and charge excitation.

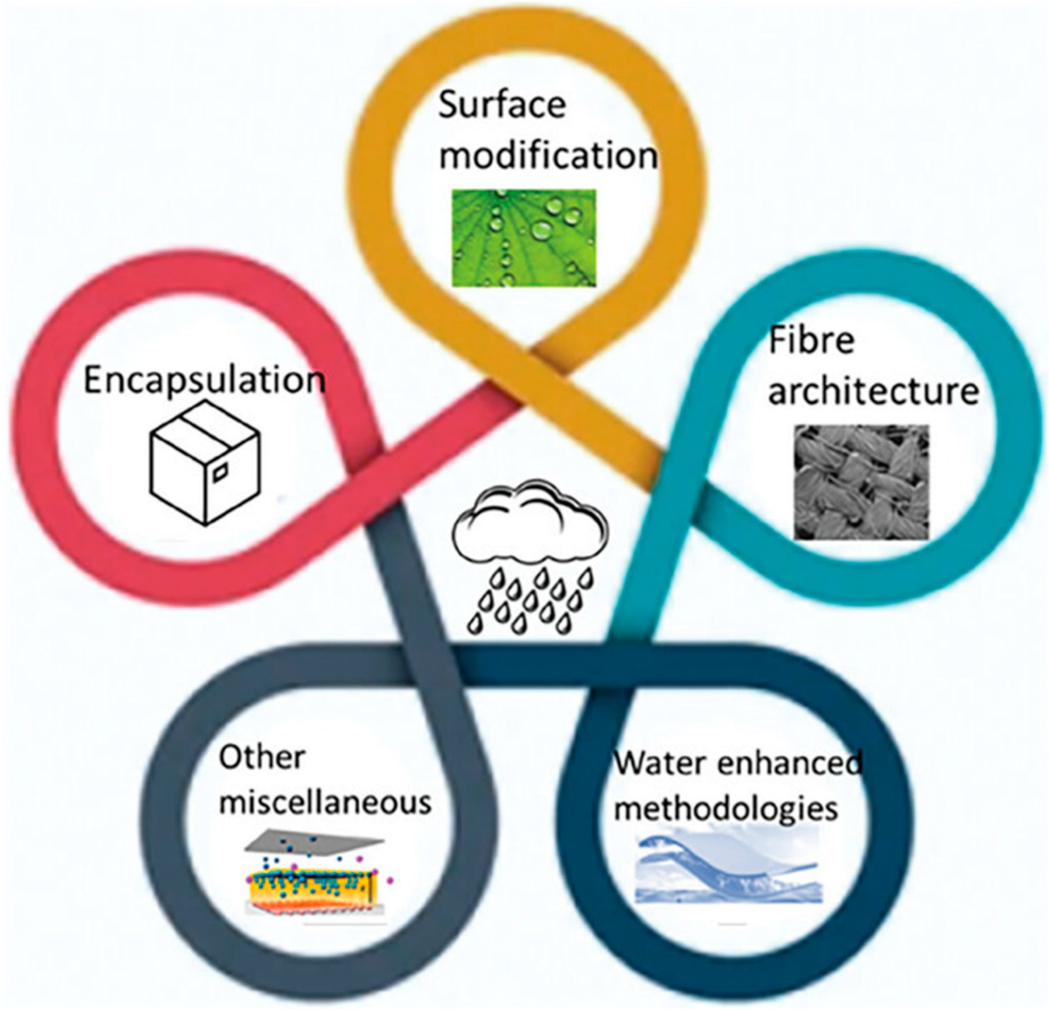


Figure 10. Strategies to increase the humidity resistance of TENGs: encapsulation; hydrophobic or superhydrophobic surface modification; superhydrophobic or moisture-gradient fibrous architectures; hygroscopic materials in which water participates in triboelectrification; and charge accumulation or excitation. Reproduced from Zhang et al. [177], Small 2024, 20, 2401846, Figure 1; © 2024 The Authors, published by Wiley-VCH GmbH, licensed under CC BY.

8.4. Self-Healing Materials and Damage-Tolerant Architectures

The development of self-healing polymers opens a promising route to restoring performance after mechanical or electrical damage. Dynamic networks, covalent (disulfide, imine, boronic ester bonds) or supramolecular (hydrogen bonds, metal coordination), allow spontaneous repair of microcracks and reformation of interfacial adhesion after damage, and recent results show how advanced this repertoire has now become. Poly(urethane-urea) elastomers containing aromatic disulfides activated by amino groups, which combine S–S bond exchange and hydrogen bonds in a dual-dynamic network, achieve self-healing efficiency up to 96% at room temperature, without heating or catalysts, while preserving high mechanical robustness [182]. Similarly, polyurethanes in which hydrogen bonds and disulfide bridges coexist restore more than 95% of the electrical output to a TENG that has been cut and re-sealed [183]. On the supramolecular side, the incorporation of liquid metal into PDMS through interfacial assembly via weak interactions produces triboelectric materials with extraordinary stretchability (up to 12,000%) and rapid self-healing, on the order of half an hour at room temperature, operational even under extreme conditions (−20 °C, under near-infrared irradiation, or immersion) [120]. Supramolecular networks that combine hydrogen bonds and metal coordination, finally, combine high strength and toughness

with full recovery of electrical output after cutting and stability over 10^4 contact–separation cycles [184]. Overall, these materials extend operational life and enable sustainable and reconfigurable sensing systems [185].

8.5. Encapsulation, Sealing, and Environmental Durability

To ensure operation in harsh or variable environments, in the presence of humidity, UV radiation, or thermal cycles, increasingly sophisticated encapsulation strategies have been developed. Multilayer coatings that alternate elastomers and fluoropolymers combine flexibility and barrier properties; parylene-C films, conformally deposited from the vapor phase with thicknesses typically on the order of microns, constitute an effective moisture barrier; if applied on the contact surface, however, they become the triboelectric layer and modify its polarity; lotus-leaf-inspired superhydrophobic coatings keep contact interfaces dry under rain or sweat (cf. Section 7.4); and UV-stabilized formulations incorporating hindered amine light stabilizers (HALS) and UV absorbers suppress photodegradation. Accelerated hot–humid and mechanical cycling tests are used to evaluate encapsulation effectiveness; conditions such as 85 °C/85% RH, borrowed from electronics reliability standards (e.g., JEDEC JESD22-A101 [186]), or more than 10^6 cycles have been adopted in specific studies, but they do not yet constitute a universally standardized TENG protocol [26].

8.6. Quantification of Reliability and Aging

Standardized metrics for describing the stability of a TENG are gradually emerging. Among the proposed quantities, the output retention ratio ($R(t)$), defined as $R(t) = (V_t/V_0) \times 100\%$, where V_t is the output after t cycles or hours and V_0 is the initial output, measures how much performance is preserved over time, while fatigue life ($N_{10\%}$) translates the same concept into mechanical terms, indicating the number of cycles that leads to a 10% drop in output (Table 1). To synthesize combined exposure to humidity, temperature, and UV, a composite environmental durability index (EDI) could be introduced as a reporting metric; however, it should be regarded as a methodological proposal and not an established standard.

On the diagnostic side, advanced characterization techniques such as atomic force microscopy (AFM), the Kelvin probe, and X-ray photoelectron spectroscopy (XPS) make it possible to track over time the morphological and electronic evolution of triboelectric surfaces; in particular, methods based on isothermal surface potential decay allow the depth and density of charge traps to be inferred, correlating them with retention [68]. Looking ahead, the integration of machine-learning algorithms with TENG output, for example for adaptive correction of signal drift so as to compensate for progressive material degradation, offers diagnostic tools to support condition monitoring of devices in operation [117].

8.7. Toward Standardized Reliability Testing

Despite this progress, the scientific community still lacks unified protocols for reliability testing of triboelectric devices, a gap that hinders reproducibility and inter-laboratory comparison. A reliability module of MIS-TENG (Section 9.4), referred to as MIS-TENG-R, is therefore proposed here to harmonize the reporting of durability tests, building on recently proposed test protocols [26]. Figure 11, taken from the testing guide by Mulvihill et al. [26], groups into four categories (fabrication, mechanical, electrical, and environmental factors) the variables that, if not controlled and reported, make results non-comparable across laboratories. It is on this set that the reporting requirements listed below are built. This module recommends that each durability study report the environmental test conditions (temperature, relative humidity, atmosphere); specify amplitude, frequency, and total number of cycles of the applied mechanical load; state the acceptance criterion adopted for

output retention, which depends on the application (e.g., ±5% over a given number of cycles, or N_{10}%); document the observed failure modes, distinguishing their mechanical, electrical, or chemical nature; and report the number of devices tested, with $n \geq 3$ independent devices recommended. Adoption of these practices would make reproducibility, inter-laboratory benchmarking, and accelerated reliability optimization possible.

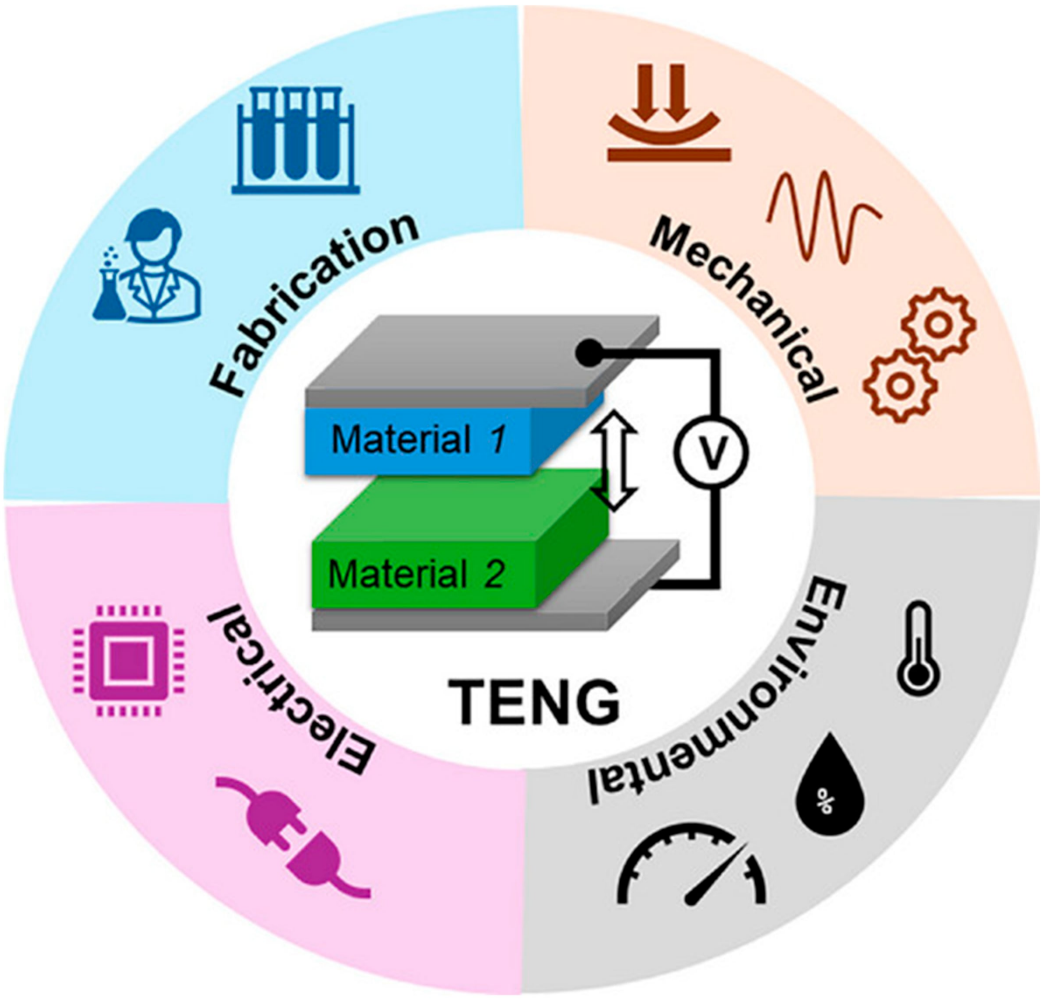


Figure 11. Factors affecting the outcome of TENG tests, grouped into fabrication, mechanical, electrical, and environmental categories (e.g., nominal contact pressure, alignment, surface roughness, instrument impedance, temperature, and relative humidity); failing to control or report any of them makes results non-comparable across laboratories [26]. The same variables define the boundary conditions required by MIS-TENG-R. Reproduced from Mulvihill et al. [26], Adv. Energy Mater. 2025, 15, e02920, Figure 1; © 2025 The Authors, published by Wiley-VCH GmbH, licensed under CC BY.

8.8. Sustainable Durability: From Protection to Regeneration

Reliability must not be maximized independently of end-of-life: extremely durable but irreversibly persistent materials can transfer the problem from performance to sustainability. Dynamic networks, self-healing materials, and reprocessable matrices offer a bridge between in-service durability and end-of-life recovery [187–189].

9. Metrology and Standardization in Self-Powered TENG-Based Sensors

The rapid expansion of TENGs has produced a vast but fragmented corpus of performance metrics, often reported under non-homogeneous test conditions. Unlike conventional sensors, for which calibration procedures are well established, TENGs yield outputs strongly

dependent on input mechanical parameters, environmental conditions, and circuit configuration. Consequently, cross-comparisons are often unreliable, with negative repercussions on both scientific reproducibility and technological transfer. Consolidated benchmarks exist at the generator and material levels [22,23,30], and standardized test protocols, up to a dedicated ISO committee, are now called for [26]; the metrological characterization of TENGs used as sensors, however, still lacks a shared reference framework. The preceding sections identified this gap area by area: the dependence of the transfer function on dielectric thickness and humidity (Section 2.1), the piezoelectric contribution in polar polymers, rarely isolated from the other components (Section 3.2), the poor documentation of readout conditions (Section 4.8), the variation in the nature of the primary metric across different mechanical sensors (Section 5.6), the absence of comparisons with reference methods in biomedical demonstrations (Table 4), the lack of calibration slopes and of controls for signal attribution in liquid–solid devices (Section 7.5), as well as the heterogeneity of protocols for durability assessment (Section 8.7). The framework proposed in this section organizes these recurring gaps into a single reporting structure. Unlike Sections 2–8, which examine already published evidence, this section is predominantly propositional in nature: the proposal presented here constitutes a starting point toward such a reference framework, without intending to replace normative formalization; its relationship with existing figures of merit, standards and test guides is analyzed in Section 9.4.2.

9.1. The Reproducibility Challenge

Triboelectric outputs, open-circuit voltage (V_{OC}), short-circuit current (I_{SC}), and transferred charge (Q_{tr}), are not intrinsic properties of materials but system-dependent responses. They vary with force amplitude (F), frequency (f), and contact area (A); with relative humidity (RH), temperature (T), and the surrounding atmosphere; and with electrical load impedance (R_L) and the measuring equipment used. Because many publications omit reporting these parameters, declared values are ambiguous: the same statement, e.g., "V_{OC} = 500 V," may correspond to profoundly different forces or geometries. The consequences of missing test and reporting protocols are well documented for polymer piezoelectric generators, where contact-electrification charge is frequently mistaken for piezoelectric output [60]; conversely, in TENG sensors, parasitic contributions (piezo- and pyroelectric charge, cable triboelectricity, motion artefacts) must be excluded. For accurate benchmarking, it is therefore indispensable that all TENG metrics be normalized and contextualized within a standard test perimeter [22,26,30]. The same requirement applies to seemingly well-established quantities: in the V–Q plane of a contact-separation-based TENG, electrical discharge in air can already occur at 50 μC m^{-2}, making part of the maximum-energy cycle inaccessible; consequently, the extractable energy depends on the gas, its pressure, and the air-gap geometry, and not only on the materials. The standardized method proposed by Xia et al. experimentally determines the discharge points and accordingly redefines the figures of merit (Figure S7) [30].

9.2. Key Parameters and Normalization Strategies

9.2.1. Electrical Performance Metrics

The definitions of Table 1 (Section 2.4) apply; this section adds the instrumental requirements on which their measurement depends.

Instrumentation must be selected according to the source impedance and signal bandwidth. Input-impedance requirements for voltage- and charge-mode readout are given in Section 4.5; the sampling frequency must be sufficiently greater than the signal bandwidth to correctly reproduce peaks and transients. Sampling rates such as $\geq 10^6$ samples s^{-1} may be appropriate in many configurations, but they do not constitute universal requirements.

Any digital filtering or smoothing applied to the signal must be declared, since it alters peak values.

9.2.2. Mechanical Normalization of Inputs

Because the triboelectric response depends jointly on force or pressure, displacement, velocity/frequency, real contact area, and contact history, these quantities must be reported explicitly; it is generally not possible to reduce different devices and regimes to a single proportionality with the input mechanical work, which for a real contact must be calculated as the integral of force over displacement ($Wm = \int F\,dx$) and reduces to $F \cdot \Delta x$ only at constant force. Normalized metrics such as V_{OC}/F or Q_{tr}/A can facilitate comparisons within families of comparable devices, provided that the operating range, geometry, frequency, and environmental conditions are declared; they alone do not constitute a universal normalization. For cyclic loading, the excitation waveform (sinusoidal or square-wave), the velocity/acceleration profile, the preload, the maximum separation, and the dwell time must also be specified, at frequencies representative of the target application (e.g., 1–10 Hz for human motion). Since the output typically builds up over the initial cycles until the surface charge saturates, the number of pre-conditioning cycles before data acquisition, and any charge-neutralization step between tests, must be reported [26].

9.2.3. Environmental Controls

Temperature and relative humidity must be maintained and reported in a controlled manner; a reference range such as 25 ± 2 °C and 40–60% RH may be adopted when compatible with the application, but it should not be interpreted as a universal standard (cf. Section 8.3); to these factors are added atmospheric pressure and the composition of the gaseous medium, which are also capable of altering triboelectric charge density. For reliable calibration, it is therefore recommended to conduct tests at constant and always reported temperature and humidity, resorting, where greater accuracy is required, to chambers with controlled relative humidity, in inert gas (nitrogen or argon), or under vacuum [26]. Note that low pressure or inert atmospheres raise the breakdown-limited charge density, so values obtained there are not representative of ambient operation and must be labelled as such.

9.3. Toward Reporting Guidelines for TENG-Based Sensors

In order to promote clarity and reproducibility, we propose a minimum set of information to accompany studies on TENG sensors. These cover the materials and the device, the test and environmental conditions, the circuit and the measuring instrument, and the output and durability data needed to interpret a result; the complete list is given in Section 9.4. This set of information forms the basis of the reference framework proposed in this review, named *Minimum Information Set for Triboelectric Sensors* (MIS-TENG). MIS-TENG is a proposed checklist for the documentation of results, not a normative standard: its items reflect the synthesis, carried out by the authors, of the evidence discussed in Sections 2–8 and have not yet been validated through interlaboratory comparisons (a validation roadmap is proposed in Section 11.3). Unlike the general checklist for tests proposed by Mulvihill et al. [26], focused on the characterization of generators, MIS-TENG introduces metrological descriptors specific to sensors (LoD, nonlinearity, hysteresis, drift, response time) and distinguishes between the descriptors required for every device and those that depend on the architecture and application. As discussed by Mulvihill et al. [26] (Figure S8), layer thickness, quality of the electrode–dielectric interface, flatness and parallelism of surfaces, position of conductors, and surface topography affect the real contact area and therefore

the output. For this reason, we recommend characterizing roughness with areal parameters and connecting conductors outside the active area.

9.4. MIS-TENG: A Proposal for a Minimum Information Set for Triboelectric Sensors

The MIS-TENG framework is inspired by minimum information schemes already established in biology, such as MIAME for microarray data [190] and MIAPE for proteomic data [191]. It reorganizes the information described in Section 9.3 into four domains (materials, device, test conditions, and output signals) and two levels of requirements (Figure 12, Table 6). Core descriptors apply to all triboelectric sensors, regardless of their architecture. They identify the device, the applied stimulus, the environmental conditions, and the signal acquisition system, while also providing the performance parameters necessary to interpret the reported results. Module descriptors, by contrast, apply only when the corresponding architecture, interface, or application is present.

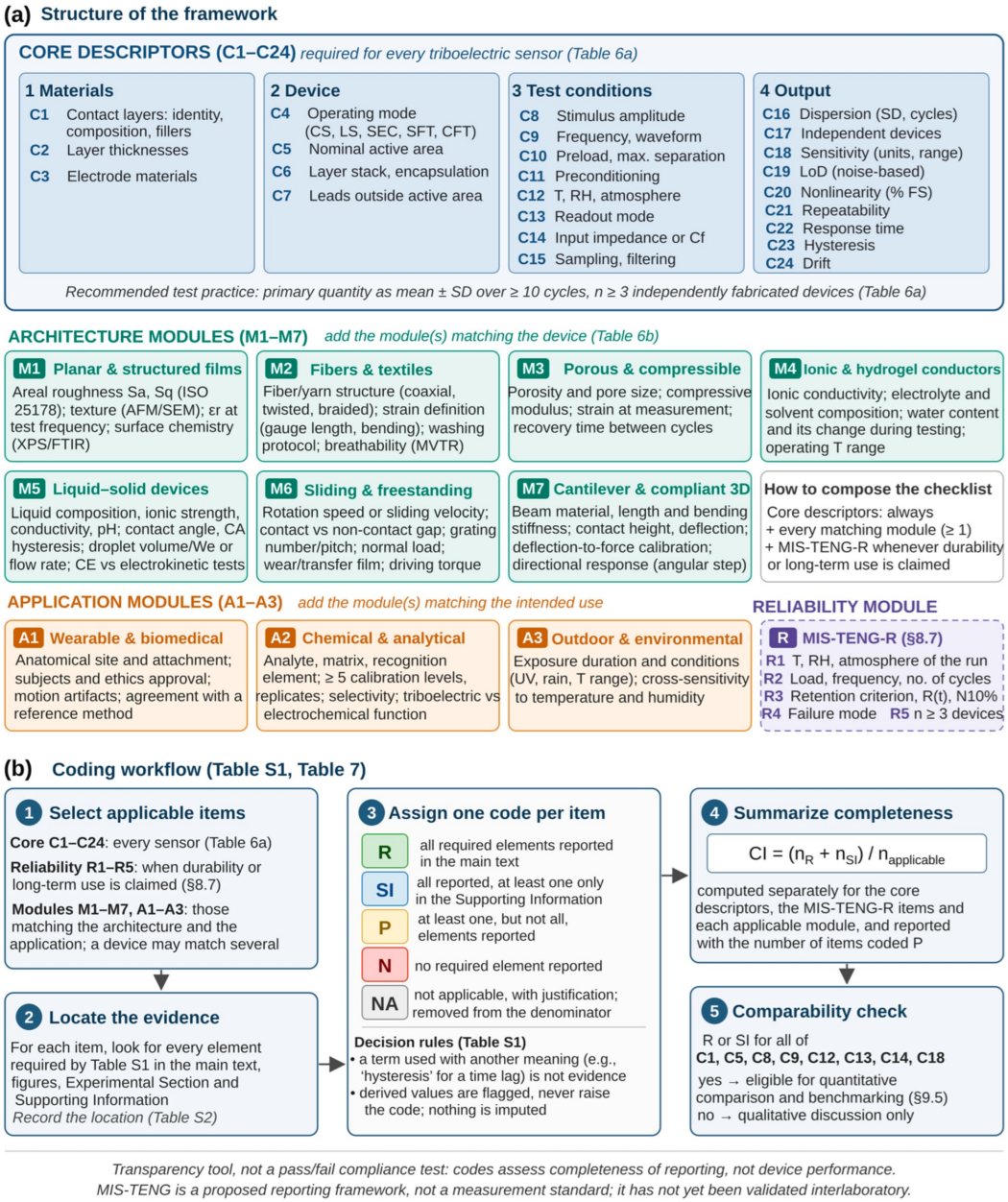


Figure 12. MIS-TENG, the minimum-information framework proposed in this review. (**a**) Structure: information is organized into four domains (materials, device, test conditions, output) and two levels:

core descriptors (C1–C24), to be reported for every triboelectric sensor, and module descriptors, to be added only for the matching architecture (M1–M7) or application (A1–A3) (Table 6); durability claims are documented with the reliability module MIS-TENG-R (R1–R5, Section 8.7). (**b**) Coding workflow: applicable items are selected, the elements required by Table S1 are located in the main text and Supporting Information, and each item is coded R, SI, P, N or NA; completeness is summarized by the completeness index CI, and only devices with R or SI codes for C1, C5, C8, C9, C12, C13, C14 and C18 enter quantitative comparisons (Section 9.5). CS, contact–separation; LS, lateral sliding; SEC, single-electrode contact; SFT, sliding freestanding; CFT, contact freestanding; Cf, feedback capacitance; T, temperature; RH, relative humidity; SD, standard deviation; LoD, limit of detection; FS, full scale; εr, relative permittivity; AFM, atomic force microscopy; SEM, scanning electron microscopy; XPS, X-ray photoelectron spectroscopy; FTIR, Fourier-transform infrared spectroscopy; MVTR, moisture vapor transmission rate; CA, contact angle; We, Weber number; CE, contact electrification; UV, ultraviolet; R(t), output retention; N10%, cycles to 10% output loss. MIS-TENG is a proposed reporting framework, not a measurement standard (Section 9.3). Original elaboration by the authors.

This distinction is important because a descriptor that is decisive for a given class of devices may be of little significance for another. Areal surface roughness, dielectric constant, and surface functional groups influence the real contact area and charge density in planar or microstructured films. However, such parameters are poorly representative of the behavior of a rotary freestanding-electrode device, in which the gap geometry and the pitch of the periodic structure play a predominant role, or of a generator based on a liquid–solid interface. In liquid–solid devices, the composition, ionic strength, conductivity, and pH of the liquid become essential parameters, together with surface wettability (contact angle and contact angle hysteresis), because they influence both charge transfer and the formation and behavior of the electric double layer (Section 7.2).

Every study should therefore report all core descriptors, integrating them with those of the modules relevant to the specific device configuration. Within each applicable module, parameters that were not measured must be explicitly declared as such, rather than simply omitted. The completed checklist constitutes a tool for transparency and traceability of information, not a binding conformity criterion based on a binary (pass/fail) assessment. Completeness is therefore assessed only on what is reported (column 'Items to report (C1–C24)' of Table 6a), whereas the recommended test practice and the application-dependent acceptance criteria serve as guidance for experimental design and evaluation. Each element is coded as: reported in the main text (R), reported only in the Supporting Information (SI), reported partially or ambiguously (P), not reported (N), or not applicable (NA); the operational definitions, units of measurement, calculation methods, and decision criteria for each core descriptor are given in Table S1; the coding workflow is summarized in Figure 12b. An element is coded as P when at least one, but not all, of the elements listed in Table S1 is present, and as N when none is present; a term used with a meaning different from that indicated in Table 1 is not considered as evidence of that descriptor. The NA label requires a justification and entails excluding the element from the denominator. Missing values are never imputed; quantities calculated by the coder (for example, the number of cycles derived from the test duration and frequency) or inferred from figures are flagged as "derived" and do not affect the code. Completeness is expressed through the completeness index CI = (R + SI)/applicable core descriptors, reported together with the number of elements coded as P (cf. Table 7). Authors could include the checklist among the Supporting Information, thereby allowing readers and reviewers to immediately identify which descriptors are available.

Table 6. Structure of the MIS-TENG checklist. (a) Core descriptors, required for all triboelectric sensors. (b) Specific modules, required only when the corresponding architecture, interface, or application is present; a device may fall into more than one module. Reporting of durability performance follows the MIS-TENG-R module (Section 8.7). Operational definitions, units and coding rules for each core descriptor and MIS-TENG-R element are given in Table S1 *.

(a) Core Descriptors

Domain	Items to Report (C1–C24)	Recommended Test Practice	Application-Dependent Acceptance Criterion
Materials	Identity and composition of both contact layers (polymer, additives, fillers with loading) (C1); layer thicknesses (C2); electrode materials (C3)	-	-
Device	Operating mode (CS, LS, SEC, SFT, CFT) (C4); nominal active area (C5); layer stack and encapsulation (C6); conductor connection outside the active area (C7)	Conductors connected outside the active area	-
Test conditions	Measurand and stimulus amplitude (force or pressure, displacement or strain) (C8); frequency or velocity, and waveform (C9); preload and maximum separation (C10); number of preconditioning cycles and any charge-neutralization step (C11); T, RH, and atmosphere (C12); readout mode (V_{OC}, Q_{SC}, I_{SC}) (C13), instrument input impedance or feedback capacitance (C14), sampling rate, and applied filtering (C15)	Preconditioning until output stabilizes, i.e., until the mean peak output over successive blocks of cycles changes by less than a stated percentage (block size and criterion reported); controlled T and RH (e.g., 25 ± 2 °C, 40–60% RH when compatible with the application); input impedance $\gg 1/(2\pi f C_T)$	-
Output	Primary electrical quantity with its dispersion statistic (SD or SE, stated) with the number of cycles (C16); the number of independent devices on which it is computed (C17); sensitivity with output quantity, units, and range (C18); LoD with noise definition (C19); nonlinearity (% FS) with fitted range (C20); regression equation and residuals; repeatability (C21); response time with loading rate (C22); hysteresis for loading–unloading measurands (C23); drift whenever continuous or long-term use is claimed (C24)	≥10 cycles; $n \geq 3$ independent devices; residual analysis rather than R^2 alone	Maximum nonlinearity, hysteresis and drift, and minimum R^2 (e.g., hysteresis < 5% FS or $R^2 > 0.98$, often used for tactile and strain sensors), set by the intended application

(b) Modules

Module	Applies to	Additional Descriptors
M1	Planar and micro/nanostructured films	Areal roughness Sa, Sq (ISO 25178 [192]) and texture geometry (AFM, SEM, profilometry); ε_r at test frequency; surface chemistry (XPS, FTIR) when functionalization or treatment is claimed; nominal contact pressure. For piezoelectrically active layers (PVDF and copolymers, filled composites): polar-phase content, poling state and direction, and the control used to separate piezoelectric from triboelectric contributions.

Table 6. *Cont.*

(**b**) **Modules**		
Module	**Applies to**	**Additional Descriptors**
M2	Fiber- and textile-based devices	Fiber or yarn diameter and structure (coaxial, twisted, braided); fabric construction; definition of strain (gauge length, bending radius or angle); washing protocol and cycles; breathability (MVTR) for skin-worn textiles
M3	Porous and compressible layers (foams, aerogels, spacers)	Porosity and pore size; compressive modulus; compressive strain at measurement; recovery time between cycles
M4	Ionic and hydrogel-based conductors	Ionic conductivity; electrolyte and solvent composition; water content and its change during testing; operating temperature range
M5	Liquid–solid devices (droplet, flow, wave, DEG)	Liquid composition, ionic strength, conductivity, pH, and temperature; static contact angle and contact-angle hysteresis; droplet volume and impact velocity (or Weber number), or flow rate and channel geometry; surface preconditioning; controls separating contact electrification from electrokinetic contributions; position of the liquid in the quantified liquid triboelectric series (β), where available [39]
M6	Rotary, sliding, and freestanding devices	Rotation speed or sliding velocity; contact vs. non-contact gap; grating number and pitch; normal load in sliding; wear or transfer-film assessment; driving torque when efficiency is reported
M7	Cantilever, whisker, and other compliant 3D transducers	Beam material, length, and bending stiffness; contact height and deflection; deflection-to-force calibration; directional response (angular step)
A1	Wearable and biomedical use	Anatomical site and attachment; number of subjects and ethics approval; handling of motion artifacts; agreement with a reference method; skin-contact biocompatibility
A2	Chemical and analytical sensing	Analyte, matrix, and recognition element; number of calibration levels and replicates (≥5 levels recommended); selectivity against interferents; separation of triboelectric and electrochemical functions
A3	Outdoor and environmental use	Exposure duration and conditions (UV, rain, temperature range); cross-sensitivity to T and RH

* MIS-TENG is a minimum-information reporting framework proposed by the authors; it is not a measurement standard, prescribes neither test methods nor acceptance thresholds, and requires interlaboratory validation before any normative use. Abbreviations: CS, contact-separation; LS, lateral sliding; SEC, single-electrode contact; SFT, sliding freestanding; CFT, contact freestanding; T, temperature; RH, relative humidity; V_{OC}, open-circuit voltage; Q_{SC}, short-circuit charge; I_{SC}, short-circuit current; C_T, device capacitance; SD, standard deviation; SE, standard error; LoD, limit of detection; FS, full scale; ε_r, relative permittivity; Sa, arithmetical mean height; Sq, root-mean-square height; AFM, atomic force microscopy; SEM, scanning electron microscopy; XPS, X-ray photoelectron spectroscopy; FTIR, Fourier-transform infrared spectroscopy; MVTR, moisture vapor transmission rate; DEG, droplet-based electricity generator; CE, contact electrification; We, Weber number.

Table 7. Illustrative case studies: application of the MIS-TENG checklist (core descriptors C1–C24, Table 6a) and of the MIS-TENG-R items (R1–R5, Section 8.7) to six devices examined in this review. Codes, assigned with the workflow of Figure 12b and the decision rules of Table S1: R (green), reported in the main text; SI (blue), reported only in the Supporting Information; P (yellow), reported partially or ambiguously; N (red), not reported; NA (grey), not applicable and excluded from the denominator. Colors duplicate the letter codes and carry no additional information; superscript numbers refer to the notes below the table. CI, completeness index = (R + SI)/applicable items. Module codes as in Table 6b: M1, planar and micro/nanostructured films; M2, fiber- and textile-based devices; M3, porous and compressible layers; M6, rotary, sliding and freestanding devices; M7, cantilever, whisker and other compliant 3D transducers; A1, wearable and biomedical use; A3, outdoor and environmental use. V_{OC}, open-circuit voltage; Q_{SC}, short-circuit transferred charge; I_{SC}, short-circuit current; T, temperature; RH, relative humidity; LoD, limit of detection; FS, full scale. Each item was coded from the full text and the Supporting Information; item-level evidence is given in Table S2. The coding assesses the completeness of reporting, not device performance or experimental quality: the absence of an item prevents comparison across studies but does not necessarily imply an experimental shortcoming.

Descriptor	[46] Pressure	[112] Strain	[114] Vibration	[116] Vibration	[95] Force (Whisker)	[150] Wind Speed/Airflow Temp
			Core—Materials			
C1 Identity/composition of both contact layers	P	R	R	R	R	R
C2 Layer thicknesses	P	P	P	R	P	R
C3 Electrode materials	R	R	R	R	R	R
			Core—Device			
C4 Operating mode	R	R	P	R	R	R
C5 Nominal active area	P[1]	P	P	P	P	SI
C6 Layer stack and encapsulation	R	R	R	R	R	R
C7 Conductor connection outside active area	N	N	N	N	N	N
			Core—Test			
C8 Stimulus amplitude	SI	R	R	R	R	R
C9 Frequency/velocity and waveform	P	P	R	R	P	R
C10 Preload and maximum separation	N	P	P	P	P	R
C11 Preconditioning/charge neutralization	N	N	N	N	N	N
C12 T, RH, atmosphere	P	P	N	N	P	P
C13 Readout mode (V_{OC}, Q_{SC}, I_{SC})	P	R	R	R	R	R
C14 Instrument input impedance/feedback capacitance	P	P	P	P	P	P
C15 Sampling rate and filtering	P	P	P	P	P	P

Table 7. *Cont.*

Descriptor	[46] Pressure	[112] Strain	[114] Vibration	[116] Vibration	[95] Force (Whisker)	[150] Wind Speed/Airflow Temp
			Core—Output			
C16 Dispersion statistic with number of cycles	**N**	**N**	**N**	**N**	**P**	**P**
C17 Number of independent devices	**N**	**N**	**N**	**N**	**N**	**N**
C18 Sensitivity (quantity, units, range)	**R**	**P**	**P**[4]	**R**	**P**	**R**
C19 LoD with noise definition	**N**	**P**	**P**	**P**	**P**	**SI**[6]
C20 Nonlinearity (% FS)	**P**	**P**	**P**	**P**	**P**	**P**
C21 Repeatability	**N**	**P**	**N**	**P**	**N**	**P**
C22 Response time with loading rate	**R**	**R**[3]	**N**	**N**	**N**	**R**
C23 Hysteresis	**N**[2]	**N**	**NA**	**NA**	**N**	**NA**
C24 Drift	**P**	**P**	**P**	**P**	**P**	**P**
			MIS-TENG-R (reliability module, Section 8.7)			
R1 Environmental conditions of durability test	**N**	**N**	**N**	**N**	**N**	**N**
R2 Load amplitude, frequency, number of cycles	**P**	**R**	**P**[4]	**P**	**P**	**P**
R3 Acceptance/retention criterion	**N**	**N**	**N**	**N**	**N**	**N**
R4 Failure modes	**N**	**N**	**N**	**N**	**N**	**P**
R5 Number of devices in durability test	**N**	**N**	**N**	**N**	**N**	**N**
			Summary			
CI, core = (R + SI)/applicable	**6/24**	**7/24**	**6/23**	**9/23**	**6/24**	**13/23**
Core descriptors partially reported (P)	10	12	10	8	12	7
Core descriptors not reported (N)	8	5	7	6	6	3
CI, MIS-TENG-R = (R + SI)/5	**0/5**	**1/5**	**0/5**	**0/5**	**0/5**	**0/5**
Applicable modules (R + SI/applicable items)	M1 0/3; M3 0/4	M2 1/3; A1 1/5	M2 2/2	M1 0/3; M3 0/4	M7 ¾ [5]	M1 1/3; M6 2/5; A3 1/2

[1] Force (0–17 N) and pressure (0–30 kPa) scales cannot be reconciled without the loading area, which is not stated. [2] 'Hysteresis' in the SI denotes the temporal lag relative to the actuator, not the loading–unloading output difference of Table 1. [3] 70 ms at 5 Hz, 180 ms at 2 Hz: the response time depends on the loading rate. [4] Performance given as frequency error from a single comparison; durability given as run duration (≈1530 s at 30 Hz), from which ≈4.6×10^4 cycles is derived. [5] Coded against module M7, added after this analysis: contact height and deflection and directional response reported; deflection-to-force calibration only in the SI; beam length and bending stiffness not stated. [6] Noise-based detection limit given only in the SI; it nearly coincides with the lower bound of the stated operating range.

For durability tests, this structure is supplemented by the MIS-TENG-R module defined in Section 8.7, which specifies aging conditions, cyclic stress, retention, and failure mode. MIS-TENG and MIS-TENG-R therefore constitute a single reporting system articulated into a metrological core and a reliability module.

MIS-TENG complements, rather than replaces, the tools already available for generators and materials [22,23,26,30,103,104]; the two approaches share fundamental electrical quantities (V_{OC}, Q_{SC}) and should be presented jointly when a device is proposed for both functions (Section 9.4.2).

MIS-TENG must be considered a first version of a proposal subject to revision. Section 9.4.1 illustrates its use on six previously published devices as case studies; its constituent elements—and in particular the distinction between core descriptors and module descriptors—still require validation through systematic literature reviews and interlaboratory comparative measurements on shared device designs, ideally in coordination with standardization initiatives already under discussion [26]; a staged roadmap for this validation is outlined in Section 11.3.

9.4.1. Illustrative Case Studies: MIS-TENG Applied to Six Published Devices

To illustrate how the checklist is applied in practice, rather than to validate it, MIS-TENG was used to code six devices already discussed in this review as case studies: the three entries in Table 3 (pressure [46], deformation [112], and vibration [114]) and three devices illustrated in Figure 5, Figure 6, Figure 9 and Figure S3 (the "whisker" force sensor [95], the quasi-zero-stiffness vibration sensor [116], and the rotary sensor for wind and air-flow temperature [150]). The selection therefore follows the structure of the review rather than the expected result. Within this constraint, the six devices were chosen so that (i) both the full text and the Supporting Information were accessible for item-level coding; (ii) they span different measurands (pressure, strain, vibration, force, wind speed and airflow temperature), operating modes (contact–separation, single-electrode, rotary freestanding) and architectures (films, fibers, foams, cantilevers, rotary disks), thereby exercising seven of the ten modules (M1–M3, M6, M7, A1, A3); and (iii) they were published between 2022 and 2026. Each of the 24 core descriptors (Table 6a) and of the five MIS-TENG-R elements (Section 8.7) was coded, on the basis of the full text and the Supporting Information and according to the rules of Table S1, as follows: reported in the main text (R), reported only in the Supporting Information (SI), reported partially or ambiguously (P), not reported (N), or not applicable (NA, with justification) (Table 7; element-level evidence in Table S2).

Three observations emerge. First, completeness is uneven: the six studies fully report between 6 and 13 applicable core descriptors (out of 23–24 total), and only one MIS-TENG-R element is fully reported in any of the six studies (the cycling parameters in [112]). Second, in these six cases the gaps recur in the same descriptors rather than being scattered across the checklist. None of the six studies reports preconditioning or charge neutralization phases, the position of the conductor connections relative to the active area, measurements on independent devices, the environmental conditions of the durability test, a quantitative retention criterion, or independent replicates in durability tests. The measuring instrument is always stated, but its input impedance is never specified for the calibration measurements; sampling frequency and filtering are never fully described; linearity is never expressed as nonlinearity in % FS; and although four studies characterize the dependence of the output on humidity, none specifies the temperature and relative humidity at which the calibration itself was performed. Third, these gaps concern precisely the descriptors that determine comparability.

Two pairs of devices illustrate this last point. References [114,116] both concern vibration sensors, but Ref. [116] expresses performance as slope in V g^{-1} at a fixed frequency,

whereas Ref. [114] reports no slope and quantifies accuracy as a frequency error of 0.32%, obtained through a single comparison with a commercial accelerometer on a diesel engine. Neither reports temperature or humidity; moreover, the durability of [114] is given in terms of operating duration (≈1530 s at a dominant frequency of 30 Hz), so the value of $\approx 4.6 \times 10^4$ cycles reported in Table 3 is the result of a calculation and not a direct statement. Consequently, the two entries are not comparable in terms of sensitivity, environmental conditions, or durability. Similarly, the response times reported in Table 3 for [46] (25 ms) and [112] (70 ms) appear directly comparable, but were obtained under different loading conditions (a pressure step at 0.5 Hz versus stretching at 5 Hz); moreover, study [112] shows that the same device has a response time of 180 ms at 2 Hz. Since τ depends on the loading conditions, which C22 requires to be stated alongside it (Table S1), response times obtained at different excitation frequencies describe the test rather than the sensor.

The case studies also exposed limits of the framework itself. The "whisker" sensor [95] did not fall within any of the original modules M1–M6; this made it necessary to add module M7, dedicated to compliant cantilever transducers and three-dimensional transducers (Table 6b). On the other hand, some descriptors were presented in forms not envisaged by the checklist: in work [46], the term "hysteresis" denotes the temporal phase shift between sensor and actuator, rather than the difference between the loading and unloading phases defined in Table 1; in work [150], by contrast, a noise-based wind speed detection limit (2.15 m s^{-1}) appears exclusively in the Supporting Information and coincides almost perfectly with the lower limit of the declared operating range (2.2 m s^{-1}). Such cases confirm the advisability of explicitly evaluating each individual criterion, rather than limiting oneself to a binary pass/fail judgment, and of anchoring the terminology to what is established in Table 1. As these are only six studies, selected to follow the structure of the review, the exercise has purely illustrative value: it demonstrates neither the robustness nor the discriminating power of the checklist, and does not allow estimating the prevalence of documentation gaps; the natural next step consists of a systematic review involving independent double coding.

9.4.2. Positioning of MIS-TENG Relative to Existing Frameworks and Standards

Table 8 compares the MIS-TENG framework with the schemes, standards, and guidelines that currently regulate the evaluation of TENGs, or of measurements in general. It stands out for two characteristics. First, it is the only one to focus specifically on the triboelectric device used as a sensor. The figures of merit for generators [22,30], the quantified triboelectric series [23,86], and the IEC test methods [103,104] evaluate energy conversion or material charging. The testing guide by Mulvihill et al. [26] examines the factors that make a generator's output reproducible. Recent sensing-oriented figures of merit are confined to a single stimulus class, acoustic sensing, where they combine displacement and transferred charge [24] or normalize sensitivity to the effective sensor area (mV Pa^{-1} cm^{-2}), evaluated at a single sound pressure level and frequency [25]. Second, MIS-TENG constitutes a reporting framework rather than a test method or a specific metric. It prescribes what should be documented, without imposing the device's excitation modes or the values it should reach. Consequently, it can complement existing tools rather than compete with them. A test performed in accordance with IEC 62830-6 or -7 documents the descriptors of the test conditions for a contact–separation or sliding device; a figure of merit can also be included among the output descriptors.

Table 8. Positioning of MIS-TENG relative to existing frameworks, standards and guides. (a) Nature, scope and relationship with MIS-TENG. (b) Coverage of typical use cases.

(**a**)

Framework	Nature/Level	Object and Scope	What It Specifies	Relationship with MIS-TENG
Structural and material FOM_S [22]; breakdown-corrected output assessment [30]	Quantitative figures of merit; generator	Energy output per cycle of the five canonical modes; [30] adds the experimentally determined air-breakdown limit	FOM_S from the maximized V–Q cycle (geometry); $FOM_M \propto \sigma^2$ (material); accessible V–Q region	Complementary: MIS-TENG defines no FOM; shares V_{OC} and Q_{SC}; FOM_S reported alongside sensor descriptors for dual-function devices
Quantified triboelectric series [23,39,86]	Standardized measurement method and reference dataset; material	Polymers and inorganic non-metallic materials against liquid mercury; liquids (organic solvents, ionic solutions) against FEP [39]; controlled atmosphere, T and RH	Normalized charge density with uncertainty: α for solids, β (relative to deionized water) for liquids	α may be cited for the contact layers (C1, M1); β for the liquid (M5); does not characterize device or transfer function
IEC 62830-6:2019 [104]; IEC 62830-7:2021 [103]	International standards (test and evaluation methods); device	Energy-harvesting devices in vertical contact (-6) and linear sliding (-7) mode, as power sources	Terms, symbols, configurations, test methods and test report for performance characteristics	IEC tests can document C8–C15 for CS/LS devices; sensor metrics and other modes (SEC, freestanding, rotary, liquid–solid) are covered by MIS-TENG via M1–M7
Testing guide, Mulvihill et al. [26]	Community test-practice guide; test rig; proposal of an ISO committee	Reproducibility of TENG output (generator-oriented)	Fabrication, mechanical, electrical and environmental factors to control and report; preconditioning	Closest antecedent: its factors become test-condition descriptors and underpin MIS-TENG-R; MIS-TENG adds C18–C24, the core/module split and explicit "not measured" declarations
Sensing-specific FOM_S [24,25]	Single figure of merit; sensor, one stimulus class	Triboelectric [24] and hybrid triboelectric–piezoelectric [25] acoustic sensors	FOM combining displacement and transferred charge [24]; area-normalized sensitivity, $FOM_{sens} = V/(P{\cdot}A)$ (mV Pa^{-1} cm^{-2}), at a stated sound pressure level and frequency [25]	Not transferable to other stimuli; can be reported among output descriptors with C8–C15
GUM, VIM, ISO 5725, ISO 13528 [47,48,193–195]	Generic metrological standards	Any measurement	Uncertainty, vocabulary, precision, interlaboratory proficiency	Instantiated for TENG sensors (Sections 9.6 and 9.7) and used in the validation roadmap (Section 11.3); no replacement for an uncertainty budget

Table 8. *Cont.*

ISO 81060-2/-3, IEEE 1708 [129–131]	Clinical validation standards; system/application	Blood-pressure measuring devices	Reference method, population, acceptance criteria	Downstream of MIS-TENG: A1 records agreement with a reference method without criteria; compliance corresponds to level L5 (Table 4)

(b) ● Addressed · ◐Partially · ○ Not Addressed

Use Case	FOM_S [22,30]	Series [23,39,86]	IEC [103,104]	Guide [26]	Sensing FOM [24,25]	MIS-TENG (+R)
Compare energy output across geometries/modes	●	○	◐ [a]	◐	○	○
Rank and select contact materials	◐	●	○	○	○	○
Standardized test of harvester output	◐	○	● [a]	◐	○	○
Document test-rig and environmental conditions	◐	○	◐ [a]	●	○	●
Sensor transfer function (S, LoD, nonlinearity, hysteresis, response time, drift)	○	○	○	○	◐ [c]	●
Readout chain (input impedance/feedback capacitance, sampling, filtering)	○	○	○	◐	○	●
Architectures beyond CS/LS (SEC, freestanding, rotary, fiber, porous, ionic, liquid–solid, cantilever)	◐ [b]	○	○	◐	○	●
Durability and reliability reporting	○	○	●	◐	○	●
Interlaboratory precision	○	○	○	◐	○	◐ [d]
Application or clinical validation	○	○	○	○	○	◐ [e]
Machine-learning recognition performance	○	○	○	○	○	○

[a] Vertical contact and linear sliding modes only. [b] Five canonical solid–solid modes. [c] Acoustic sensing only. [d] Validation roadmap proposed (Section 11.3), not yet executed. [e] Agreement with a reference method, without acceptance criteria; see [129–131]. FOM_S, structural figure of merit; FOM_M, material figure of merit; σ, triboelectric surface charge density; V–Q, voltage–charge; V_{OC}, open-circuit voltage; Q_{SC}, short-circuit transferred charge; T, temperature; RH, relative humidity; CS, contact–separation; LS, lateral sliding; SEC, single-electrode contact; FOM_{sens}, sensing figure of merit (area-normalized acoustic sensitivity), where V is the output voltage, P the sound pressure and A the effective sensor area; GUM, Guide to the Expression of Uncertainty in Measurement; VIM, International Vocabulary of Metrology; L5, standard-compliant validation (Table 4).

Compared with generator-oriented frameworks, MIS-TENG asks authors to document three additional groups of information. First, the seven sensor metrology descriptors (C18–C24: sensitivity with its range, LoD with noise definition, nonlinearity, repeatability, response time as a function of loading rate, hysteresis, and drift) are not covered as a set by any of them; the sensing-specific FOM_S [24,25] address sensitivity alone, and only for acoustic stimuli. Second, the readout-system descriptors (C14–C15) make explicit, from a sensing perspective, the instrument impedance (already indicated by Mulvihill et al. among the factors to be controlled), adding the sampling frequency and filtering; the statistical descriptors (C16–C17), in turn, formalize the replication of tests. Finally, the module descriptors (M1–M7, A1–A3) and the reliability-related elements (R1–R5) apply only to the relevant architectures and applications. Most of this information is already available to the experimenter and simply needs to be documented. Additional measurements are required only for replicates on independent devices, load–unload cycles for hysteresis analysis, drift tests, and noise characterization for LoD determination. These are among the aspects most often missing in the six case studies of Section 9.4.1: data on independent devices (C17) were never reported; hysteresis (C23), where relevant, has never been comprehensively documented; drift (C24) was only partially addressed; and finally, the noise-based LoD (C19) was reported only once, within the supporting information (Table 7). This highlights where the greatest burden in terms of required documentation lies.

The comparison also clarifies the areas not covered by MIS-TENG (Table 8b). The framework does not replace generator figures of merit for energy evaluation, quantified series for material selection, or the test procedures defined by IEC standards. It does not establish acceptance thresholds and does not constitute a conformity assessment. It does not replace the calculation of measurement uncertainty according to the Guide to the Expression of Uncertainty in Measurement (GUM) [193], nor application-specific validation standards, such as those relating to blood pressure measurement [129–131], with respect to which it serves as a preliminary phase. Two further gaps also emerge: the current version does not examine the performance of machine-learning-based recognition systems (dataset composition, cross-validation schemes, subject independence), aspects addressed in many of the works discussed in Sections 5 and 6. Likewise, the energy autonomy of the complete sensing node is not considered (Section 6.3). Both aspects represent potential additions for future modules.

9.5. Benchmarking Framework and Data Visualization

Once reported according to the MIS-TENG framework, data can be organized into benchmarking maps, analogous to Ashby maps, based on homogeneous and declared test conditions; such maps can relate, for example, open-circuit voltage to dynamic pressure amplitude for tactile sensors, sensitivity to durability for strain sensors, or cycle-averaged power density to excitation frequency for vibration sensors (Figure S9). The adoption of shared graphical formats of this kind would also make the data reusable for machine-learning-based analyses [196]. Since the MIS-TENG framework does not constitute a conformity assessment, no minimum level of completeness in reporting is required; however, we propose that including a device in a quantitative comparison or in a benchmarking map be conditional, at a minimum, on the coding (according to the R or SI specifications) of the descriptors that define the transfer function and the related test conditions: identity of the contact layer (C1), nominal active area (C5), stimulus amplitude and frequency (C8, C9), temperature and relative humidity (C12), readout mode and input impedance or feedback capacitance (C13, C14), as well as sensitivity and its measurement range (C18).

9.6. Data Reproducibility and Statistical Validation

In addition to the reporting requirements of Tables 1 and 6, the recommended test practice ($n \geq 3$ independent devices, at least ten cycles, nonlinearity as % of full scale) should be followed whenever feasible, and any deviation should be stated; error bars should specify whether they represent the standard deviation or the standard error; calibration curves should include the regression equation and residuals. In accordance with VIM [47] and ISO 5725-1 [48], dispersion should be reported at three distinct levels. Repeatability refers to the same device, the same configuration, the same operator, and the same session, without reassembly operations; it is expressed as the coefficient of variation (CVr = SD/mean × 100%) of the primary quantity, calculated over at least ten consecutive cycles following a preconditioning phase, for each specified stimulus level. Intermediate precision within a laboratory concerns independently manufactured devices (C17) and, where indicated, may include the use of different manufacturing batches, days, or reassembly procedures; this parameter is expressed as the CV of the means obtained for each device, specifying the number of devices and batches examined. Reproducibility is reserved for interlaboratory conditions and is addressed in the validation plan described in Section 11.3 (sR). Measurements can be performed according to the first two levels, as demonstrated by a recent study on textile TENGs, which reported intra-device, inter-device, and between-batch coefficients of variation for nine devices from three distinct batches [124]. Target values such as $R^2 > 0.98$ and hysteresis $< 5\%$, often assumed as benchmarks for pressure and strain sensors, constitute comparison indicators rather than acceptance criteria. For vibration sensors, the repeatability of the frequency response across cycles should be reported, while for environmental sensors, the cross-sensitivity to temperature and humidity, as well as baseline recovery, should be indicated; where possible, the combined measurement uncertainty should be declared, in accordance with the GUM (Joint Committee for Guides in Metrology, JCGM 100:2008) [193].

9.7. Toward Metrological Traceability

A long-term goal is to establish metrological traceability, linking TENG measurements to SI units through an unbroken chain of calibrations with stated uncertainties (JCGM 200:2012) [47], using calibrated load cells, displacement sensors, and electrometers/charge calibrators. Reference materials (e.g., PTFE–Al pairs with certified composition, thickness, and topography, not yet available today) and calibration devices could provide reference outputs under defined conditions, and collaboration with national metrology institutes (NIST, PTB, INRiM) would formalize this link, opening the way to industrial certification of TENG-based sensors. The gap to be bridged remains wide: unlike, for example, the characterization of photovoltaic cells, international test methods for TENGs are limited to energy-harvesting evaluation of specific modes (IEC 62830-6:2019 for vertical contact mode [104]; IEC 62830-7:2021 for linear sliding mode [103]), and no standard yet addresses their use as sensors (Table 8); a dedicated ISO committee for TENG testing protocols has recently been proposed [26].

9.8. Databases and Open Benchmarking Initiatives

There is still no shared community repository for TENG performance data: data collected from the literature refer to different samples and measurement conditions, with a variance that limits analyses based on small datasets; the only homogeneous quantitative datasets consist of the triboelectric series, measured with a unique method for polymers and non-metallic inorganic materials [86] and, more recently, for liquids [39]. Correlating the quantitative descriptors of polymers (dipole moment, ε_r, surface energy) with performance metrics would enable data-driven materials design [196], provided that such data are

organized according to FAIR (findable, accessible, interoperable, reusable) principles [197] and fed through shared minimum-information reporting frameworks, such as the MIS-TENG proposal (Section 9.4) once validated.

10. Sustainability and Design Rules for Polymer-Based Self-Powered TENG Sensors

The rapid spread of technologies based on TENGs, especially those built with polymeric materials, has brought to the forefront the issue of their environmental footprint, recyclability, and end-of-life management. Although each individual device uses modest volumes of material, the large-scale deployment envisaged in wearable devices, Internet of Things nodes, and distributed sensor networks risks translating into a significant accumulation of polymer waste, often composite and therefore difficult to separate and recover. This section examines materials, processes, and end-of-life strategies and translates them into design rules (Section 10.8), building on Section 8.8.

10.1. Sustainability Challenges in Polymer TENGs

Polymers conventionally used in TENGs, such as PTFE, FEP, PVDF, and PDMS, offer high electrical and mechanical performance but are persistent and poorly biodegradable. For fluoropolymers, moreover, the presence of heavily fluorinated chemistry requires careful assessment of the impacts associated with production, treatment, and end-of-life [198,199]. To this is added the impact of microfabrication processes, plasma etching, solvent casting, and lithography, which generate chemical waste streams and entail non-negligible energy consumption. Sustainability in triboelectric research must therefore extend beyond conversion efficiency alone to encompass resource use, recyclability, and ecotoxicity of the entire device [198,199].

The main obstacles to sustainability are interconnected. The difficult integration of fluoropolymers and many silicones into conventional recycling streams, together with their high persistence, represents the most critical node, since these materials resist natural degradation and, in the case of fluoropolymers, production (fluorinated processing aids) and thermal treatment at end-of-life can release low-molecular-weight per- and polyfluoroalkyl substances (PFAS), which are persistent and mobile; for this reason fluoropolymers are included in the proposed universal PFAS restriction under discussion in the EU (ECHA, 2023) [200]; to this is added solvent-intensive manufacturing, often using DMF, acetone, or hexafluoroisopropanol (HFIP), whose management significantly affects the environmental balance. A further difficulty arises from the intrinsically composite nature of the devices, in which polymer layers, metal electrodes, and functional fillers are intimately coupled and therefore hard to separate at end-of-life. Finally, weighing on everything is the absence of a standardized and shared life-cycle assessment (LCA) for triboelectric devices, a field that still relies on few dedicated analyses, the first and most cited of which is discussed in Section 10.5.2 [198,199,201,202].

10.2. Biodegradable and Bio-Based Polymers for TENGs

A promising route consists in the use of biopolymers and naturally derived materials as triboelectric media. Their renewable origin and the possibility of degradation under defined conditions can reduce some impacts of persistent polymers; however, actual sustainability, degradation kinetics, and the nature of the final products must be verified case by case. More recent literature has shown that the rational pairing of these materials is no longer limited to low-performance proof-of-principle demonstrations: the reported results fall within the order of magnitude of those obtained with fluorinated systems, although they

have rarely been achieved under test conditions comparable to those used for benchmark fluorinated polymers (Section 10.7).

10.2.1. Natural Biopolymers

Among natural biopolymers, cellulose and bacterial cellulose (BC) occupy a central position: the abundance of hydroxyl groups gives them a positive triboelectric tendency and a pronounced hydrogen-bonding capability, while BC membranes combine high flexibility and large surface area, ideal characteristics for eco-TENGs [203]. Its derivatives, however, can shift markedly toward the negative side: a commercial clear cellulose film, in particular, ranks in the quantified triboelectric series above PTFE in its tendency to acquire negative charge ($\alpha = -1.18$ vs. -1.00) [23], opening the possibility of realizing all-cellulosic triboelectric pairs. Chitosan, an amine-functional biopolymer [204], has a triboelectric tendency tunable through surface group chemistry: the ratio between electron-donating groups ($–NH_2$, –OH) and carboxylic groups introduced during acid dissolution modifies the surface potential and, with it, the film's position in the triboelectric series and the device output [205]; processing variables matter as much as composition: residual acetic acid from dissolution and hot pressing of the film increase the output [206], while Mg^{2+} coordination raises the dielectric constant by 76% and the charge density by 75% [207]; the output can be further increased by introducing green plasticizers, which simultaneously modulate mechanical properties and electrical output [208]. Silk fibroin, a protein material, that offers flexibility, transparency, and biodegradability, is a candidate for resorbable TENGs; mesoscopic doping of regenerated fibroin with PU promotes the β-sheet transition, raising stretchability to ~250% and chemical stability up to 100 °C and pH 3–11, and the doped film acts as the tribo-positive layer against PTFE [209], although the PTFE counter-layer and Ag electrodes keep that device from being fully resorbable, while incorporation of two-dimensional nanofillers such as MXenes increases surface area and surface charge density [210]. Gelatin and starch, finally, complete the picture as water-processable materials compatible with green solvents, particularly suitable for transient and low-impact devices.

10.2.2. Biodegradable Synthetic Polymers

Alongside natural biopolymers, a growing role is played by biodegradable synthetic polymers. Polyesters such as Polylactic Acid (PLA) and Polyhydroxyalkanoates (PHA) offer more favorable degradation pathways than persistent polymers, but their compostability depends on formulation and environmental conditions; for PLA in particular, rapid degradation typically requires industrial composting conditions [198]. Polycaprolactone (PCL) and polybutylene succinate (PBS), by contrast, offer flexibility and are suitable for blending with cellulose or ionic dopants. To these are added supramolecular and dynamic covalent elastomers, for example polyurethanes cross-linked with disulfide bonds, which combine mechanical resilience and reprocessability, acting as bridge materials toward sustainable durability (cf. Section 8.8). The pairing of biodegradable polymers of opposite polarity allows the construction of fully biodegradable triboelectric pairs free of fluorinated components; since polarity is relative to the counter-material, the same polymer can occupy both sides: in the PLA–gelatin pair of [211], for instance, PLA acts as the electron donor and gelatin as the acceptor; devices of this kind, among the first fully biodegradable TENGs, combined electrospun PLA nanofibers with nanostructured gelatin films, achieving open-circuit voltages of about 500 V (560 V at 70 N) and peak power densities of about 5 W m^{-2} (4×4 cm^2, 50 N, 5 Hz, 80 MΩ load), values not normalized according to a common protocol; all materials composing the device dissolved in natural water at room temperature within about 40 days [211]. PBS–cellulose composites have shown charge densities comparable to PDMS-based TENGs tested under the same conditions and stable operation for over

10^4 cycles [212]; both pure PBS and a PBS/MCC composite (70 wt%) degraded under composting at 58 °C within about 70 days [212].

10.3. Eco-Dopants and Green Fillers

The incorporation of fillers and dopants of natural origin can increase polarization and charge retention, but biodegradability and ecotoxicity must be reassessed on the entire composite, since adding a functional phase does not automatically preserve the environmental profile of the matrix. Natural clays, such as montmorillonite and kaolinite, act as lamellar fillers that increase interfacial polarization and introduce charge-trapping sites; carbonized biomass, biochar, and lignin-derived carbons make it possible to tune conductivity and charge capture; bio-derived ionic liquids based on choline, citrate, or acetate act simultaneously as eco-friendly plasticizers and charge stabilizers [198]; and metal oxides such as ZnO and TiO_2, obtainable by sol–gel synthesis or green routes, increase effective permittivity; their biocompatibility does not, however, imply low environmental impact, since nanoscale forms (especially ZnO, due to Zn^{2+} release) exhibit significant aquatic ecotoxicity that must be assessed over the entire life cycle. In chitosan films, for example, a bio-derived plasticizer improves conformability and output only up to an optimal dosage, beyond which the loss of stiffness and effective surface charge degrades performance [208].

10.4. Transient and Resorbable TENGs

Beyond biodegradability, the concept of a transient triboelectric device envisages sensors designed to disintegrate physically or chemically at the end of their operating life, thereby eliminating electronic waste. Transient TENGs use water-soluble or bioresorbable polymers whose dissolution time window can be selected by design; such times depend, however, on degree of crystallinity, cross-linking, thickness, temperature, pH, and medium composition. PVA, gelatin, fibroin, and cellulose derivatives must therefore be described in terms of specific degradation conditions, avoiding universal times or the automatic assumption of innocuous final products. Blends of biopolymer with ionic liquids make it possible to modulate both flexibility and dissolution times. When these materials are combined with electrodes that are also transient, typically magnesium, zinc, or molybdenum, it is possible to realize fully resorbable triboelectric sensors for temporary physiological monitoring or implantable energy harvesting, capable of dissolving over times ranging from weeks (Mg) to months (Mo), with degradation products whose biocompatibility must be verified case by case [213]. The most recent frontier extends this paradigm to active control of degradation: triboelectric implants have been demonstrated whose dissolution is triggered and accelerated on demand by external stimulation: in an implantable PHBV/PVA–Mg TENG, low-intensity ultrasound drives the device, while intensities ≥ 3 W cm^{-2} initiate its dissolution [214], thus decoupling the operating window from the disappearance of the device. Such designs align TENG research with the broader paradigm of green transient electronics and circular materials science [213,214].

10.5. Sustainable Manufacturing and Life-Cycle Design

10.5.1. Green Processing

Water-based or solvent-free processes (e.g., aqueous casting of chitosan or hot-melt extrusion of PLA), additive manufacturing, and roll-to-roll processing of biopolymer films make it possible to reduce solvent use and material waste; lower process temperatures reduce thermal energy demand, provided that this advantage is not offset by longer processing times or the use of higher-impact reagents, an aspect that must be verified through a life cycle assessment (LCA) (Section 10.5.2).

10.5.2. LCA

A complete life-cycle assessment should quantify at least four dimensions: embodied energy (in MJ m^{-2}) associated with material synthesis and processing; CO_2-equivalent emissions referred to a declared functional unit (for example, one year of monitoring per measurement point for sensing, or 1 kWh delivered for energy harvesting), with explicit system boundaries (cradle-to-gate or cradle-to-grave) [215,216]; the energy balance of recycling or degradation; and toxicity indices of raw materials and by-products. The knowledge base in this area is, however, still limited: the reference analysis remains that of Ahmed et al., which compared two low-cost TENG modules (functional unit: 1 m^2 module; use phase, transport, and recycling excluded from system boundaries) with different photovoltaic technologies [199]. About 90% of primary energy was found to be associated with raw materials, and in particular with the acrylic substrate, the main contributor to embodied energy (78–97%) and climate change impact (74–81%), followed by the fluoropolymer film (PTFE, ~20% of embodied energy in the module that used a triple layer); on the process side, electrode deposition by sputtering absorbed most of the electrical energy of manufacturing [199]. Even with non-optimized laboratory fabrication routes, both modules showed aggregate environmental indicators lower than those of silicon and organic solar cells, although the less efficient module had a higher energy payback time than organic and perovskite cells. Two design indications follow: replace fossil-derived polymer substrates and reduce the energy of vacuum deposition processes, as the same authors recommend [199]. A more recent cradle-to-grave analysis of a wireless discharge triboelectric sensor confirmed them: PTFE synthesis contributes more than 60% to the device's global warming potential, due to c-C_4F_8 emissions associated with the chlorodifluoromethane (HCFC-22) supply chain, while the electrical consumption of physical vapor deposition dominates acidification [202]. Fully biopolymer pairs with transient electrodes (for example cellulose–Zn or PLA–Mg) act on both fronts, but the resulting footprint reduction has not yet been quantified by dedicated LCA analyses with homogeneous functional units and system boundaries.

10.6. Circularity and Reusability

Circular design aims at disassembly, repair, and reuse: modular architectures with mechanically separable electrodes and polymer layers, dynamic covalent bond matrices amenable to reprocessing, and solvent-assisted recovery of conductive fillers such as MXenes and carbon nanotubes; all while linking durability goals (Section 8.8) to material recovery.

10.7. Balancing Performance and Sustainability

Materials with lower environmental impact are not necessarily incompatible with high electrical performance; however, the record values reported in this field are rarely comparable with one another or with benchmark parameters based on fluoropolymers. They differ in driving mode (manual or controlled), generation mechanism (capacitive conduction or electrostatic discharge), and normalization criteria (instantaneous peak power or average power per cycle; active area or total device area). Consequently, any comparison requires homogeneous mechanical conditions, active area, load, and normalization method (Section 9). With this caveat, systems based on cellulose, chitosan, silk, or PLA have achieved significant voltages and power densities [198,203,211,217,218]. A well-documented example is represented by fully cellulose-based TENGs: using regenerated cellulose and cellophane as triboelectric layers and graphite sheet electrodes, a peak power density of 98 W m^{-2} was recorded under controlled excitation conditions via a linear motor (1 m s^{-1}), a value that rises to 307 W m^{-2} under manual actuation, the latter not reproducible as a benchmark parameter, while maintaining stable operation for over 3×10^4 cycles and over a relative

humidity range between 30% and 84% [217]. More recent developments have pushed this frontier further: engineered papers coated with nano-graphite, obtainable on an industrial scale and proposed as substitutes for engineering plastics and metal electrodes, have reached instantaneous peak power densities above 14 kW m^{-2} through a surface electrostatic discharge of very short duration, a mechanism distinct from capacitive conduction, so that the value is not comparable with the power densities of conventional TENGs (Section 9) [218]. The challenge that remains open is therefore not so much achieving a single high metric, but integrating within a single framework mechanical robustness, environmental stability, and controlled end-of-life degradability, a task requiring collaboration among polymer chemists, materials scientists, and sustainability analysts.

10.8. Design Rules for Sustainable Triboelectric Sensors

The indications discussed in the previous paragraphs can be reduced to five complementary criteria, which act jointly rather than as isolated constraints (Figure 13): three of them correspond to life-cycle stages (raw materials, processing, end-of-life), one, minimum toxicity, crosses them all, from raw material sourcing to end-of-life, while the fifth constrains them all. At the basis is the choice of raw materials of renewable origin, natural polymers, and biomass whose environmental benefit must nevertheless be verified on an LCA basis, since biological origin does not in itself imply lower impact, pursued together with the principle of minimum toxicity, which excludes persistent fluorinated or halogenated species and toxic metals (for example Pb, Cd, Hg, Cr(VI)). Upstream of the device, processing should remain low-energy, favoring water-based processes under ambient conditions; downstream, end-of-life should be conceived as recyclable or biodegradable, so as to ensure benign degradation, under declared conditions and standards, or material recovery of the entire device, including electrodes and encapsulation.

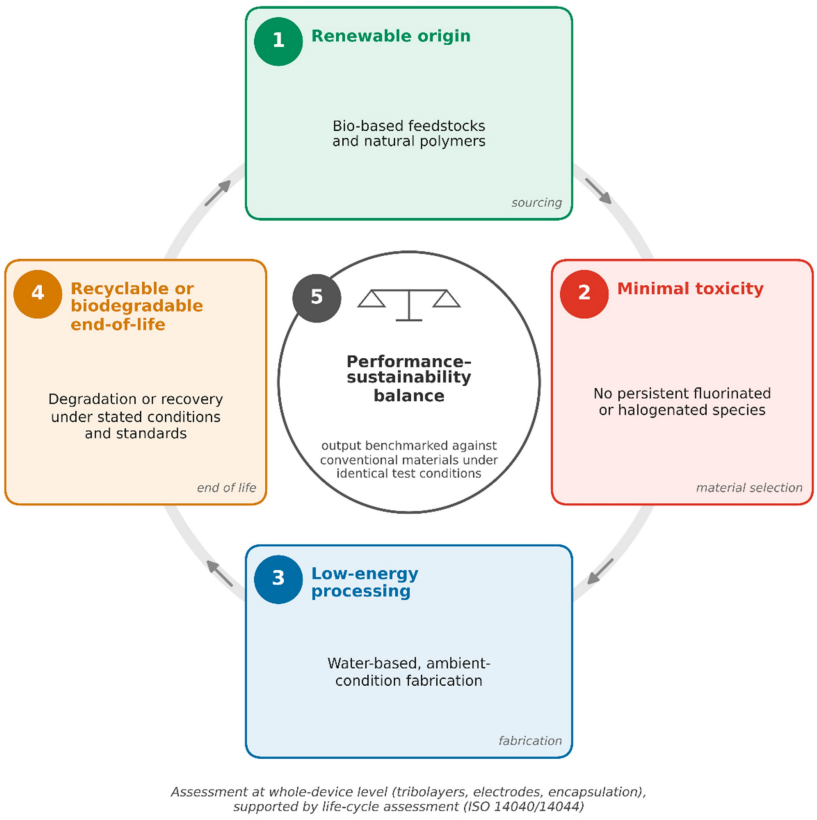


Figure 13. Design rules for sustainable triboelectric sensors. Three criteria correspond to life-cycle stages: renewable origin of raw materials (1), low-energy processing in aqueous medium and under

ambient conditions (3), and end-of-life with recycling or biodegradation under declared conditions and standards (4); minimum toxicity (2) crosses all stages. The fifth criterion, functional adequacy, constrains them all: performance must be sufficient for the intended application and evaluated together with production, durability, and end-of-life impacts. The assessment concerns the entire device, including electrodes and encapsulation, and is supported by life-cycle assessment (ISO 14040/14044) [215,216]. Original elaboration by the authors.

According to the criterion of functional adequacy (Figure 13), equivalence with the maximum performance of conventional materials is not required; what is necessary is a transparent balance between function and environmental cost.

11. Conclusions and Perspectives

This review has traced the path from contact electrification through materials, device design, applications, reliability, metrology, and sustainability of polymer-based TENG sensors. Its main contribution consists of the critical synthesis summarized in Section 11.1; the MIS-TENG framework, discussed in Section 11.2, represents the proposal that arises from the gaps that emerged in that synthesis.

11.1. Key Insights and Milestones

Five conclusions emerge. First, polymers are functional platforms rather than passive supports: molecular design, dipole alignment, surface functionalization, and nanofillers act jointly on charge generation and retention (Section 3). Second, architecture and readout determine whether a TENG operates as a generator or as a sensor with an approximately linear transfer function over a specified range, and air gaps, spacers, and microtextures regulate its sensitivity (Sections 4 and 5). Third, wearable and biomedical use reduces battery dependence only when the energy and signal paths are separated and autonomy is assessed for the entire chain (Section 6.3); moreover, biomedical demonstrations have so far reached at most healthy-volunteer pilot or preclinical level, so that clinical utility remains to be established (Table 4), while liquid–solid interfaces extend sensing to droplets, wind, and flows (Section 7). Fourth, reliability and sustainability now define technological maturity, with self-healing, biodegradable, and transient polymers bridging the two (Sections 8 and 10). Fifth, in every application domain the main obstacle to quantitative comparison is not device performance but the heterogeneity of test conditions and reported metrics (Sections 5.6, 7.5 and 9.4.1).

11.2. Still-Open Challenges

Despite rapid progress, some critical issues remain, both fundamental and technological. The first concerns charge control and predictability: contact electrification is extremely sensitive to the microscopic state of surfaces, contact history and the environment, conditions that limit quantitative modeling and reproducibility. Atomic-scale understanding of the relative contribution of electronic, ionic and material transfer also remains incomplete. Static loads also remain inaccessible to the triboelectric element alone (Section 4.4), so applications requiring a static component must rely on hybrid transduction.

Closely connected is the question of signal standardization and metrology. The absence of shared test protocols continues to make fair comparison between materials and devices difficult: the figures of merit and standards currently available (IEC 62830-6 and -7) [103,104] concern the energy evaluation of the harvester, whereas recognized metrics for the TENG as a sensor are lacking. MIS-TENG (Section 9.4), together with its reliability module MIS-TENG-R (Section 8.7), addresses this gap on the sensor side and complements the generator- and material-level references [22,23,30] and the IEC test methods [103,104] (Table 8). Compared with these references, the proposed framework offers four specific advantages. First, it gathers into a single set the metrological descriptors of sensors (sen-

sitivity and its range, noise-based limit of detection, nonlinearity, repeatability, response time as a function of loading rate, hysteresis, and drift); this is a set of parameters that no existing framework covers in its entirety, since, in the field of acoustic sensing, figures of merit are often limited to sensitivity alone [24,25]. Second, the framework makes explicit the documentation concerning the readout chain (input impedance or feedback capacitance, sampling, filtering) and the replication of results on independent devices. Third, its structure based on a core plus additional modules allows it to be applied to operating modes and architectures that fall outside the scope of IEC test methods, as in the case of single-electrode, freestanding, rotational, fiber-based, ionic, liquid-solid, or cantilever-based devices. Fourth, the coding of individual parameters, accompanied by operational definitions (Table S1, Figure 12b), makes it possible to verify the completeness of a report and to identify the minimum subset of descriptors necessary for a device to be included in a quantitative comparison (Section 9.5). Since the framework prescribes which aspects to document, rather than defining how to perform the tests or which values to achieve, the MIS-TENG framework can be used alongside other figures of merit and IEC tests; its adoption essentially requires the documentation of information already available to the experimenter (Section 9.4.2). In the six case studies of Section 9.4.1, the descriptors most often missing are precisely those that govern comparability (instrument input impedance, preconditioning, replicates across different devices, acceptance criteria related to durability); its usefulness, as well as the very distinction between core and module, will nevertheless need to be verified through adoption by multiple groups, interlaboratory tests, and comparison with future standardization initiatives (Section 11.3).

Finally, durability under real conditions (Section 8), the integration of harvesting, sensing, storage, and communication in thin, conformable formats (Section 6.5), and the balance between performance and end-of-life impact (Section 10) remain open.

11.3. Future Research Directions

The evidence discussed in the review points to three particularly relevant development axes, schematized in Figure 14 together with the common metrological basis on which they rest.

The first axis is materials intelligence. This means moving toward rational design of polymers engineered at the molecular level, with controlled dipolar orientation and well-defined energy levels, and exploring ionic, zwitterionic and supramolecular systems capable of linking electronic charge transfer to ionic charge transfer. From this perspective, artificial-intelligence-assisted materials discovery, combined with high-throughput screening, plays a growing role as a route to identify optimal compositions from the emerging triboelectric datasets [196], whose value will depend on standardized and comparable reporting (Section 9).

The second axis is functional integration. On the one hand, this means incorporating TENGs into flexible electronics systems that combine sensing, logic and wireless transmission, and creating multimodal triboelectric platforms capable of simultaneously detecting pressure, temperature and biosignals, decoupling their cross-sensitivities through dedicated channels, hybrid transduction or algorithmic separation; on the other hand, intelligent signal interpretation will increasingly be entrusted to machine-learning-based pattern recognition. At the same level is hybridization with other conversion mechanisms, piezoelectric, electromagnetic, photovoltaic, in hybrid nanogenerators, which synergistically exploit multiple energy sources to overcome the power limits of individual devices, coupled with storage and electronic loads without loading the source when the same element is also used as a sensor (Sections 4.1 and 6.3).

The third axis, that of sustainability and circularity, follows the design criteria defined in Section 10.8: biodegradable and transient devices, design oriented toward recovery or degradation under predetermined conditions, and life cycle assessment integrated into the optimization of materials and devices. All three axes presuppose the availability of comparable data: the discovery of new materials, the comparison between multimodal platforms, and life cycle assessment require shared measurement protocols and FAIR open data, which can be fed by structured reporting systems such as MIS-TENG (Section 9; Figure 14).

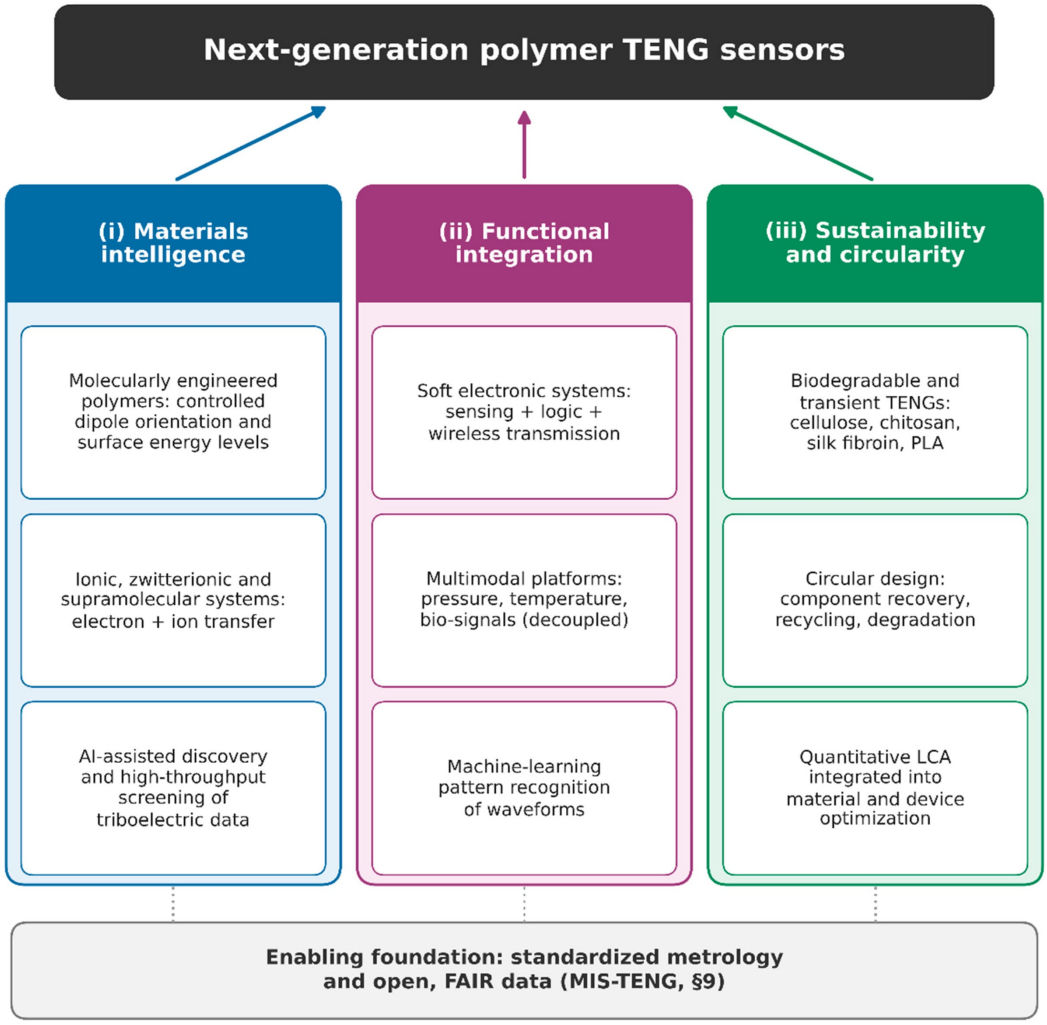


Figure 14. Future research directions for polymeric TENG sensors, organized along three axes: (i) materials intelligence, with polymers engineered at the molecular level, ionic, zwitterionic and supramolecular systems, and artificial-intelligence-assisted materials discovery; (ii) functional integration, with flexible electronic systems, multimodal platforms with decoupled cross-sensitivities, and pattern recognition via machine learning; (iii) sustainability and circularity, with biodegradable and transient devices, circular design and quantitative life cycle assessment. The three axes rest on a common basis of comparable metrology and FAIR open data, for which MIS-TENG (Section 9) is proposed as a reporting framework, itself subject to the staged interlaboratory validation described in the text. Conceptual diagram derived from the synthesis of the review; original elaboration by the authors.

Since this common metrological basis is itself a proposal, its validation is a prerequisite for all three axes; we therefore suggest organizing it as collective work developed in several phases. Such work could begin with a literature phase, in which independent double coding of a systematic sample of studies based on the MIS-TENG checklist would make it possible to verify the clarity of each descriptor and the distinction between core and modular descriptors (Section 9.4.1). The next step would be a protocol phase, in which a coordinating laboratory would define a common test protocol specifying the excitation (actuator, force or displacement, frequency, waveform), the preconditioning, the temperature and relative humidity, and the readout system. Transferred charge, measured in charge mode, would be taken as the primary quantity, since it is the least sensitive to loading introduced by the measuring instrument (Table 1, Section 4.5); open-circuit voltage (V_{OC}) would be acquired through inputs with electrometer-like characteristics. This would be followed by an interlaboratory round-robin comparison, in which identical reference devices, for example, units based on contact-separation between PTFE and aluminum (Section 9.7), would circulate among a sufficient number of laboratories to obtain precision estimates (usually no fewer than eight) [48,194], thereby isolating the contribution of the test rig. A second cycle, in which each laboratory would fabricate the devices from a common material kit and a common procedure, would make it possible to include variability related to fabrication. Each laboratory would provide the raw waveforms together with the completed checklist. In an analysis phase, repeatability and reproducibility standard deviations (sr, sR) would then be calculated after excluding outliers [194], and the performance of individual laboratories would be expressed through z-scores [195]. Descriptors showing insufficient reproducibility would therefore be redefined or accompanied by stricter test prescriptions. Finally, the data set would be made available according to the FAIR principles [197]. The revised methodological framework would be presented within the standardization initiatives currently under discussion [26], thereby complementing the IEC test methods focused on generators [103,104].

11.4. Interdisciplinary Convergence and Final Perspective

Progress in polymeric TENG sensors will depend on integration among polymer and surface chemistry, mechanical and electrical engineering, biomedical and environmental sciences, metrology and data science. Technological maturation will require not only higher electrical outputs, but reproducible transfer functions, reliability demonstrated under real conditions, efficient interface electronics and sustainability criteria verified over the life cycle. From this perspective, the value of TENGs does not lie in the idea of universally replacing conventional sensors and sources, but in the possibility of integrating transduction, energy harvesting and information in soft and distributed architectures where such integration offers a measurable advantage. The transition from prototypes to robust applications will therefore depend on convergence among materials design, standardization and validation specific to the end use.

Supplementary Materials: The following supporting information can be downloaded at: https://www.mdpi.com/article/10.3390/s26237492/s1, Figure S1: Surface structuring via wrinkling and transfer; Figure S2: Mechanical compliance of a polymeric triboelectric layer with a phase-locked structure; Figure S3: Machine-learning decoding in a reconfigurable whisker array; Figure S4: Stretchable particulate-dielectric TENG; Figure S5: AIoT health-management system; Figure S6: Glucose response of the PVDF–PCL/PPy/GO TENG; Figure S7: Standardized output-capability method accounting for breakdown; Figure S8: Constructive elements of a TENG for reproducible tests; Figure S9: Ashby-style benchmarking maps; Table S1: Operational definitions, units and coding rules for the MIS-TENG core descriptors and MIS-TENG-R elements; Table S2: Item-level evidence for the MIS-TENG coding of Table 7.

Author Contributions: Conceptualization, A.P. and G.D.P.; writing—original draft preparation, A.P. and G.D.P.; writing—review and editing, A.P. and G.D.P.; visualization, A.P. and G.D.P. All authors have read and agreed to the published version of the manuscript.

Funding: This research received no external funding.

Institutional Review Board Statement: Not applicable.

Informed Consent Statement: Not applicable.

Data Availability Statement: Operational definitions and coding rules for the MIS-TENG core descriptors are provided in Table S1. The item-level coding underlying Table 7 is provided in Table S2 of the Supplementary Materials. No other new data were created.

Conflicts of Interest: The authors declare no conflicts of interest.

Abbreviations

The following abbreviations are used in this manuscript:

ε_r	Relative permittivity
A_{eff}	Effective contact area
AFM	Atomic force microscopy
AgNW	Silver nanowire
AIoT	Artificial intelligence of things
BLE	Bluetooth low energy
CFT	Contact freestanding triboelectric-layer mode
CI	Completeness index
CNN	Convolutional neural network
CNT	Carbon nanotube
CS	Vertical contact-separation mode
CV	Coefficient of variation
DEGs	Droplet-based electricity generators
ECG	Electrocardiogram
EDI	Environmental durability index
EDL	Electric double layer
EDS	Energy dispersive spectroscopy
EEG	Electroencephalogram
EHD	Electrohydrodynamic
EMG	Electromyography
EOG	Electrooculography
FEP	Fluorinated ethylene propylene
FEV_1	Forced expiratory volume in the 1st second
FFT	Fast fourier transform
FS	Full scale
FOM_M	Material figure of merit
FOM_s	Structural figure of merit
FOM_{sens}	Sensing figure of merit (area-normalized acoustic sensitivity)
FTIR	Fourier-transform infrared spectroscopy
FVC	Forced vital capacity
GO	Graphene oxide
GOx	Glucose oxidase
GUM	Guide to the expression of uncertainty in measurement
HALS	Hindered amine light stabilizers
HSVS-TENG	High-sensitivity vibration sensor triboelectric nanogenerator
IoT	Internet of things
I_{SC}	Short-circuit current
ITO	Indium tin oxide

LCA	Life-cycle assessment
LoD	Limit of detection
LS	Lateral sliding mode
LSTM	Long short-term memory
MAE	Mean absolute error
MIS-TENG	Minimum information set for triboelectric sensors (proposed framework)
MIS-TENG-R	MIS-TENG reliability module
ML	Machine learning
MVTR	Moisture vapor transmission rate
NFC	Near field communication
PCL	Poly(ε-caprolactone)
PDMS	Polydimethylsiloxane
PEDOT:PSS	Poly(3,4-ethylenedioxythiophene):poly(styrene sulfonate)
PE	Polyethylene
PEI	Poly(ethyleneimine)
PEO	Polyethylene oxide
PFAS	Per- and polyfluoroalkyl substances
PHA	Polyhydroxyalkanoates
PLA	Polylactic acid
PMC	Power-management circuit
PMMA	Poly(methyl methacrylate)
PP-TENG	PTFE-micro-particle-based triboelectric nanogenerator
PPy	Polypyrrole
PTFE	Polytetrafluoroethylene
PTT	Pulse transit time
PU	Polyurethane
PVA	Poly(vinyl alcohol)
PVC	Poly(vinyl chloride)
PVDF	Polyvinylidene fluoride
PVDF–CTFE	Poly(vinylidene fluoride-chlorotrifluoroethylene)
P(VDF–TrFE)	Poly(vinylidene fluoride-trifluoroethylene)
PWV	Pulse-wave velocity
Q_{SC}	Transferred charge (when measured under short-circuit conditions)
Q_{tr}	Transferred charge
RCPTG	Compliant iontronic triboelectric gel with phase-locked structure
RH	Relative humidity
R_L	Load resistance
RO-TWSA	Reconfigurable omnidirectional triboelectric whisker sensor array
SAMs	Self-assembled monolayers
SD	Standard deviation
SE	Standard error
SEC	Single-electrode contact mode
SEM	Scanning electron microscopy
SFT	Sliding freestanding triboelectric-layer mode
SNR	Signal-to-noise ratio
TENG	Triboelectric nanogenerator
TPU	Thermoplastic polyurethane
VIM	International vocabulary of metrology
V_{OC}	Open-circuit voltage
XPS	X-ray photoelectron spectroscopy

Appendix A

Table A1. Search strings used in Scopus (field TITLE-ABS-KEY; search date: 15 July 2026). All strings were combined with the filters PUBYEAR > 2011 AND PUBYEAR < 2027, document type article or review, and language English. Records overlap across strings and are reported only as an indication of the volume of the literature.

Thematic Block	Keywords Combined with "Triboelectric Nanogenerator*" AND Polymer*	Records 2012–2026	of Which 2023–2026
Polymer materials and surface engineering	("surface charge density" OR dielectric OR "surface engineering" OR functionalization)	229	157
Device architectures and operating modes	"contact-separation" OR "single-electrode" OR freestanding OR "working mode" OR "device architecture"	160	102
Mechanical sensing	("pressure sensor" OR "strain sensor" OR "vibration sensor" OR tactile) AND "self-powered"	60	45
Wearable and biomedical sensing	wearable OR "health monitoring" OR pulse OR respiration OR "e-skin" OR biomedical	330	236
Environmental and analytical sensing	wind OR raindrop OR droplet OR "flow sensor" OR "self-powered electrochemical" OR environmental	185	135
Durability and reliability	durability OR "self-healing" OR encapsulation OR "charge decay" OR "charge retention" OR humidity OR aging	235	154
Metrology and standardization	"figure of merit" OR standardization OR reproducibility OR benchmarking OR "performance metrics"	98	44
Sustainability and biodegradable materials	biodegradable OR sustainable OR cellulose OR chitosan OR "silk fibroin" OR transient OR "life cycle"	313	220

References

1. Wang, S.; Lin, L.; Wang, Z.L. Nanoscale Triboelectric-Effect-Enabled Energy Conversion for Sustainably Powering Portable Electronics. *Nano Lett.* **2012**, *12*, 6339–6346. [CrossRef] [PubMed]
2. Cheng, T.; Shao, J.; Wang, Z.L. Triboelectric Nanogenerators. *Nat. Rev. Methods Primer* **2023**, *3*, 39. [CrossRef]
3. Liu, D.; Zhang, J.; Cui, S.; Zhou, L.; Gao, Y.; Wang, Z.L.; Wang, J. Recent Progress of Advanced Materials for Triboelectric Nanogenerators. *Small Methods* **2023**, *7*, 2300562. [CrossRef] [PubMed]
4. Fan, F.-R.; Tian, Z.-Q.; Lin Wang, Z. Flexible Triboelectric Generator. *Nano Energy* **2012**, *1*, 328–334. [CrossRef]
5. Cui, Y.; Yang, T.; Luo, H.; Zheng, Y. Triboelectric Nanogenerators Promote Self-Powered Sensing and Intelligent Monitoring. *Sensors* **2026**, *26*, 2984. [CrossRef] [PubMed]
6. Olson, K.P.; Marks, L.D. What Puts the "Tribo" in Triboelectricity? *Nano Lett.* **2024**, *24*, 12299–12306. [CrossRef] [PubMed]
7. Jimidar, I.S.M.; Kwiecinski, W.; Roozendaal, G.; Kooij, E.S.; Gardeniers, H.J.G.E.; Desmet, G.; Sotthewes, K. Influence of Wettability and Geometry on Contact Electrification between Nonionic Insulators. *ACS Appl. Mater. Interfaces* **2023**, *15*, 42004–42014. [CrossRef] [PubMed]
8. Verners, O.; Lapčinskis, L.; Sherrell, P.C.; Šutka, A. Contact Electrification at Dielectric Polymer Interfaces: On Bond Scission, Material Transfer, and Electron Transfer. *Adv. Mater. Interfaces* **2023**, *10*, 2300562. [CrossRef]
9. Costa, C.M.; Cardoso, V.F.; Martins, P.; Correia, D.M.; Gonçalves, R.; Costa, P.; Correia, V.; Ribeiro, C.; Fernandes, M.M.; Martins, P.M.; et al. Smart and Multifunctional Materials Based on Electroactive Poly(Vinylidene Fluoride): Recent Advances and Opportunities in Sensors, Actuators, Energy, Environmental, and Biomedical Applications. *Chem. Rev.* **2023**, *123*, 11392–11487. [CrossRef] [PubMed]
10. Linarts, A.; Sherrell, P.C.; Mālnieks, K.; Ellis, A.V.; Šutka, A. Electrospinning Triboelectric Laminates: A Pathway for Scaling Energy Harvesters. *Small* **2023**, *19*, 2205563. [CrossRef] [PubMed]
11. Sardana, S.; Sharma, V.; Beepat, K.G.; Sharma, D.P.; Chawla, A.K.; Mahajan, A. Flexible, Humidity- and Contamination-Resistant Superhydrophobic MXene-Based Electrospun Triboelectric Nanogenerators for Distributed Energy Harvesting Applications. *Nanoscale* **2023**, *15*, 19369–19380. [CrossRef] [PubMed]

12. Šutka, A.; Lapčinskis, L.; He, D.; Kim, H.; Berry, J.D.; Bai, J.; Knite, M.; Ellis, A.V.; Jeong, C.K.; Sherrell, P.C. Engineering Polymer Interfaces: A Review toward Controlling Triboelectric Surface Charge. *Adv. Mater. Interfaces* **2023**, *10*, 2300323. [CrossRef]
13. Liu, X.; Zhao, Z.; Gao, Y.; Nan, Y.; Hu, Y.; Guo, Z.; Qiao, W.; Wang, J.; Zhou, L.; Wang, Z.L.; et al. Triboelectric Nanogenerators Exhibiting Ultrahigh Charge Density and Energy Density. *Energy Environ. Sci.* **2024**, *17*, 3819–3831. [CrossRef]
14. Xu, L.; Bu, T.Z.; Yang, X.D.; Zhang, C.; Wang, Z.L. Ultrahigh Charge Density Realized by Charge Pumping at Ambient Conditions for Triboelectric Nanogenerators. *Nano Energy* **2018**, *49*, 625–633. [CrossRef]
15. Liu, W.; Wang, Z.; Wang, G.; Liu, G.; Chen, J.; Pu, X.; Xi, Y.; Wang, X.; Guo, H.; Hu, C.; et al. Integrated Charge Excitation Triboelectric Nanogenerator. *Nat. Commun.* **2019**, *10*, 1426. [CrossRef] [PubMed]
16. Liu, Y.; Liu, W.; Wang, Z.; He, W.; Tang, Q.; Xi, Y.; Wang, X.; Guo, H.; Hu, C. Quantifying Contact Status and the Air-Breakdown Model of Charge-Excitation Triboelectric Nanogenerators to Maximize Charge Density. *Nat. Commun.* **2020**, *11*, 1599. [CrossRef] [PubMed]
17. Jia, X.; Wu, X.; Qi, L.; Dai, X.; Wang, J.; Jiang, T.; Hong, Z. $CaTiO_3$/ZnO-PVDF Composite-Based Triboelectric Nanogenerators for Self-Powered Gait Sensing. *Adv. Funct. Mater.* **2025**, *35*, e07124. [CrossRef]
18. Gao, S.; Sun, Y.; Long, L.; Liu, Y.; Wang, J. A Ternary-Dielectric Dual-Domain Triboelectric Nanogenerator for High Charge Density and Tail-Charge Suppression. *Energy Environ. Sci.* **2026**, *19*, 2569–2584. [CrossRef]
19. Guo, M.; Xia, Y.; Liu, J.; Zhang, Y.; Li, M.; Wang, X. Wearable Pressure Sensor Based on Triboelectric Nanogenerator for Information Encoding, Gesture Recognition, and Wireless Real-Time Robot Control. *Adv. Funct. Mater.* **2025**, *35*, 2419209. [CrossRef]
20. Chen, D.; Cui, R.; Huang, C.; Wang, Z.; Niu, L. Wearable Mechanoluminescent Triboelectric Sensors for Real-Time Monitoring of Nighttime Sports Activities. *ACS Appl. Mater. Interfaces* **2025**, *17*, 18844–18851. [CrossRef] [PubMed]
21. Xu, L.; Zhong, S.; Yue, T.; Zhang, Z.; Lu, X.; Lin, Y.; Li, L.; Tian, Y.; Jin, T.; Zhang, Q.; et al. AIoT-enhanced Health Management System Using Soft and Stretchable Triboelectric Sensors for Human Behavior Monitoring. *EcoMat* **2024**, *6*, e12448. [CrossRef]
22. Zi, Y.; Niu, S.; Wang, J.; Wen, Z.; Tang, W.; Wang, Z.L. Standards and Figure-of-Merits for Quantifying the Performance of Triboelectric Nanogenerators. *Nat. Commun.* **2015**, *6*, 8376. [CrossRef] [PubMed]
23. Zou, H.; Zhang, Y.; Guo, L.; Wang, P.; He, X.; Dai, G.; Zheng, H.; Chen, C.; Wang, A.C.; Xu, C.; et al. Quantifying the Triboelectric Series. *Nat. Commun.* **2019**, *10*, 1427. [CrossRef] [PubMed]
24. Hui, X.; Hu, Z.; Ren, Y.; Gong, S.; Zhou, H.; Chen, J.; Guo, H. Reviving Acoustic Sensing via a Triboelectric Nanogenerator: Principle, Progress, and Perspective. *Int. J. Extrem. Manuf.* **2026**, *8*, 022012. [CrossRef]
25. Shahbaz, I.; Yao, Z.; Rehman, S.; Deng, J.; Song, Y.; Li, L. Self-Powered Triboelectric–Piezoelectric Hybrid Acoustic Sensor with Microcone Patterned Film Based on Poly(Vinylidene Fluoride)/LNKNTS-Mn Nanorods Composite. *Adv. Funct. Mater.* **2026**, *36*, e14004. [CrossRef]
26. Mulvihill, D.M.; Mukherjee, R.; Xu, Y.; Kumar, C.; Khandelwal, G.; Perris, J.; Bairagi, S.; Aliyana, A.K.; Stylios, G.K.; Pillai, S.C.; et al. How to Test Triboelectric Nanogenerators: Key Factors for Standardized Performance Evaluation. *Adv. Energy Mater.* **2025**, *15*, e02920. [CrossRef]
27. Rahman, M.T.; Rahman, M.S.; Kumar, H.; Kim, K.; Kim, S. Metal-Organic Framework Reinforced Highly Stretchable and Durable Conductive Hydrogel-Based Triboelectric Nanogenerator for Biomotion Sensing and Wearable Human-Machine Interfaces. *Adv. Funct. Mater.* **2023**, *33*, 2303471. [CrossRef]
28. Le, H.A.T.; Luu, T.T.; Dinh, D.; Rhee, K.; Choi, K.; Choi, D.; Park, Y.T. Transparent and Robust LiCl–Organohydrogel Triboelectric Nanogenerator With Deep Learning Assisted Sensing. *Adv. Funct. Mater.* **2026**, *36*, e76403. [CrossRef]
29. Ozen, A.; İpek, O.; Garcia Castellanos, H.; Yurdakul, S.; Demiray, M.A.; Gürel, B.; Ozel, F.; Kurtuluş, K.; Kizilhan, H.; Keçebaş, A.; et al. Enhanced Triboelectric Nanogenerator Performance Using Torrefied Biowaste Dielectrics. *Adv. Eng. Mater.* **2026**, *28*, e202502668. [CrossRef]
30. Xia, X.; Fu, J.; Zi, Y. A Universal Standardized Method for Output Capability Assessment of Nanogenerators. *Nat. Commun.* **2019**, *10*, 4428. [CrossRef] [PubMed]
31. Baytekin, H.T.; Patashinski, A.Z.; Branicki, M.; Baytekin, B.; Soh, S.; Grzybowski, B.A. The Mosaic of Surface Charge in Contact Electrification. *Science* **2011**, *333*, 308–312. [CrossRef] [PubMed]
32. Lin, S.; Xu, C.; Xu, L.; Wang, Z.L. The Overlapped Electron-Cloud Model for Electron Transfer in Contact Electrification. *Adv. Funct. Mater.* **2020**, *30*, 1909724. [CrossRef]
33. Lin, S.; Xu, L.; Xu, C.; Chen, X.; Wang, A.C.; Zhang, B.; Lin, P.; Yang, Y.; Zhao, H.; Wang, Z.L. Electron Transfer in Nanoscale Contact Electrification: Effect of Temperature in the Metal–Dielectric Case. *Adv. Mater.* **2019**, *31*, 1808197. [CrossRef] [PubMed]
34. Gao, H.; Hu, M.; Ding, J.; Xia, B.; Yuan, G.; Sun, H.; Xu, Q.; Zhao, S.; Jiang, Y.; Wu, H.; et al. Investigation of Contact Electrification between 2D MXenes and MoS_2 through Density Functional Theory and Triboelectric Probes. *Adv. Funct. Mater.* **2023**, *33*, 2213410. [CrossRef]
35. Wang, H.; Huang, S.; Kuang, H.; Zhang, C.; Liu, Y.; Zhang, K.; Cai, X.; Wang, X.; Luo, J.; Wang, Z.L. A United Triboelectrification Mechanism for Contacts between All Types of Materials. *Adv. Energy Mater.* **2023**, *13*, 2300529. [CrossRef]

36. Ekim, S.D.; Yavuz, Z.; Çalışkan, T.D.; Güler, H.; Baytekin, H.T. The Dynamic Energy Band Model of Contact-Separation and Sliding Mode Triboelectric Charging of Polymers at the Metal-Polymer Interface. *Adv. Sci.* **2026**, *13*, e17094. [CrossRef] [PubMed]
37. Ma, X.; Zhou, J.; Kim, E.; Gao, J.; Hu, W.; Shin, D. Quantifying Electron and Ion Transfers in Contact Electrification with Ionomers. *Adv. Funct. Mater.* **2026**, *36*, e06471. [CrossRef]
38. Jiang, L.; Liu, X.; Lv, J.; Li, G.; Yang, P.; Ma, Y.; Zou, H.; Wang, Z.L. Fluid-Based Triboelectric Nanogenerators: Unveiling the Prolific Landscape of Renewable Energy Harvesting and Beyond. *Energy Environ. Sci.* **2024**, *17*, 3700–3738. [CrossRef]
39. Zhang, H.; Zhang, Y.; He, P.; Tian, X.; Jiang, L.; He, M.; Liu, X.; Chen, S.; Pang, D.; Kang, G.; et al. Quantifying the Triboelectric Series of Liquid Phase Materials. *Adv. Mater.* **2026**, *38*, e73450. [CrossRef] [PubMed]
40. Jiang, L.; Wang, Q.; Ou, J.; Lv, J.; Li, G.; Zhang, H.; Zhang, Y.; Liu, X.; Zheng, Y.; Li, Z.; et al. Mist Creates Giant Voltage: A Bio-Inspired, Self-Powered, and AI-Empowered Platform for Liquid Identification. *Device* **2026**, *4*, 101083. [CrossRef]
41. Tang, W.; Jiang, T.; Fan, F.R.; Yu, A.F.; Zhang, C.; Cao, X.; Wang, Z.L. Liquid-Metal Electrode for High-Performance Triboelectric Nanogenerator at an Instantaneous Energy Conversion Efficiency of 70.6%. *Adv. Funct. Mater.* **2015**, *25*, 3718–3725. [CrossRef]
42. Xie, Y.; Wang, S.; Niu, S.; Lin, L.; Jing, Q.; Yang, J.; Wu, Z.; Wang, Z.L. Grating-Structured Freestanding Triboelectric-Layer Nanogenerator for Harvesting Mechanical Energy at 85% Total Conversion Efficiency. *Adv. Mater.* **2014**, *26*, 6599–6607. [CrossRef] [PubMed]
43. Gong, S.; Li, K.; Sun, J.; Chen, J.; Guo, H. Three-Phase Interfacial Force Regulated Solid-Like Liquid-Slider for Highly Efficient and Robust Triboelectric Nanogenerator. *Adv. Mater.* **2026**, *38*, e16923. [CrossRef] [PubMed]
44. Chen, J.; Wang, Z.L. Reviving Vibration Energy Harvesting and Self-Powered Sensing by a Triboelectric Nanogenerator. *Joule* **2017**, *1*, 480–521. [CrossRef]
45. Choi, D.; Lee, Y.; Lin, Z.-H.; Cho, S.; Kim, M.; Ao, C.K.; Soh, S.; Sohn, C.; Jeong, C.K.; Lee, J.; et al. Recent Advances in Triboelectric Nanogenerators: From Technological Progress to Commercial Applications. *ACS Nano* **2023**, *17*, 11087–11219. [CrossRef] [PubMed]
46. Cheng, Y.; Liu, S.; Zhou, X.; Bai, J.; An, S.; Pu, X. Silicone-Based Triboelectric Pressure Sensor with Gradient Structures for Flexible Keyboard Music. *Adv. Funct. Mater.* **2025**, *35*, e10026. [CrossRef]
47. *JCGM 200:2012*; International Vocabulary of Metrology—Basic and General Concepts and Associated Terms (VIM), 3rd ed. BIPM: Sèvres, France, 2012.
48. *ISO 5725-1:2023*; Accuracy (Trueness and Precision) of Measurement Methods and Results—Part 1: General Principles and Definitions. International Organization for Standardization (ISO): Geneva, Switzerland, 2023.
49. Meng, Z.; Li, N.; Chen, X. Exploring Triboelectric Polymers: Strategies for Performance Optimization and Long-Term Stability. *Small Methods* **2025**, *9*, e01487. [CrossRef] [PubMed]
50. Joo, H.; Park, S.; Gwak, S.; Park, H.; Kim, S.; Lee, C.; Lee, W.; Lee, J. Polyelectrolytes as a Stable and Tunable Platform for Triboelectric Nanogenerators. *Adv. Mater.* **2025**, *37*, 2505547. [CrossRef] [PubMed]
51. Kundu, M.; Sarkar, M.; Lakshman, S.; Banerjee, S.; Hývl, M.; Ledinský, M.; Basu, R.; Bose, N.; Das, S. Improving the Performance of a Triboelectric Nanogenerator by Tuning the Work Function of a Surface Modified Tribonegative Polymer Composite. *Nanoscale* **2026**, *18*, 13532–13542. [CrossRef] [PubMed]
52. Khandelwal, G.; Maria Joseph Raj, N.P.; Kim, S. Zeolitic Imidazole Framework: Metal–Organic Framework Subfamily Members for Triboelectric Nanogenerators. *Adv. Funct. Mater.* **2020**, *30*, 1910162. [CrossRef]
53. Choi, G.-J.; Sohn, S.-H.; Kim, S.-J.; Park, I.-K. Polymer Composite-Based Triboelectric Nanogenerators: Recent Progress, Design Principles, and Future Perspectives. *Polymers* **2025**, *17*, 1962. [CrossRef] [PubMed]
54. Bhaduri, A.; Ha, T. Biowaste-Derived Triboelectric Nanogenerators for Emerging Bioelectronics. *Adv. Sci.* **2024**, *11*, 2405666. [CrossRef] [PubMed]
55. Luo, B.; Cai, C.; Liu, T.; Meng, X.; Zhuang, X.; Liu, Y.; Gao, C.; Chi, M.; Zhang, S.; Wang, J.; et al. Multiscale Structural Nanocellulosic Triboelectric Aerogels Induced by Hofmeister Effect. *Adv. Funct. Mater.* **2023**, *33*, 2306810. [CrossRef]
56. Brăileanu, P.I.; Pascu, N.E.; Dobrescu, T.G. Structure–Property Relationships and Surface Engineering of Natural Biopolymers for Triboelectric Applications: The Role of Additive Manufacturing. *Polymers* **2026**, *18*, 1260. [CrossRef] [PubMed]
57. Rodrigues-Marinho, T.; Pace, G.; Tubio, C.R.; Lanceros-Méndez, S.; Costa, P. Poly(Vinylidene Fluoride) Copolymers for Hybrid Piezoelectric and Triboelectric Energy Harvesting. *ACS Appl. Energy Mater.* **2024**, *7*, 10454–10465. [CrossRef]
58. Bindhu, A.; Arun, A.P.; Pathak, M. Review on Polyvinylidene Fluoride-Based Triboelectric Nanogenerators for Applications in Health Monitoring and Energy Harvesting. *ACS Appl. Electron. Mater.* **2024**, *6*, 47–72. [CrossRef]
59. Li, Y.; Luo, Y.; Deng, H.; Shi, S.; Tian, S.; Wu, H.; Tang, J.; Zhang, C.; Zhang, X.; Zha, J.; et al. Advanced Dielectric Materials for Triboelectric Nanogenerators: Principles, Methods, and Applications. *Adv. Mater.* **2024**, *36*, 2314380. [CrossRef] [PubMed]
60. Šutka, A.; Sherrell, P.C.; Shepelin, N.A.; Lapčinskis, L.; Mālnieks, K.; Ellis, A.V. Measuring Piezoelectric Output—Fact or Friction? *Adv. Mater.* **2020**, *32*, 2002979. [CrossRef] [PubMed]

61. Muñoz, I.; Quero, F.; Fernández-Gil, F.; Maureira, J.; Rosales-Cuello, N.; Palza, H. About the Relevance of Triboelectric Effects and Conductive Particles in Nanogenerators Based on Cellulose Materials and Their Composites. *Polymers* **2026**, *18*, 762. [CrossRef] [PubMed]
62. Liu, J.; Zhang, F.; Xu, J.; Jia, S.; Cui, N.; Yang, R.; Wang, W.; Gu, L. Unveiling the Synergistic Mechanism of C-F and C-Cl Bonds in Enhancing the Triboelectric Performance of Fluorinated Polymers. *Nat. Commun.* **2026**, *17*, 3698. [CrossRef] [PubMed]
63. Jella, V.; Ippili, S.; Yoon, S.-G. Dielectric Tailoring of Perovskite-Polymer Composites for High-Performance Triboelectric Nanogenerators. *Polymers* **2025**, *17*, 969. [CrossRef] [PubMed]
64. Madathil, N.; Potu, S.; Pani, J.; Bochu, L.; Babu, A.; Borkar, H.; Kodali, P.; Khanapuram, U.K.; Rajaboina, R.K. Enhancing Triboelectric Nanogenerators Performance with MXene–Silicone Nanocomposites: A Leap Forward in Energy Harvesting and Touch-Sensitive Technologies. *ACS Appl. Electron. Mater.* **2024**, *6*, 5563–5574. [CrossRef]
65. Manchi, P.; Paranjape, M.V.; Kurakula, A.; Graham, S.A.; Kavarthapu, V.S.; Yu, J.S. PDA-Ag/TiO_2 Nanoparticles-Loaded Electrospun Nylon Composite Nanofibrous Film-Based Triboelectric Nanogenerators for Wearable Biomechanical Energy Harvesting and Multifunctional Sensors. *Adv. Funct. Mater.* **2025**, *35*, 2416018. [CrossRef]
66. Li, H.; Zhang, T.; Zhao, H.; Kalimuldina, G.; Chen, L.; Sun, L.; Wen, Z.; Zhou, Y.; Chen, G.; Huang, H. Research Progress on Specialized Processing Technologies Enhancing Triboelectric Nanogenerators: Mechanisms, Performance and Applications. *Int. J. Extrem. Manuf.* **2026**, *8*, 062005. [CrossRef]
67. Meena, K.K.; Arief, I.; Ghosh, A.K.; Knapp, A.; Nitschke, M.; Fery, A.; Das, A. Transfer-Printed Wrinkled PVDF-Based Tactile Sensor-Nanogenerator Bundle for Hybrid Piezoelectric-Triboelectric Potential Generation. *Small* **2025**, *21*, 2502767. [CrossRef] [PubMed]
68. Liu, X.; Zhao, Z.; Zhang, B.; Hu, Y.; Qiao, W.; Gao, Y.; Wang, J.; Guo, Z.; Zhou, L.; Wang, Z.L.; et al. Superior Charge Density of Triboelectric Nanogenerator via Trap Engineering. *Adv. Funct. Mater.* **2025**, *35*, 2416944. [CrossRef]
69. Venkatesan, M.; Chandrasekar, J.; Hsu, Y.; Sun, T.; Li, P.; King, X.; Chung, M.; Chung, R.; Lee, W.; Zhou, Y.; et al. Rationally Improved Surface Charge Density of Triboelectric Nanogenerator with TiO_2-MXene/Polystyrene Nanofiber Charge Trapping Layer for Biomechanical Sensing and Wound Healing Application. *Adv. Sci.* **2024**, *11*, 2404019. [CrossRef] [PubMed]
70. Lim, D.U.; Lee, E.J.; Jang, J.K.; Kim, S.; Lee, S.Y.; Kim, T. Ion-Impregnated Intermediate Layer for Enhancing Triboelectric Nanogenerator Performance. *Adv. Funct. Mater.* **2024**, *34*, 2401717. [CrossRef]
71. Zhang, D.; Zhou, L.; Wu, Y.; Yang, C.; Zhang, H. Triboelectric Nanogenerator for Self-Powered Gas Sensing. *Small* **2024**, *20*, 2406964. [CrossRef] [PubMed]
72. Hou, Z.; Liu, T.; Li, M.; Xu, Y.; Wu, X.; Luo, S.; Cai, C.; Mou, Y.; Qiu, Y.; Nie, S.; et al. Superhydrophobic Triboelectric Structural Materials Enabled by Hierarchical Spatial Assembly. *Adv. Funct. Mater.* **2024**, *34*, 2400750. [CrossRef]
73. Mondal, A.; Faraz, M.; Dahiya, M.; Khare, N. Double-Layer Electronegative Structure-Based Triboelectric Nanogenerator for Enhanced Performance Using Combined Effect of Enhanced Charge Generation and Improved Charge Trapping. *ACS Appl. Mater. Interfaces* **2024**, *16*, 50659–50670. [CrossRef] [PubMed]
74. Huang, S.; Wang, W.; Yang, C.; Liu, J.; Li, K.; Zhou, L.; Zhang, H.; Zhang, D. Highly Stretchable Conductive Hydrogel-Based Flexible Triboelectric Nanogenerators for Ultrasensitive Tactile Sensing. *Polymers* **2025**, *17*, 342. [CrossRef] [PubMed]
75. Shen, Z.; Li, N.; Yi, J.; Xu, X.; Mo, X.; Wang, R. Toward Skin-like Sensors: Stretchable Conductive Gels for Triboelectric Applications. *Gels* **2026**, *12*, 151. [CrossRef] [PubMed]
76. Vaicekauskaite, J.; Mazurek, P.; Vudayagiri, S.; Skov, A.L. Mapping the Mechanical and Electrical Properties of Commercial Silicone Elastomer Formulations for Stretchable Transducers. *J. Mater. Chem. C* **2020**, *8*, 1273–1279. [CrossRef]
77. Song, S.; Drotlef, D.; Son, D.; Koivikko, A.; Sitti, M. Adaptive Self-Sealing Suction-Based Soft Robotic Gripper. *Adv. Sci.* **2021**, *8*, 2100641. [CrossRef] [PubMed]
78. Du, G.; Shao, Y.; Luo, B.; Liu, T.; Zhao, J.; Qin, Y.; Wang, J.; Zhang, S.; Chi, M.; Gao, C.; et al. Compliant Iontronic Triboelectric Gels with Phase-Locked Structure Enabled by Competitive Hydrogen Bonding. *Nano-Micro Lett.* **2024**, *16*, 170. [CrossRef] [PubMed]
79. Iqbal, S.; Muqeet Rehman, M.; Abbas, Z.; Sardar, S.A.; Saqib, M.; Yang, Y.; Kim, W.Y. High Performance Triboelectric Nanogenerator Based on Metal–Organic Framework Composites for IoT-Assisted Wireless Healthcare Monitoring. *Energy Environ. Mater.* **2025**, *8*, e70010. [CrossRef]
80. Oh, J.; Kang, M.; Park, J.; Kim, T.Y.; Park, K.; Seo, J. Autonomously Self-healing, Adhesive, and Stretchable Triboelectric Nanogenerator Using Multifunctional Hydrogel-Elastomer Double Layer with a Power Management Circuit. *Adv. Electron. Mater.* **2024**, *10*, 2400013. [CrossRef]
81. Kim, D.-W.; Mun, H.; Kang, Y.; Kim, W.-G.; Ahn, D.; Yun, S.-Y.; Han, J.-A.; Lee, D.H.; Lee, T.; Jeong, K.; et al. Synthesis of Stretchable Triboelectric Material with Strain-Compensating Ability Using Gradient Interpenetrating Polymer Networks. *Energy Environ. Sci.* **2025**, *18*, 4080–4096. [CrossRef]
82. Xu, S.; Fu, S.; Li, K.; Yi, H.; Wu, H.; Kang, Y.; Tao, X.; Wang, J.; Xi, Y.; Hu, C. Positive and Negative Triboelectricity Checkered Board Design for Friction Force and Heat Suppression in Triboelectrification Process. *Adv. Mater.* **2026**, *38*, e14573. [CrossRef] [PubMed]

83. Cao, M.; Chen, Y.; Sha, J.; Xu, Y.; Chen, S.; Xu, F. All-Cellulose Nanofiber-Based Sustainable Triboelectric Nanogenerators for Enhanced Energy Harvesting. *Polymers* **2024**, *16*, 1784. [CrossRef] [PubMed]
84. Yang, J.; Chang, L.; Deng, H.; Cao, Z. Zwitterionic Eutectogels with High Ionic Conductivity for Environmentally Tolerant and Self-Healing Triboelectric Nanogenerators. *ACS Nano* **2024**, *18*, 18980–18991. [CrossRef] [PubMed]
85. Sutradhar, S.C.; Banik, N.; Rahman Khan, M.M.; Jeong, J.-H. Polymer Gel-Based Triboelectric Nanogenerators: Conductivity and Morphology Engineering for Advanced Sensing Applications. *Gels* **2025**, *11*, 737. [CrossRef] [PubMed]
86. Zou, H.; Guo, L.; Xue, H.; Zhang, Y.; Shen, X.; Liu, X.; Wang, P.; He, X.; Dai, G.; Jiang, P.; et al. Quantifying and Understanding the Triboelectric Series of Inorganic Non-Metallic Materials. *Nat. Commun.* **2020**, *11*, 2093. [CrossRef] [PubMed]
87. Wang, Z.L. Triboelectric Nanogenerators as New Energy Technology for Self-Powered Systems and as Active Mechanical and Chemical Sensors. *ACS Nano* **2013**, *7*, 9533–9557. [CrossRef] [PubMed]
88. Wang, S.; Xie, Y.; Niu, S.; Lin, L.; Wang, Z.L. Freestanding Triboelectric-Layer-Based Nanogenerators for Harvesting Energy from a Moving Object or Human Motion in Contact and Non-contact Modes. *Adv. Mater.* **2014**, *26*, 2818–2824. [CrossRef] [PubMed]
89. Niu, S.; Wang, Z.L. Theoretical Systems of Triboelectric Nanogenerators. *Nano Energy* **2015**, *14*, 161–192. [CrossRef]
90. Chen, A.; Zeng, Q.; Tan, L.; Xu, F.; Wang, T.; Zhang, X.; Luo, Y.; Wang, X. A Novel Hybrid Triboelectric Nanogenerator Based on the Mutual Boosting Effect of Electrostatic Induction and Electrostatic Breakdown. *Energy Environ. Sci.* **2023**, *16*, 3486–3496. [CrossRef]
91. Li, Q.; Fu, S.; Li, X.; Chen, H.; He, W.; Yang, Q.; Zhang, X.; Yang, H.; Ren, D.; Xi, Y. Overall Performance Improvement of Direct-Current Triboelectric Nanogenerators by Charge Leakage and Ternary Dielectric Evaluation. *Energy Environ. Sci.* **2023**, *16*, 3514–3525. [CrossRef]
92. Xu, C.; Yu, J.; Huo, Z.; Wang, Y.; Sun, Q.; Wang, Z.L. Pursuing the Tribovoltaic Effect for Direct-Current Triboelectric Nanogenerators. *Energy Environ. Sci.* **2023**, *16*, 983–1006. [CrossRef]
93. Wang, Y.; Shi, L.; Zhong, M.; Tang, L.; Gan, W.C.; Zhu, Y.; Aw, K. Triboelectric Nanogenerator-Based Stretch Sensor. *Sensors* **2026**, *26*, 6493. [CrossRef] [PubMed]
94. Nie, C.; Lin, C.; Li, B.; Chen, F.; Guo, H.; Li, J.; Liang, L.; Wang, Y.; Wu, Y.; Zheng, H. A Novel E-Sticker Based on Triboelectric Nanogenerators for Wireless Passive Communication. *Adv. Funct. Mater.* **2025**, *35*, 2425965. [CrossRef]
95. Wang, W.; Zhu, J.; Zhao, H.; Yao, F.; Zhang, Y.; Qian, X.; Shu, M.; Wu, Z.; Xu, M.; Geng, H.; et al. A Reconfigurable Omnidirectional Triboelectric Whisker Sensor Array for Versatile Human–Machine–Environment Interaction. *Nano-Micro Lett.* **2026**, *18*, 76. [CrossRef] [PubMed]
96. Shen, F.; Zhang, Q.; Guo, H.; Cao, C.; Gong, Y.; Wang, J.; Peng, Y.; Li, Z. Investigation of Power Density Amplification in Stacked Triboelectric Nanogenerators. *Energy Environ. Mater.* **2024**, *7*, e12697. [CrossRef]
97. Park, Y.; Ro, Y.G.; Shin, Y.; Park, C.; Na, S.; Chang, Y.; Ko, H. Multi-Layered Triboelectric Nanogenerators with Controllable Multiple Spikes for Low-Power Artificial Synaptic Devices. *Adv. Sci.* **2023**, *10*, 2304598. [CrossRef] [PubMed]
98. Lei, H.; Ji, H.; Liu, X.; Lu, B.; Xie, L.; Lim, E.G.; Tu, X.; Liu, Y.; Zhang, P.; Zhao, C.; et al. Self-Assembled Porous-Reinforcement Microstructure-Based Flexible Triboelectric Patch for Remote Healthcare. *Nano-Micro Lett.* **2023**, *15*, 109. [CrossRef] [PubMed]
99. Meng, F.; Gao, Y.; Tao, Q.; Hu, J.; Yang, X. Braided Coaxial Two-Electrode Triboelectric Thread with a Mesh Spacer for Highly Sensitive Respiration Monitoring. *ACS Appl. Mater. Interfaces* **2025**, *17*, 20013–20021. [CrossRef] [PubMed]
100. Li, J.; Cai, J.; Yu, J.; Li, Z.; Ding, B. The Rising of Fiber Constructed Piezo/Triboelectric Nanogenerators: From Material Selections, Fabrication Techniques to Emerging Applications. *Adv. Funct. Mater.* **2023**, *33*, 2303249. [CrossRef]
101. Hussain, S.Z.; Singh, V.P.; Rahman, M.; Onuralp, D.B.; Ordu, M. Hybridized Piezoelectric–Triboelectric Effects for Self-Powered Sensing in Thermally Drawn Nanocomposite Fibers. *J. Mater. Chem. A* **2026**, *14*, 24420–24440. [CrossRef]
102. Si, J.; Yang, J.; Chen, Y.; Hu, N.; Yang, Y.; Wu, Y.; Huang, Q.; Han, L. An Integrated Temperature and Humidity Dual-Parameter Triboelectric Sensor. *J. Mater. Chem. C* **2024**, *12*, 11640–11647. [CrossRef]
103. *IEC 62830-7:2021*; Semiconductor Devices—Semiconductor Devices for Energy Harvesting and Generation—Part 7: Linear Sliding Mode Triboelectric Energy Harvesting. IEC: Geneva, Switzerland, 2021.
104. *IEC 62830-6:2019*; Semiconductor Devices—Semiconductor Devices for Energy Harvesting and Generation—Part 6: Test and Evaluation Methods for Vertical Contact Mode Triboelectric Energy Harvesting Devices. IEC: Geneva, Switzerland, 2019.
105. Zhang, H.; Li, H.; Li, Y. Biomimetic Electronic Skin for Robots Aiming at Superior Dynamic-Static Perception and Material Cognition Based on Triboelectric-Piezoresistive Effects. *Nano Lett.* **2024**, *24*, 4002–4011. [CrossRef] [PubMed]
106. Peng, W.; Zhu, R.; Ni, Q.; Zhao, J.; Zhu, X.; Mei, Q.; Zhang, C.; Liao, L. Functional Tactile Sensor Based on Arrayed Triboelectric Nanogenerators. *Adv. Energy Mater.* **2024**, *14*, 2403289. [CrossRef]
107. Johansson, R.S.; Vallbo, A.B. Detection of Tactile Stimuli. Thresholds of Afferent Units Related to Psychophysical Thresholds in the Human Hand. *J. Physiol.* **1979**, *297*, 405–422. [CrossRef] [PubMed]
108. Zhang, T.; Xu, X.; Li, X.; Yao, C.; Chen, J.; Li, M.; Tao, Y.; Xia, W.; Li, Y.; Wang, Y.; et al. Flexible Sensing Platform Based on Negative Pressure Triboelectric Nanogenerators and Microelectrode Array for Long-Term Synchronous Monitoring of Electrophysiological and Mechanical Beating in Cardiomyocytes. *ACS Sens.* **2025**, *10*, 4467–4479. [CrossRef] [PubMed]

109. Zhi, C.; Shi, S.; Wu, H.; Si, Y.; Zhang, S.; Lei, L.; Hu, J. Emerging Trends of Nanofibrous Piezoelectric and Triboelectric Applications: Mechanisms, Electroactive Materials, and Designed Architectures. *Adv. Mater.* **2024**, *36*, 2401264. [CrossRef] [PubMed]
110. Liu, J.; Wang, J.; Wang, Y.; Wu, Z.; Sun, H.; Yang, Y.; Zhang, L.; Kou, X.; Li, P.; Kang, W.; et al. A High-Performance Stretchable Triboelectric Nanogenerator Based on Polytetrafluoroethylene (PTFE) Particles. *Energy Environ. Mater.* **2025**, *8*, e12814. [CrossRef]
111. Khan, A.; Rashid, M.; Grabher, G.; Hossain, G. Autonomous Triboelectric Smart Textile Sensor for Vital Sign Monitoring. *ACS Appl. Mater. Interfaces* **2024**, *16*, 31807–31816. [CrossRef] [PubMed]
112. Ning, C.; Cheng, R.; Jiang, Y.; Sheng, F.; Yi, J.; Shen, S.; Zhang, Y.; Peng, X.; Dong, K.; Wang, Z.L. Helical Fiber Strain Sensors Based on Triboelectric Nanogenerators for Self-Powered Human Respiratory Monitoring. *ACS Nano* **2022**, *16*, 2811–2821. [CrossRef] [PubMed]
113. Ippili, S.; Jella, V.; Jyothi, S.J.; Kment, S.; Zboril, R.; Yoon, S.; Jayaramulu, K. Covalent Graphene-Metal–Organic Polyhedra Hybrids: Triboelectric Nanogenerators for Next Generation of Wearable E-Skin Technologies. *Small* **2025**, *21*, 2503772. [CrossRef] [PubMed]
114. Zhao, C.; Du, T.; Ge, B.; Xi, Z.; Qian, Z.; Wang, Y.; Wang, J.; Dong, F.; Shen, D.; Zhan, Z.; et al. Coaxial Flexible Fiber-Shaped Triboelectric Nanogenerator Assisted by Deep Learning for Self-Powered Vibration Monitoring. *Small* **2024**, *20*, 2307680. [CrossRef] [PubMed]
115. Peng, H.; Wu, Y.; Li, Y.; He, Y.; Wang, C.; Na, X.; Tan, Q.; Qiu, W.; Yang, X. Magnetically Repulsive Cushion Triboelectric Nanogenerator for Rotating Machinery Structural Health Monitoring. *Sensors* **2026**, *26*, 3587. [CrossRef] [PubMed]
116. Wu, P.; Wang, F.; Xu, S.; Liu, T.; Qi, Y.; Zhao, X.; Zhang, C.; Mu, X. A Highly Sensitive Triboelectric Quasi-Zero Stiffness Vibration Sensor with Ultrawide Frequency Response. *Adv. Sci.* **2023**, *10*, 2301199. [CrossRef] [PubMed]
117. Gao, M.; Yang, Z.; Pang, Y.; Dai, G.; Lee, C.; Choi, J.; Yang, J. Triboelectric Nanogenerators for Condition Monitoring of Machines, Infrastructure and Environment. *Interdiscip. Mater.* **2025**, *4*, 645–685. [CrossRef]
118. Chen, Q.; Cao, Y.; Lu, Y.; Akram, W.; Ren, S.; Niu, L.; Sun, Z.; Fang, J. Hybrid Piezoelectric/Triboelectric Wearable Nanogenerator Based on Stretchable PVDF–PDMS Composite Films. *ACS Appl. Mater. Interfaces* **2024**, *16*, 6239–6249. [CrossRef] [PubMed]
119. Chen, J.; Shen, C.; Yao, C.; Wang, X.; Wang, S.; Chen, Z.; Zhang, M.; Gan, J.; Zhao, X. Enriching Triboelectric Signal Waveform Characteristics Based on Complex Interface Structure for Monitoring Device Operating Status. *Small* **2026**, *22*, e11248. [CrossRef] [PubMed]
120. Peng, W.; Zhang, Y.; Zhang, Z.; Zhao, H.; Huang, H.; Zhao, J.; Cheng, B.-X.; He, J.; Xu, B.; Shang, B.; et al. Liquid Metal-Promoted Supramolecular Interactions Enable Ultrafast Self-Healing Triboelectric Materials with High Performance at Room Temperature. *Nano Lett.* **2025**, *25*, 6622–6630. [CrossRef] [PubMed]
121. So, M.Y.; Xu, B. Adaptive Ultra-Low Resilience Woven Triboelectric Nanogenerators for High-Performance Wearable Energy Harvesting and Motion Sensing. *Small* **2025**, *21*, 2501116. [CrossRef] [PubMed]
122. Shen, Y.; Jiang, Z.; Huang, H.; Wang, S.; Wu, S.; Wang, J.; Sun, X.; Liu, Y.; Wen, Z. Advances in Textile-Based Triboelectric Sensors for Physiological Signal Monitoring. *Adv. Funct. Mater.* **2025**, *35*, 2426081. [CrossRef]
123. Han, D.; Kim, K.; Shin, J.; Park, J. Gesture-Based Secure Authentication System Using Triboelectric Nanogenerator Sensors. *Sensors* **2025**, *25*, 5170. [CrossRef] [PubMed]
124. Gong, H.; Luo, S.; Shan, P. Low-Cost Spray-Patterned Triboelectric Textiles for Wearable Interaction and Energy Harvesting. *Sensors* **2026**, *26*, 5554. [CrossRef] [PubMed]
125. Yao, C.; Liu, S.; Xu, X.; Yun, P.; Zhang, T.; Sun, T.; He, M.; Liang, B.; Li, M.; Huang, S.; et al. Long-Term Used Continuous Blood Pressure Monitoring via Personalized Object Transfer Learning Architecture Enhanced Triboelectric Pulse Sensors. *Adv. Funct. Mater.* **2025**, *35*, 2418318. [CrossRef]
126. Zou, M.; Deng, L.; Deng, Y.; Lu, Y.; Gao, H.; Xu, F.; Li, M.; Guo, H.; Lin, Z. Octopus-Inspired High-Sensitivity Triboelectric Sensor for Epidermal Pulse Monitoring and Cardiovascular Assessment. *Nanoscale* **2025**, *17*, 27881–27889. [CrossRef] [PubMed]
127. Wang, C.; He, Y.; Peng, H.; Luo, H.; Wang, X. A Flexible Triboelectric-Based Sensor for Seismocardiography Monitoring. *Biosensors* **2026**, *16*, 260. [CrossRef] [PubMed]
128. Shi, A.; Luo, B.; Liu, W.; Chen, W.; Li, Z.; Wang, S.; Jiang, L.; Zhang, H.; Qin, X.; Sun, W. A Facile Strategy for Textile-Based Highly Sensitive and Water-Resistant Triboelectric Nanogenerator. *Adv. Mater.* **2025**, *37*, 2420459. [CrossRef] [PubMed]
129. *ISO 81060-2:2018*; Non-Invasive Sphygmomanometers—Part 2: Clinical Validation of Intermittent Automated Measurement Type. International Organization for Standardization (ISO): Geneva, Switzerland, 2018.
130. *IEEE 1708-2014*; Standard for Wearable Cuffless Blood Pressure Measuring Devices. IEEE: Piscataway, NJ, USA, 2014.
131. *ISO 81060-3:2022*; Non-Invasive Sphygmomanometers—Part 3: Clinical Investigation of Continuous Automated Measurement Type. International Organization for Standardization (ISO): Geneva, Switzerland, 2022.
132. Chen, X.; Peng, X.; Wei, C.; Wang, Z.; He, J.; Sheng, H.; Jiang, T.; Dong, K. A Moisture-Proof, Anti-Fouling, and Low Signal Attenuation All-Nanofiber Triboelectric Sensor for Self-Powered Respiratory Health Monitoring. *Adv. Funct. Mater.* **2025**, *35*, 2415421. [CrossRef]
133. Xu, H.; Han, W.; Yuce, M.R. A Wearable Device with Triboelectric Nanogenerator Sensing for Respiration and Spirometry Monitoring. *ACS Sens.* **2025**, *10*, 264–271. [CrossRef] [PubMed]

134. Choi, K.; Park, J.; Song, W.J.; An, S.; Choe, S.; Keum, B.; Kim, M.Y.; Hwang, D.H.; Park, Y.; Kim, S.; et al. Soft Ionic and Electronic Triboelectric Nanogenerators: Toward Attachable and Implantable Biomedical Applications. *Adv. Mater.* **2026**, *38*, e17321. [CrossRef] [PubMed]
135. Vera Anaya, D.; Yuce, M.R. Stretchable Triboelectric Sensor for Measurement of the Forearm Muscles Movements and Fingers Motion for Parkinson's Disease Assessment and Assisting Technologies. *Med. Devices Sens.* **2021**, *4*, e10154. [CrossRef]
136. Huang, S.; Hou, A.; Murti, B.T.; Chen, C.; Hsu, C.; Ha, I.; Luo, K.; Chao, Y.; Ni, I.; Kang, C.; et al. Deformation-Adaptive Hybrid Triboelectric–Piezoelectric Nanogenerator for Wearable Muscle Monitoring and Human–Machine Interaction. *Small* **2026**, *22*, e75415. [CrossRef] [PubMed]
137. Sheng, F.; Zhang, B.; Zhang, Y.; Li, Y.; Cheng, R.; Wei, C.; Ning, C.; Dong, K.; Wang, Z.L. Ultrastretchable Organogel/Silicone Fiber-Helical Sensors for Self-Powered Implantable Ligament Strain Monitoring. *ACS Nano* **2022**, *16*, 10958–10967. [CrossRef] [PubMed]
138. Shen, J.; Yang, Y.; Zhang, J.; Lin, W.; Gu, H. Carbon Quantum Dot-Functionalized Dermis-Derived Transparent Electronic Skin for Multimodal Human Motion Signal Monitoring and Construction of Self-Powered Triboelectric Nanogenerator. *ACS Appl. Mater. Interfaces* **2024**, *16*, 46771–46788. [CrossRef] [PubMed]
139. Chang, Y.; Wang, L.; Li, R.; Zhang, Z.; Wang, Q.; Yang, J.; Guo, C.F.; Pan, T. First Decade of Interfacial Iontronic Sensing: From Droplet Sensors to Artificial Skins. *Adv. Mater.* **2021**, *33*, 2003464. [CrossRef] [PubMed]
140. Ro, Y.G.; Na, S.; Kim, J.; Chang, Y.; Lee, S.; Kwak, M.S.; Jung, S.; Ko, H. Iontronics: Neuromorphic Sensing and Energy Harvesting. *ACS Nano* **2025**, *19*, 24425–24507. [CrossRef] [PubMed]
141. Xu, G.; Huang, X.; Shi, R.; Yang, Y.; Wu, P.; Zhou, J.; He, X.; Li, J.; Zen, Y.; Jiao, Y.; et al. Triboelectric Nanogenerator Enabled Sweat Extraction and Power Activation for Sweat Monitoring. *Adv. Funct. Mater.* **2024**, *34*, 2310777. [CrossRef]
142. Gao, N.; Xu, G.; Chang, G.; Wu, Y. From Lab to Life: Self-Powered Sweat Sensors and Their Future in Personal Health Monitoring. *Adv. Sci.* **2025**, *12*, 2409178. [CrossRef] [PubMed]
143. Ali, I.; Karim, N.; Afroj, S. Textile-based Triboelectric Nanogenerators Integrated with 2D Materials. *EcoMat* **2024**, *6*, e12471. [CrossRef]
144. Das, J.P.; Nardekar, S.S.; Ravichandran, V.; Kim, S. From Friction to Function: A High-Voltage Sliding Triboelectric Nanogenerator for Highly Efficient Energy Autonomous IoTs and Self-Powered Actuation. *Small* **2024**, *20*, 2405792. [CrossRef] [PubMed]
145. Parashar, P.; Sharma, M.K.; Nahak, B.K.; Khan, A.; Hsu, W.-Z.; Tseng, Y.-H.; Chowdhury, J.R.; Huang, Y.-H.; Liao, J.-C.; Kao, F.-C.; et al. Machine Learning-Driven Gait-Assisted Self-Powered Wearable Sensing: A Triboelectric Nanogenerator-Based Advanced Healthcare Monitoring. *J. Mater. Chem. A* **2025**, *13*, 13750–13762. [CrossRef]
146. Chen, P.; Wang, R.; Schmuck, E.; Wang, D.; Modaff, D.; Zhou, T.; Osaki, S.; Liu, W.; Pan, F.; Kim, J.-K.; et al. Self-Sustaining Leadless Intracardiac Pacemaker Powered by Triboelectric Nanogenerator. *Sci. Adv.* **2026**, *12*, eaef8903. [CrossRef] [PubMed]
147. Zhu, Q.; Wu, T.; Sun, Y.; Yang, P.; Zhang, L.; Xin, Y.; Cao, X.; Wang, N. Bioinspired Janus Spider-Web Nanofibrous Membranes Integrating Triboelectric Energy Harvesting, Adaptive Thermo-Moisture Regulation, and Bactericidal Activity for Multifunctional Wearables. *Adv. Mater.* **2026**, *38*, e16022. [CrossRef] [PubMed]
148. Zhang, B.; Shen, A.; Jing, Y.; Zhang, S.; Jiang, Y.; Li, R.; Wang, R.; Chen, B.; Cai, Y.; Mao, Y. Flexible Nanostructured Polymer Materials Based Triboelectric Nanogenerators for Self-Powered Environmental Sensing. *Small Methods* **2025**, *9*, e01241. [CrossRef] [PubMed]
149. Arjun, A.M.; Ankitha, M.; Mathew, M.; Sharma, S.; Rasheed, P.A. Recent Advances in MXene-Based Self-Powered Electrochemical Sensors. *J. Mater. Chem. A* **2026**, *14*, 1450–1467. [CrossRef]
150. Li, Y.; Deng, H.; Wu, H.; Luo, Y.; Deng, Y.; Yuan, H.; Cui, Z.; Tang, J.; Xiong, J.; Zhang, X.; et al. Rotary Wind-driven Triboelectric Nanogenerator for Self-Powered Airflow Temperature Monitoring of Industrial Equipment. *Adv. Sci.* **2024**, *11*, 2307382. [CrossRef] [PubMed]
151. Heo, D.; Hur, J.; Cho, H.; Cha, K.; Choi, J.; Choi, M.; Hong, J.; Kim, S.; Lee, S. Nano-Oil-Barrier-Based Fluttering Triboelectric Nanogenerator. *Adv. Sci.* **2025**, *12*, e02278. [CrossRef] [PubMed]
152. Wang, Z.; Wang, K.; Liu, Y.; Guan, X.; Pan, Z.; Yao, Y.; Li, T. Triboelectric Sensor with a Hierarchical Structure for Omnidirectional Adaptive Wind Speed and Wind Direction Sensing for Unmanned Aerial Vehicles. *ACS Appl. Mater. Interfaces* **2025**, *17*, 23984–23995. [CrossRef] [PubMed]
153. Xu, W.; Zheng, H.; Liu, Y.; Zhou, X.; Zhang, C.; Song, Y.; Deng, X.; Leung, M.; Yang, Z.; Xu, R.X.; et al. A Droplet-Based Electricity Generator with High Instantaneous Power Density. *Nature* **2020**, *578*, 392–396. [CrossRef] [PubMed]
154. Min, G.; Wang, W.; Li, H.; Wang, T.; Li, C.; Xu, S.; Xu, K.; Shang, Y.; Zhao, X.; Khandelwal, G.; et al. Optimizing Droplet-Based Electricity Generator via a Low Sticky Hydrophobic Droplet-Impacted Surface. *Small* **2024**, *20*, 2402765. [CrossRef] [PubMed]
155. Begum, S.R.; Chandrasekhar, A. Biomimicking Hydrophobic Leaf Structure Using Soft Lithography for Fog Harvesting, Triboelectric Nanogenerators as a Self-Powered Rain Sensor. *iScience* **2024**, *27*, 108878. [CrossRef] [PubMed]
156. Shan, C.; He, W.; Wu, H.; Fu, S.; Li, K.; Liu, A.; Du, Y.; Wang, J.; Mu, Q.; Liu, B.; et al. Dual Mode TENG with Self-Voltage Multiplying Circuit for Blue Energy Harvesting and Water Wave Monitoring. *Adv. Funct. Mater.* **2023**, *33*, 2305768. [CrossRef]

157. Liu, C.; Wang, Z.; Tong, X.; Wu, Z.; Zhou, L.; Zou, H.; Ogunjuyibe, A.; Lin, H.; Yan, D.; Yang, W.; et al. Water-Evaporation-Induced Direct Current Electricity Generation Based on Stretchable Hydrogel/Al_2O_3. *Matter* **2025**, *8*, 102200. [CrossRef]
158. Li, F.; Sun, S.; Wan, X.; Sun, M.; Zhang, S.L.; Xu, M. A Self-Powered Soft Triboelectric-Electrohydrodynamic Pump. *Nat. Commun.* **2025**, *16*, 1315. [CrossRef] [PubMed]
159. Nie, J.; Wang, Z.; Ren, Z.; Li, S.; Chen, X.; Lin Wang, Z. Power Generation from the Interaction of a Liquid Droplet and a Liquid Membrane. *Nat. Commun.* **2019**, *10*, 2264. [CrossRef] [PubMed]
160. Lu, Y.; Jiang, L.; Yu, Y.; Wang, D.; Sun, W.; Liu, Y.; Yu, J.; Zhang, J.; Wang, K.; Hu, H.; et al. Liquid-Liquid Triboelectric Nanogenerator Based on the Immiscible Interface of an Aqueous Two-Phase System. *Nat. Commun.* **2022**, *13*, 5316. [CrossRef] [PubMed]
161. Zhang, R.; Lin, H.; Pan, Y.; Li, C.; Yang, Z.; Tian, J.; Shum, H.C. Liquid–Liquid Triboelectric Nanogenerator for Harvesting Distributed Energy. *Adv. Funct. Mater.* **2022**, *32*, 2208393. [CrossRef]
162. Yang, Y.; Akhtar, F.; Iqbal, S.; Rehman, M.M.; Kim, W.Y. Sustainable Triboelectric Nanogenerator from Abalone Shell Powder for Self-Powered Humidity Sensing. *Sensors* **2025**, *25*, 7584. [CrossRef] [PubMed]
163. Zhang, M.; Zhang, B.; Li, Z.; Zhang, J.; Luo, Y.; Yue, Z. A Swirling-Flow-Enhanced Triboelectric Nanogenerator for Improved Dilute-Phase Particle Sensing. *Sensors* **2026**, *26*, 2284. [CrossRef] [PubMed]
164. Gungordu Er, S.; Bulathsinghala, R.; Kizilates, S.B.; Li, B.; Ryan, R.; Tabish, T.A.; Dharmasena, I.; Edirisinghe, M. Multifunctional Conductive Nanofibers for Self-Powered Glucose Biosensors. *Adv. Sci.* **2025**, *12*, 2416320. [CrossRef] [PubMed]
165. Liu, W.; Li, H.; Gao, Q.; Zhao, D.; Yu, Y.; Xiang, Q.; Cheng, X.; Wang, Z.L.; Long, W.; Cheng, T. Micro-Droplets Parameters Monitoring in a Microfluidic Chip via Liquid-Solid Triboelectric Nanogenerator. *Adv. Mater.* **2023**, *35*, 2307184. [CrossRef] [PubMed]
166. Zhou, J.; Tao, Y.; Xue, R.; Ren, Y. A Self-Powered Dielectrophoretic Microparticle Manipulation Platform Based on a Triboelectric Nanogenerator. *Adv. Mater.* **2023**, *35*, 2207093. [CrossRef] [PubMed]
167. Zhou, B.; Liu, J.; Huang, X.; Qiu, X.; Yang, X.; Shao, H.; Tang, C.; Zhang, X. Mechanoluminescent-Triboelectric Bimodal Sensors for Self-Powered Sensing and Intelligent Control. *Nano-Micro Lett.* **2023**, *15*, 72. [CrossRef] [PubMed]
168. Wu, J.; Zhou, X.; Luo, J.; Zhou, J.; Lu, Z.; Bai, Z.; Fan, Y.; Chen, X.; Zheng, B.; Wang, Z.; et al. Stretchable and Self-Powered Mechanoluminescent Triboelectric Nanogenerator Fibers toward Wearable Amphibious Electro-Optical Sensor Textiles. *Adv. Sci.* **2024**, *11*, 2401109. [CrossRef] [PubMed]
169. Pan, X.; Zhuang, Y.; He, W.; Lin, C.; Mei, L.; Chen, C.; Xue, H.; Sun, Z.; Wang, C.; Peng, D.; et al. Quantifying the Interfacial Triboelectricity in Inorganic-Organic Composite Mechanoluminescent Materials. *Nat. Commun.* **2024**, *15*, 2673. [CrossRef] [PubMed]
170. Zhao, J.; Shi, Y. Boosting the Durability of Triboelectric Nanogenerators: A Critical Review and Prospect. *Adv. Funct. Mater.* **2023**, *33*, 2213407. [CrossRef]
171. Efimenko, K.; Wallace, W.E.; Genzer, J. Surface Modification of Sylgard-184 Poly(Dimethyl Siloxane) Networks by Ultraviolet and Ultraviolet/Ozone Treatment. *J. Colloid Interface Sci.* **2002**, *254*, 306–315. [CrossRef] [PubMed]
172. Ahmad, Z.; Parias M. R, B.; Barr, H.; Cabral, J.T. Thermal Conduction Suppresses Cracks in PDMS Wrinkling by Plasma Oxidation. *Nano Lett.* **2025**, *25*, 740–746. [CrossRef] [PubMed]
173. Cheng, B.; Xu, Q.; Ding, Y.; Bai, S.; Jia, X.; Yu, Y.; Wen, J.; Qin, Y. High Performance Temperature Difference Triboelectric Nanogenerator. *Nat. Commun.* **2021**, *12*, 4782. [CrossRef] [PubMed]
174. Tao, X.; Li, S.; Shi, Y.; Wang, X.; Tian, J.; Liu, Z.; Yang, P.; Chen, X.; Wang, Z.L. Triboelectric Polymer with High Thermal Charge Stability for Harvesting Energy from 200 °C Flowing Air. *Adv. Funct. Mater.* **2021**, *31*, 2106082. [CrossRef]
175. Cao, R.; Liu, Y.; Li, H.; Shen, Z.; Li, F.; Jia, X.; Chen, C.; Liu, R.; Luo, C.; Yang, W.; et al. Advances in High-temperature Operatable Triboelectric Nanogenerator. *SusMat* **2024**, *4*, e196. [CrossRef]
176. Jung, J.J.; Jin, H.S.; Kim, K.H.; Choi, J.; Han, J.H.; Lee, H.E.; Jeong, C.K. Recent Physicochemical Surface Modification Approaches to Enhance Triboelectric Nanogenerator Performance: Materials, Processing and Applications. *Nanoscale* **2026**, *18*, 4552–4567. [CrossRef] [PubMed]
177. Zhang, J.; Boyer, C.; Zhang, Y.X. Enhancing the Humidity Resistance of Triboelectric Nanogenerators: A Review. *Small* **2024**, *20*, 2401846. [CrossRef] [PubMed]
178. Liu, T.; Liang, R.; He, H.; Cui, X.; Li, X.; Yu, K.; Ye, Z.; Chi, M.; Cai, C.; Zhang, S.; et al. High-Temperature Wireless Triboelectric Sensor Fabricated from Bioinspired Porous Materials. *Adv. Funct. Mater.* **2026**, *36*, e18525. [CrossRef]
179. Weldemhret, T.G.; Debele, N.T.; Kedir, S.N.; Reda, A.T.; Kim, D.; Chung, K.; Park, Y.T. Thermally Stable and Shape-Adaptive Triboelectric Nanogenerators Based on Liquid Electrolytes with Low Vapor Pressure. *Small* **2025**, *21*, 2500318. [CrossRef] [PubMed]
180. Wang, N.; Zheng, Y.; Feng, Y.; Zhou, F.; Wang, D. Biofilm Material Based Triboelectric Nanogenerator with High Output Performance in 95% Humidity Environment. *Nano Energy* **2020**, *77*, 105088. [CrossRef]

181. Sun, Q.; Ren, G.; He, S.; Tang, B.; Li, Y.; Wei, Y.; Shi, X.; Tan, S.; Yan, R.; Wang, K.; et al. Charge Dispersion Strategy for High-Performance and Rain-Proof Triboelectric Nanogenerator. *Adv. Mater.* **2024**, *36*, 2307918. [CrossRef] [PubMed]
182. Cheng, T.; Lian, W.; Zhang, W.; Wang, J.; Wu, C.; Lu, B.; Tan, K.; Dong, B.; Liu, C.; Shen, C. Room-Temperature Self-Repairable Yet Mechanically Robust Elastomeric Triboelectric Nanogenerators Enabled by a Fast-Reversible Dual-Dynamic Network. *ACS Sustain. Chem. Eng.* **2023**, *11*, 14376–14390. [CrossRef]
183. Huang, H.-X.; Yang, F.; Huang, L.-Q.; Xu, H.; Yu, N.; Zhang, J.-L.; Li, P.; Jiang, Y.; Wang, S.-F.; Ren, X.-M.; et al. A Tough Polyurethane with Self-Healing Ability for Wearable Triboelectric Nanogenerator Devices. *ACS Appl. Mater. Interfaces* **2025**, *17*, 12621–12630. [CrossRef] [PubMed]
184. Yu, N.; Cheng, B.; Liu, Y.; Wu, W.; Li, R.K.Y.; Liang, Z.; Cheng, F.; Zhao, H. High-Strength and High-Toughness Supramolecular Materials for Self-Healing Triboelectric Nanogenerator. *Small* **2024**, *20*, 2405700. [CrossRef] [PubMed]
185. Li, G.; Li, Z.; Hu, H.; Chen, B.; Wang, Y.; Mao, Y.; Li, H.; Zhang, B. Recent Progress in Self-Healing Triboelectric Nanogenerators for Artificial Skins. *Biosensors* **2025**, *15*, 37. [CrossRef] [PubMed]
186. JEDEC Solid State Technology Association. *Steady-State Temperature-Humidity Bias Life Test*; JEDEC Solid State Technology Association: Arlington, VA, USA, 2021.
187. Wang, H.; Yin, Y.; Su, Z.; Chen, C.; Zhang, L.; Wang, C.; Yang, W.; Huang, Y.; Xu, P.; Ma, P.; et al. Bio-Based and Recyclable Self-Healing Elastomer for the Application of Self-Powered Triboelectric Nanogenerator in Low-Temperature. *Adv. Funct. Mater.* **2024**, *34*, 2311649. [CrossRef]
188. Wang, H.; Xu, D.; Zhang, Y.; Yang, W.; Xu, P.; Niu, D.; Chen, C.; Ma, P.; Ma, P. Biobased Polyurethane Materials with Self-Healing and Recycling Capabilities for Sustainable Applications in Triboelectric Devices. *ACS Sustain. Chem. Eng.* **2025**, *13*, 8904–8916. [CrossRef]
189. Hao, Y.; Zhang, C.; Su, W.; Zhang, H.; Qin, Y.; Wang, Z.L.; Li, X. Sustainable Materials Systems for Triboelectric Nanogenerator. *SusMat* **2024**, *4*, e244. [CrossRef]
190. Brazma, A.; Hingamp, P.; Quackenbush, J.; Sherlock, G.; Spellman, P.; Stoeckert, C.; Aach, J.; Ansorge, W.; Ball, C.A.; Causton, H.C.; et al. Minimum Information about a Microarray Experiment (MIAME)—Toward Standards for Microarray Data. *Nat. Genet.* **2001**, *29*, 365–371. [CrossRef] [PubMed]
191. Taylor, C.F.; Paton, N.W.; Lilley, K.S.; Binz, P.-A.; Julian, R.K.; Jones, A.R.; Zhu, W.; Apweiler, R.; Aebersold, R.; Deutsch, E.W.; et al. The Minimum Information about a Proteomics Experiment (MIAPE). *Nat. Biotechnol.* **2007**, *25*, 887–893. [CrossRef] [PubMed]
192. *ISO 25178-2:2021*; Geometrical Product Specifications (GPS)—Surface Texture: Areal—Part 2: Terms, Definitions and Surface Texture Parameters. International Organization for Standardization (ISO): Geneva, Switzerland, 2021.
193. *JCGM 100:2008*; Evaluation of Measurement Data—Guide to the Expression of Uncertainty in Measurement. BIPM: Sèvres, France, 2008.
194. *ISO 5725-2:2019*; Accuracy (Trueness and Precision) of Measurement Methods and Results—Part 2: Basic Method for the Determination of Repeatability and Reproducibility of a Standard Measurement Method. International Organization for Standardization (ISO): Geneva, Switzerland, 2019.
195. *ISO 13528:2022*; Statistical Methods for Use in Proficiency Testing by Interlaboratory Comparison. International Organization for Standardization (ISO): Geneva, Switzerland, 2022.
196. Zhang, R. Machine Learning-Assisted Triboelectric Nanogenerator-Based Self-Powered Sensors. *Cell Rep. Phys. Sci.* **2024**, *5*, 101888. [CrossRef]
197. Wilkinson, M.D.; Dumontier, M.; Aalbersberg, I.J.J.; Appleton, G.; Axton, M.; Baak, A.; Blomberg, N.; Boiten, J.-W.; Da Silva Santos, L.B.; Bourne, P.E.; et al. The FAIR Guiding Principles for Scientific Data Management and Stewardship. *Sci. Data* **2016**, *3*, 160018. [CrossRef] [PubMed]
198. Li, Z.; Yu, A.; Zhai, J.; Wang, Z.L. Sustainable Biopolymers in Eco-Friendly Triboelectric Energy Harvesting. *Adv. Mater.* **2025**, *37*, 2412671. [CrossRef] [PubMed]
199. Ahmed, A.; Hassan, I.; Ibn-Mohammed, T.; Mostafa, H.; Reaney, I.M.; Koh, L.S.C.; Zu, J.; Wang, Z.L. Environmental Life Cycle Assessment and Techno-Economic Analysis of Triboelectric Nanogenerators. *Energy Environ. Sci.* **2017**, *10*, 653–671. [CrossRef]
200. European Chemicals Agency. *Annex XV Restriction Report—Proposal for a Restriction on Per- and Polyfluoroalkyl Substances (PFASs)*; European Chemicals Agency (ECHA): Helsinki, Finland, 2023.
201. Xu, G.; Li, X.; Fu, J.; Zhou, Y.; Xia, X.; Zi, Y. Environmental Lifecycle Assessment of CO_2-Filled Triboelectric Nanogenerators to Help Achieve Carbon Neutrality. *Energy Environ. Sci.* **2023**, *16*, 2112–2119. [CrossRef]
202. Luo, Z.; Xia, X.; Zi, Y. Environmental Life Cycle Assessment of Self-Powered Wireless Sensing E-Sticker Based Devices. *SmartSys* **2026**, *2*, e70027. [CrossRef]
203. Kim, H.-J.; Yim, E.-C.; Kim, J.-H.; Kim, S.-J.; Park, J.-Y.; Oh, I.-K. Bacterial Nano-Cellulose Triboelectric Nanogenerator. *Nano Energy* **2017**, *33*, 130–137. [CrossRef]
204. Wang, R.; Gao, S.; Yang, Z.; Li, Y.; Chen, W.; Wu, B.; Wu, W. Engineered and Laser-Processed Chitosan Biopolymers for Sustainable and Biodegradable Triboelectric Power Generation. *Adv. Mater.* **2018**, *30*, 1706267. [CrossRef] [PubMed]

205. Ma, C.; Gao, S.; Gao, X.; Wu, M.; Wang, R.; Wang, Y.; Tang, Z.; Fan, F.; Wu, W.; Wan, H.; et al. Chitosan Biopolymer-derived Self-powered Triboelectric Sensor with Optimized Performance through Molecular Surface Engineering and Data-driven Learning. *InfoMat* **2019**, *1*, 116–125. [CrossRef]
206. Araújo, F.; Magalhães, S.; Medronho, B.; Eivazi, A.; Dahlström, C.; Norgren, M.; Alves, L. Effect of Chitosan Properties and Dissolution State on Solution Rheology and Film Performance in Triboelectric Nanogenerators. *Gels* **2025**, *11*, 523. [CrossRef] [PubMed]
207. He, J.; Wang, L.; Zheng, K.; Hu, S.; Zhang, X.; Mu, Z. Coordination of Mg2+ with Chitosan for Enhanced Triboelectric Performance. *Polymers* **2025**, *17*, 1001. [CrossRef] [PubMed]
208. Gao, C.; Tong, W.; Zhang, B.; Zhang, Y. Dual Effects of Green Plasticizers on the Mechanical and Output Properties of Chitosan–Based Triboelectric Nanogenerators. *Nano Energy* **2025**, *142*, 111171. [CrossRef]
209. Xu, Z.; Qiu, W.; Fan, X.; Shi, Y.; Gong, H.; Huang, J.; Patil, A.; Li, X.; Wang, S.; Lin, H.; et al. Stretchable, Stable, and Degradable Silk Fibroin Enabled by Mesoscopic Doping for Finger Motion Triggered Color/Transmittance Adjustment. *ACS Nano* **2021**, *15*, 12429–12437. [CrossRef] [PubMed]
210. Tan, X.; Wang, S.; You, Z.; Zheng, J.; Liu, Y. High Performance Porous Triboelectric Nanogenerator Based on Silk Fibroin@MXene Composite Aerogel and PDMS Sponge. *ACS Mater. Lett.* **2023**, *5*, 1929–1937. [CrossRef]
211. Pan, R.; Xuan, W.; Chen, J.; Dong, S.; Jin, H.; Wang, X.; Li, H.; Luo, J. Fully Biodegradable Triboelectric Nanogenerators Based on Electrospun Polylactic Acid and Nanostructured Gelatin Films. *Nano Energy* **2018**, *45*, 193–202. [CrossRef]
212. Lapčinskis, L.; Ģērmane, L.; Platnieks, O.; Krikovs, A.; Gaidukovs, S.; Pudzs, K.; Linarts, A.; Sherrell, P.C.; Šutka, A. High Performance Triboelectric Nanogenerators from Compostable Cellulose-Biodegradable Poly(Butylene Succinate) Composites. *Adv. Sustain. Syst.* **2023**, *7*, 2300280. [CrossRef]
213. Kang, M.; Lee, D.-M.; Hyun, I.; Rubab, N.; Kim, S.-H.; Kim, S.-W. Advances in Bioresorbable Triboelectric Nanogenerators. *Chem. Rev.* **2023**, *123*, 11559–11618. [CrossRef] [PubMed]
214. Imani, I.M.; Kim, B.; Xiao, X.; Rubab, N.; Park, B.; Kim, Y.; Zhao, P.; Kang, M.; Kim, S. Ultrasound-Driven On-Demand Transient Triboelectric Nanogenerator for Subcutaneous Antibacterial Activity. *Adv. Sci.* **2023**, *10*, 2204801. [CrossRef] [PubMed]
215. *ISO 14040:2006*; Environmental Management—Life Cycle Assessment—Principles and Framework. International Organization for Standardization (ISO): Geneva, Switzerland, 2006.
216. *ISO 14044:2006*; Environmental Management—Life Cycle Assessment—Requirements and Guidelines. International Organization for Standardization (ISO): Geneva, Switzerland, 2006.
217. Zhang, R.; Dahlström, C.; Zou, H.; Jonzon, J.; Hummelgård, M.; Örtegren, J.; Blomquist, N.; Yang, Y.; Andersson, H.; Olsen, M.; et al. Cellulose-Based Fully Green Triboelectric Nanogenerators with Output Power Density of 300 W m^{-2}. *Adv. Mater.* **2020**, *32*, 2002824. [CrossRef] [PubMed]
218. Zhang, R.; Chen, D.; Hummelgård, M.; Blomquist, N.; Dahlström, C.; Chen, W.; Li, J.; Örtegren, J.; Wang, Z.L. Engineering Triboelectric Paper for Energy Harvesting and Smart Sensing. *Adv. Mater.* **2025**, *37*, 2416641. [CrossRef] [PubMed]

Disclaimer/Publisher's Note: The statements, opinions and data contained in all publications are solely those of the individual author(s) and contributor(s) and not of MDPI and/or the editor(s). MDPI and/or the editor(s) disclaim responsibility for any injury to people or property resulting from any ideas, methods, instructions or products referred to in the content.